THE STABILITY OF CU-RICH SULFIDE MINERALS AND THE FRACTIONATION OF AU FROM PGES IN FELSIC MAGMAS

An undergraduate thesis completed by:
Danica Pascua
Department of Geology
University of Toronto
2012

Supervisor:
Professor James Brenan

Abstract

We performed a combination of phase equilibrium, centrifuge, and metal fusion experiments involving Cu-rich sulfide compositions to test whether these minerals can fractionate Au from PGEs, as proxied by Re, in a silicate melt at oxidizing conditions. This is particularly relevant to subduction zone magmas, where crystal fractionation exerts an important control on the amount of ore metals sequestered by hydrothermal fluids to form shallow-level porphyry and epithermal deposits. Crystalline phases are key to the fractionation, as fixed lattice structures dictate the specific elements that can be incorporated into a phase. For this reason, we first constrained the maximum thermal stability of our Cu-rich sulfide compositions by performing a series of phase equilibrium and centrifuge experiments in air at temperatures ranging from 1050 to 1300ºC. Samples were loaded into fused silica tubes, evacuated, then sealed. Samples were run statically in the phase equilibrium experiments, while samples were subjected to high acceleration conditions (~500 to 600g) in the centrifuge experiments. The latter set of experiments was much more helpful in judging liquid and solid textures at run conditions. We then proceeded to our main metal fusion experiments involving chalcocite (Cu_2S) and Au and Re at the sub-solidus temperature of 1050ºC as determined by our earlier experiments. Fusion experiments were also buffered with the MnO-Mn_3O_4 solid oxygen buffer at FMQ + 2.6 to 4.4 (where FMQ is the fayalite-magnetite-quartz buffer). Solubilities of Au and Re in chalcocite were derived from our experimental results, and compared with their respective solubilities in silicate melt from the literature to yield partition coefficients between chalcocite and silicate melt. Our estimates for $D_{Au}^{Cc/melt}$ and $D_{Re}^{Cc/melt}$ range from 6 to 29 and 0.01 to 0.63, respectively, providing preliminary experimental evidence for the fractionation of Au from Re in chalcocite in a silicate melt at high fO_2. Future work will involve further testing this hypothesis by performing actual partitioning experiments that will consist of co-existing sulfide and felsic melt in equilibrium with metal.

Table of contents

1. Introduction

Given the close spatial relationship between subduction zone magmatism and Cu-Au sulfide deposits (Sillitoe, 2010, and references therein), the exact processes that lead to economic concentrations of these metals in this particular tectonic setting remain unclear. In evolved silicate melts of arc affinities, one main control on the concentration of ore metals is crystal fractionation (Hedenquist and Lowenstern, 1994). As in other magmatic systems, elements that are compatible in early-formed silicate and oxide minerals become depleted in the residual melt. The melt is left enriched in those elements which are incompatible. With increasing magmatic differentiation towards more felsic compositions, elements that are not partitioned into mineral phases remain in the melt, available for remobilization and transport to the near-surface by magmatic and/or meterotic waters circulating through the system.

Sulfides, in addition to early-formed silicate and oxide minerals, sequester chalcophile elements dissolved in the melt (Mungall, 2002). If the sulfide phase is crystalline, there is a greater constraint on the specific elements partitioned into it, as dictated by is fixed crystal lattice. Thus, given an initially fertile melt, metal budgets are at least partially dependent on the thermal stability of the sulfide phase (whether it is crystalline or remains liquid), its mineralogy (crystal lattice constraints), and the timing of its formation (early formation allows it to sequester chalcophile elements, whereas late formation allows progressive buildup of these elements in the melt) - all as a function of the temporal and spatial evolution of the melt.

Recently, Jenner et al. (2010) suggested that the mineral bornite (Cu_5FeS_4) is a plausible sulfide phase that affects metal budgets of magmas in the Pual Ridge and vicinity, Eastern Manus Basin. They found that upon reaching sulfide saturation (proxied by Se and apparently triggered by magnetite formation), Cu, Au and Ag contents in the magma dropped abruptly and substantially (Figure 1). The sulfide phase was tentatively identified as bornite, based on its thermal stability at the calculated liquidus temperature of their MD7b sample (~1095°C). In addition, sulfide phases forming in evolved silicate melts tend to be low in Ni and Co, but

high in Cu, because of preferential incorporation of Ni and Co into early-formed silicate minerals (Hattori, 1996). Bornite is also one of the most common Cu-sulfides, after chalcopyrite ($CuFeS_2$) (Cook et al., 2011).

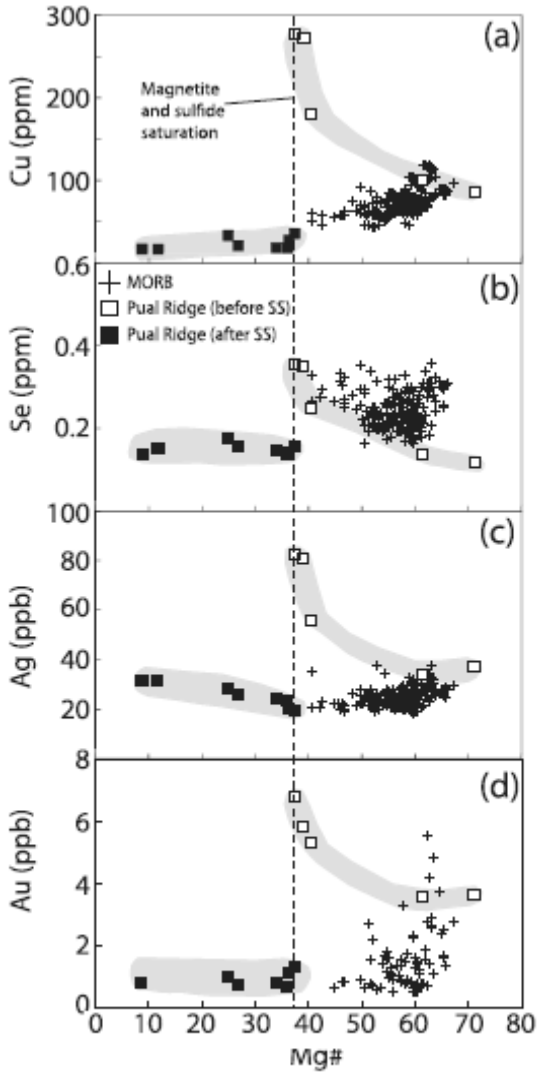

Figure 1. Covariation of (a) Cu, (b) Se, (c) Ag, and (d) Au vs. Mg-number. At an Mg-number of ~40, Cu, Ag and Au contents suddenly drop following magnetite fractionation and sulfide saturation (SS). Shaded fields: liquid line of descent of the Pual Ridge magmas. From Jenner et al. (2010).

Jenner et. al (2010) further proposed that because bornite hosts Cu in its structure, Au and Ag can be similarly partitioned into this phase as they have the same +1 valence state as Cu. An abrupt decrease in Pt contents was not observed upon sulfide saturation (Jenner et al., 2010, their Figure 4). This might demonstrate that platinum group elements (PGEs) with higher

valence states (commonly +2), although also potentially strongly chalcophile, are left in the residual melt. Thus the main focus of the current work is to test the hypothesis that crystalline bornite preferential incorporates of Cu, Au and Ag over PGEs in evolved melts at magmatic temperatures. Because one key feature of arc-related magmas is their being more oxidized than mid-ocean ridge basalt (MORB), our high-temperature partitioning experiments were performed at high oxygen fugacity (fO_2). Differentiation of a sulfide-undersaturated, oxidized melt thus allows the progressive buildup of Cu, Au and Ag in the melt (Jenner et al., 2010). Unless the melt remains sulfide-free, it will continually lose these elements during its evolution. Depending on the relative timing of events, the sulfide that is eventually formed is rich in these ore metals (Jenner et al., 2010), or more are retained and then later sequestered by hydrothermal fluids.

Some authors have already suggested that crystallization of sulfides in the Cu-Fe-S system, particularly pyrrhotite ($Fe_{1-x}S$) and intermediate solid solution (iss, the high-temperature equivalent of chalcopyrite), plays an important role in sequestering Cu and Au from felsic melts. For example, Lynton et al. (1993) and Jugo et al. (1999) found that at relatively oxidizing conditions, partition coefficients (D) of either Cu or Au between highly felsic melts and co-existing pyrrhotite or iss ranged from 140-5700. Experiments were performed at much lower temperatures (800-850°C, in the range of formation of shallow porphyry Cu ore deposits) than investigated in this work (1100-1300°C, magmatic temperatures). Simon et al. (2008) showed that at similar and oxygen fugacities and melt compositions, yet at a higher temperature of 1050°C, $D_{Cu}^{Po/melt} \geq 200$, $D_{Au}^{Po/melt} = 120 \pm 50$, and $D_{Ag}^{Po/melt} = 58 \pm 8$. Pressures ranged from ambient to 1 kbar in most experiments. Most previous experimental work has focused on the amount of Cu and Au (and less well-documented for Ag) that can enter into pyrrhotite and iss rather than bornite in an oxidized, felsic melt. Virtually no data exists for Cu/Au/Ag vs. PGE partitioning at these conditions. Experiments involving Au concentrations in bornite and iss were carried out by Simon et al. (2000). They demonstrated that for all temperatures, bornite accommodates one order of magnitude more Au than iss, increasing with increasing temperature. However, these experiments were performed at lower temperatures (400-700°C) and without co-existing melt.

Since crystalline phases are key to ore metal fractionation in a silicate melt, it is important to constrain the thermal stability of Cu-rich sulfides at high (magmatic) temperatures. Crystalline sulfides incorporate and partition specific elements in their fixed structures from the residual silicate melt. Sulfide liquids, in contrast, lack the long-range crystal structures that would be selective to elements fractionated from the silicate melt. While a great deal of experimental work has been done on the Cu-Fe-S system (Yund and Kullerud, 1966; Kullerud et al., 1969; Barton, 1973; Cabri, 1973; Craig and Scott, 1974), the maximum thermal stability of Cu-rich sulfides is still not well constrained. Much of the high temperature work (up to 1100°C) on the Cu-Fe-S system has been drawn from Kullerud et al. (1969) (Figure 2). In this work, we first present results of static and high acceleration phase equilibrium experiments on different Cu-rich sulfide compositions, including bornite and chalcocite (Cu_2S) as these minerals are the high temperature phases in the Cu-Fe-S system (Figure 2). We then show results of solubility experiments involving Au and Re in crystalline chalcocite buffered at high fO_2. Although Re is not a PGE, it is commonly in +4 and +6 oxidation states, demonstrating fractionation more dramatically than the +2 PGEs. Using literature values of the respective solubilities of these metals in silicate melt, we estimated partition coefficients that effectively demonstrate the behaviour of Au and Re in chalcocite in silicate melts at oxidizing conditions.

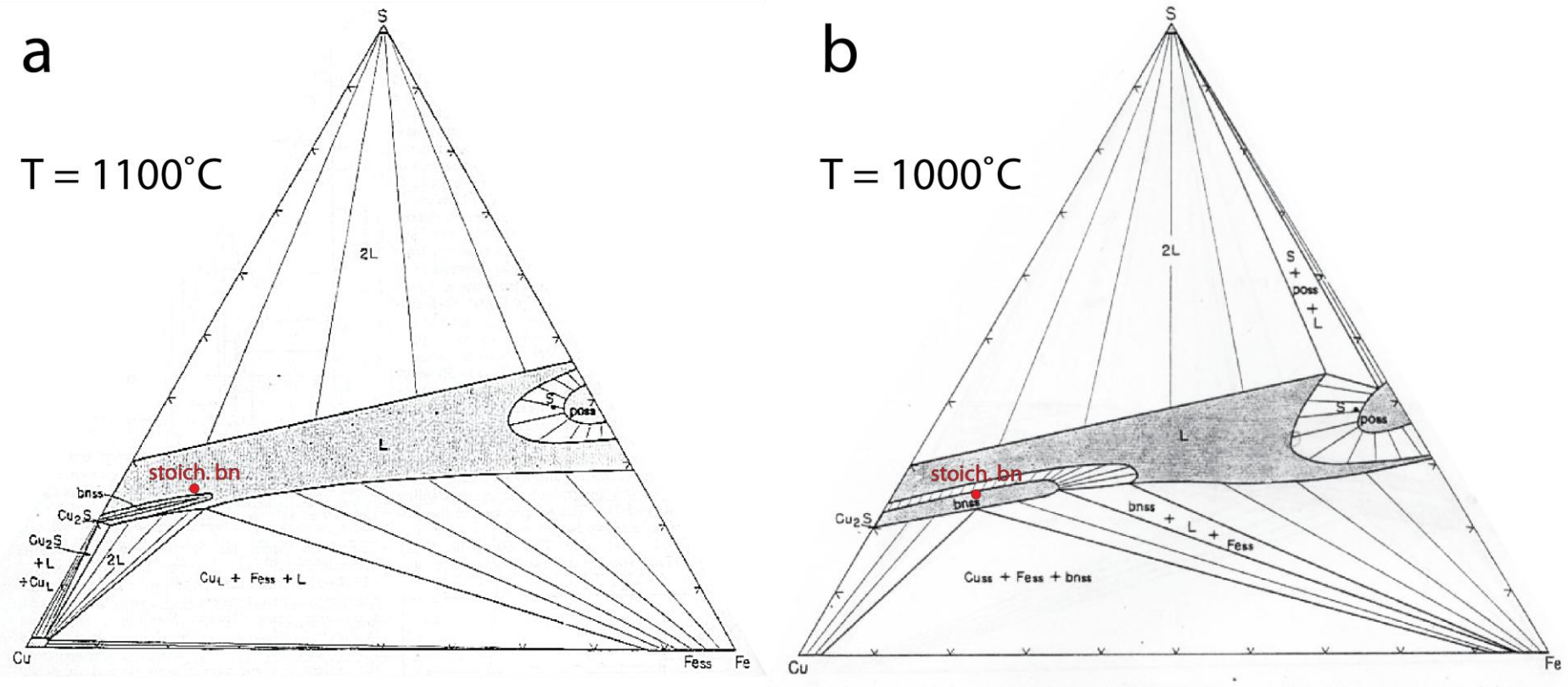

Figure 2. Phase relations in the Cu-Fe-S system at (a) 1100°C and (b) 1000°C (in wt. %). All phases and phase assemblages co-exist with vapour. Stoichiometric bornite is shown as a red dot, plotting in the field of liquid at 1100°C and of bornite solid solution at 1000°C. The average composition of the Sudbury Cu-Fe-Ni-S ores when projected onto the Cu-Fe-S plane is shown as point S. From Kullerud et al. (1969).

2. Experimental methods

All samples were prepared using the evacuated silica tube technique, varying the material loaded into the silica tube depending on the purpose of the experiment. Silica tubing was first closed at one end using an oxy-acetylene torch. The resulting tubes were cleaned with liquid detergent and left to dry in a drying oven until use. Material was loaded into the bottom of the tube, then pressed down with a stainless steel or glass rod. Silica rod was inserted from the top as a spacer to minimize vapour space during the experiment. The tube was then attached to a vacuum line for 30 minutes to 1 hour (Figure 3) prior to and during welding it shut with the torch. With the body of the tube wrapped around a cloth soaked with water, the top end was "necked down," twisted off and sealed (Figure 4). Finally the ampoule was dried and placed in alumina crucibles for the experiment.

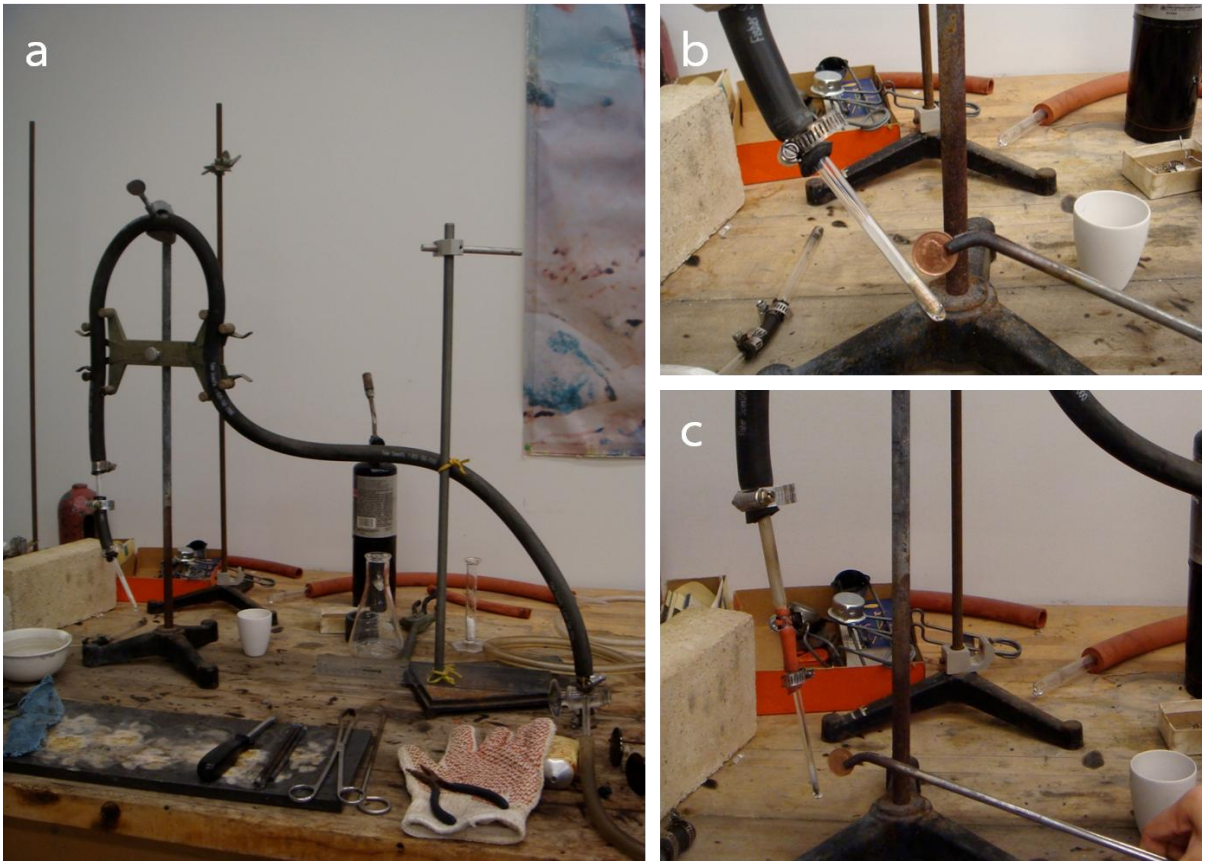

Figure 3. Set-up for evacuating silica tubes. (a) Entire set-up without the vacuum pump (underneath the table). The vacuum pump is underneath the table (not shown). The top end of

the silica tube is slid inside a piece of rubber tubing and is secured with a screw clamp. This assembly is attached to a wider (OD) piece of silica tubing that leads to the vacuum pump. The ends of the rubber tubing/silica tube are secured with screw clamps. (b) Close-up of the sample in a, with a powdered mixture of chalcocite (Cu_2S; Cu: orange, S: light green) at the bottom of the tube and a glass spacer on top. (c) Cu-rich sulfide sample with narrower tubing This assembly makes use of narrower rubber tubing to connect the sample to the vacuum line.

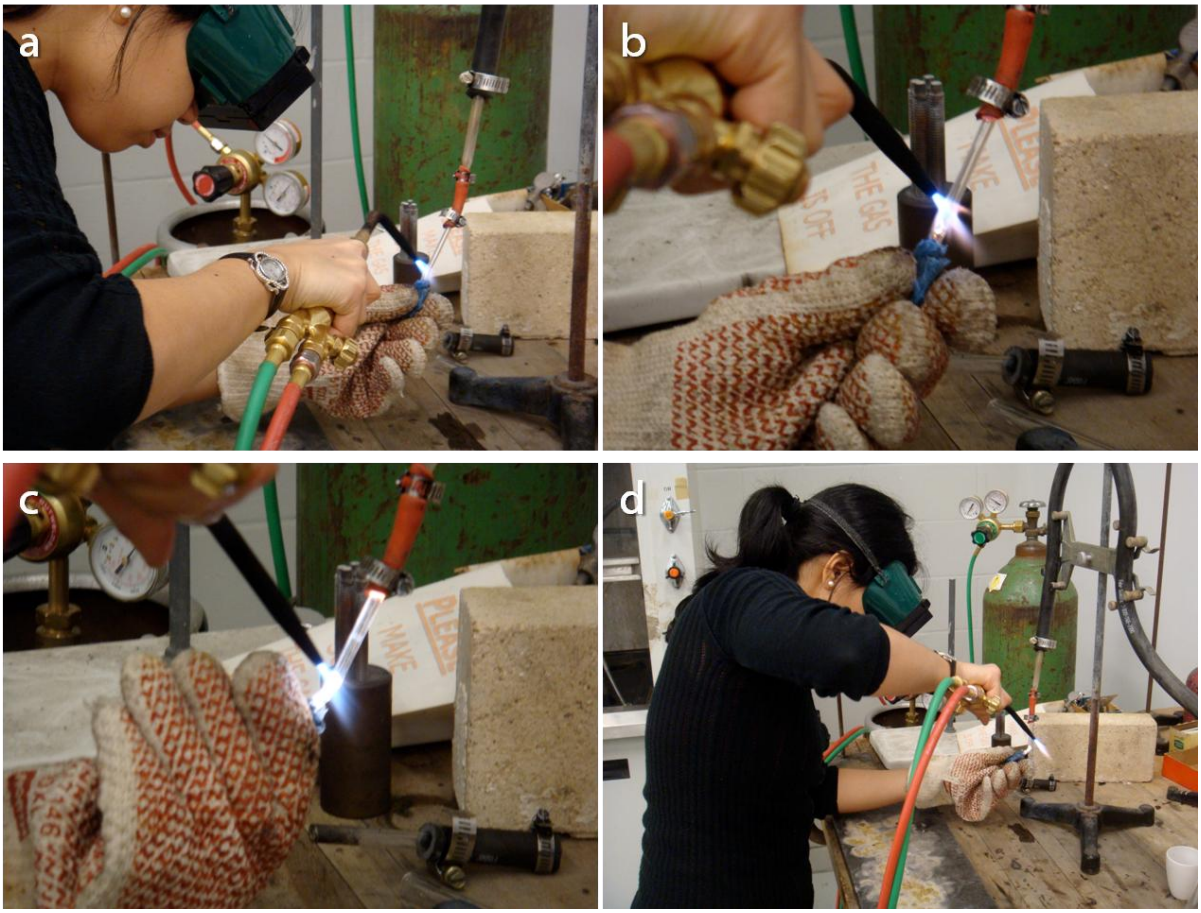

Figure 4. (a) to (d) Sealing the silica tube with the torch while attached to the vacuum line.

Four separate sets of experiments were performed with samples encapsulated in evacuated silica tubes.

2.1. Phase equilibrium experiments

2.1.1. Starting compositions

Cu-rich sulfide compositions along the line shown in Figure 5 were prepared by first synthesizing the end member compositions 1 and 5. Composition 1 is in the field of liquid,

while Composition 5 is chalcocite (Cu_2S) as determined by Kullerud et al. (1969). Stoichiometric bornite (Cu_5FeS_4) was also synthesized. These starting materials were prepared using reagents in Table 1.

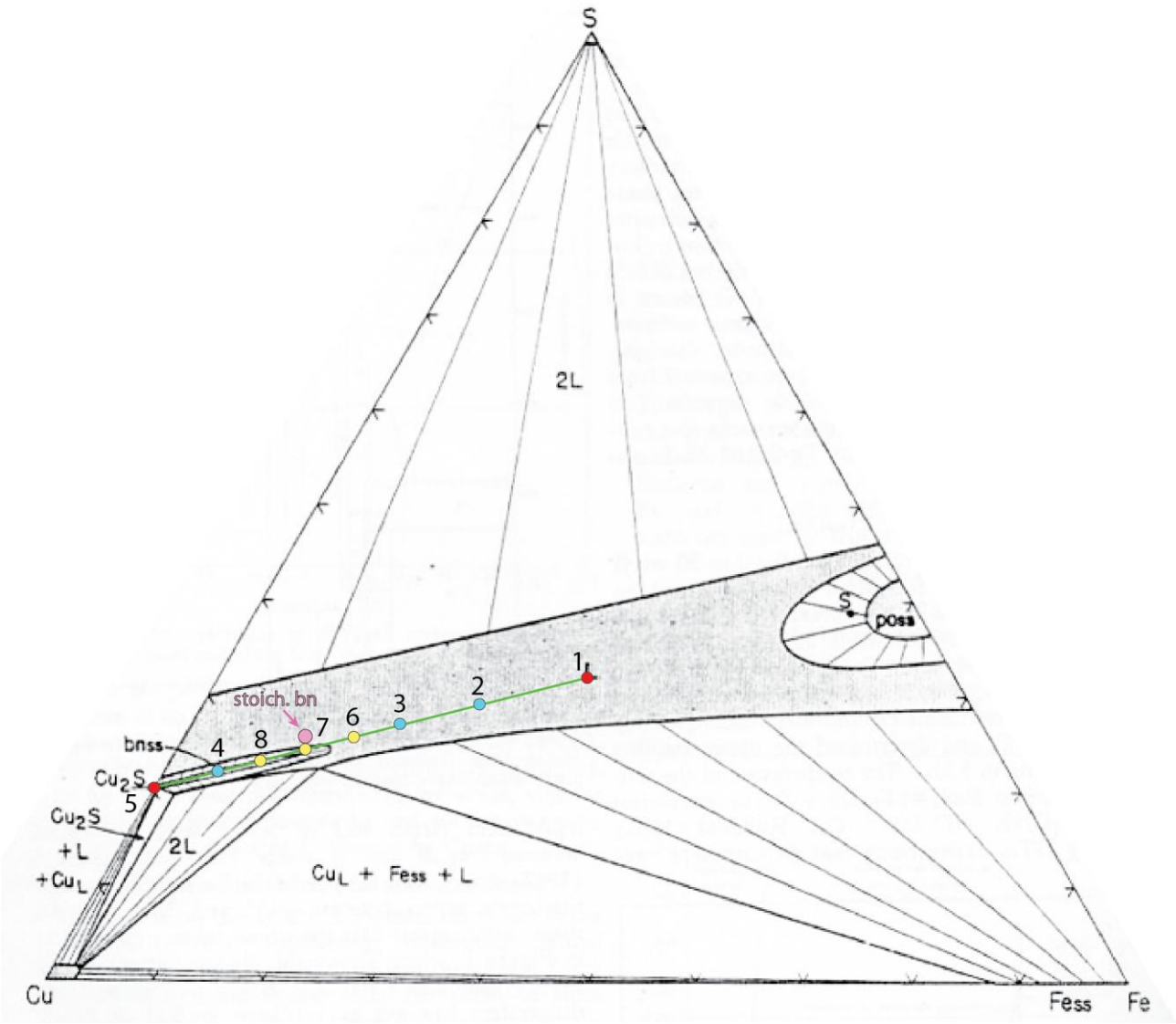

Figure 5. Cu-Fe-S phase diagram at 1100°C from Kullerud et al. (1969) with sulfide mixtures plotted as dots. Red, 1 and 5: starting compositions; blue, 2 to 4: mixtures in 1200 and 1100°C experiments; yellow, 6 to 8: mixtures in 1200°C experiments only. Stoichiometric bornite is plotted in pink for reference.

Table 1. Physical form and purity of reagents for starting materials.

Number	Material	Source	Form	Size	Purity (%)
1	Cu	Alfa Aesar	Powder	-625 mesh	99
2	Cu	In-house	Metal, cleaned with HCl	~100 μm long x ~20-30 μm wide	n.d.
3	Cu	Alfa Aesar	Powder	-100 mesh	99.999
4	Fe	Alfa Aesar	Powder	-22 mesh	99.998
5	S	Alfa Aesar	Powder	-20+325 mesh	99.999

n.d.: Not determined

In a typical synthesis, reagents were weighed in their appropriate proportions, then combined and mixed with a spatula while still on the weighing paper. This mixture was loaded into a silica tube (4 mm ID x 6 mm OD or 6 mm ID x 8 mm OD, depending on the amount synthesized), evacuated, and sealed. The sample, held in an alumina crucible, was placed into a Fischer Isotemp forced-draft muffle furnace overnight to 5 days to react. The sample was then taken out of the furnace and cooled in air. The silica tube was cracked open to remove the sintered material. This was ground under ethanol and dried in an agate mortar, then placed in a vial and stored in a dessicator until use. Table 2 shows the compositions and run conditions of the three starting materials.

Table 2. Compositions and run conditions of the starting materials.

Starting material	Composition (wt. %)			Weight loaded into silica tube (mg)	Initial run temperature (°C)	Final run temperature (°C)	Run duration (hours)	Colour of powder after grinding
	Cu	Fe	S					
Cu-Fe-S liquid[a]	35 (1)	33.4 (4)	31.6 (5)	500	600	1000	23 at 600°C, then ramped to 1000°C over 5, then held for 15	Brownish-yellow
Chalcocite (Cu_2S)[b], Batch 1	79.86 (2)		20.14 (5)	1000	600	600	110	Dark grey-blue
Chalcocite (Cu_2S)[b], Batch 2	79.86 (3)		20.14 (5)	500	300	1000	Ramped to 1000°C over 10, then held for 12	Dark grey-blue
Bornite (Cu_5FeS_4)[c]	63.32 (3)	11.13 (4)	25.56 (5)	500	600	600	16.75	Dark grey-purple

[a]Red dot 1, [b]Red dot 5, [c]Pink dot in Figure 5. Numbers in parentheses below compositions refer to reagents used in Table 1. Coarser forms of Cu powder were used after the Cu-Fe-S liquid synthesis, as the -625 mesh powder was too fine and adhered to the weighing paper

2.1.2. Isotherm experiments (1200 and 1100°C)

50-mg mixtures of compositions along the line in Figure 5 (blue and yellow dots) were prepared by mixing varying proportions of Compositions 1 and 5 (red dots). Mixtures were loaded into 3 mm ID x 5 mm ID silica tubes, evacuated, and sealed (Figure 6). Samples were usually 3.5 to 4.5 mm in length.

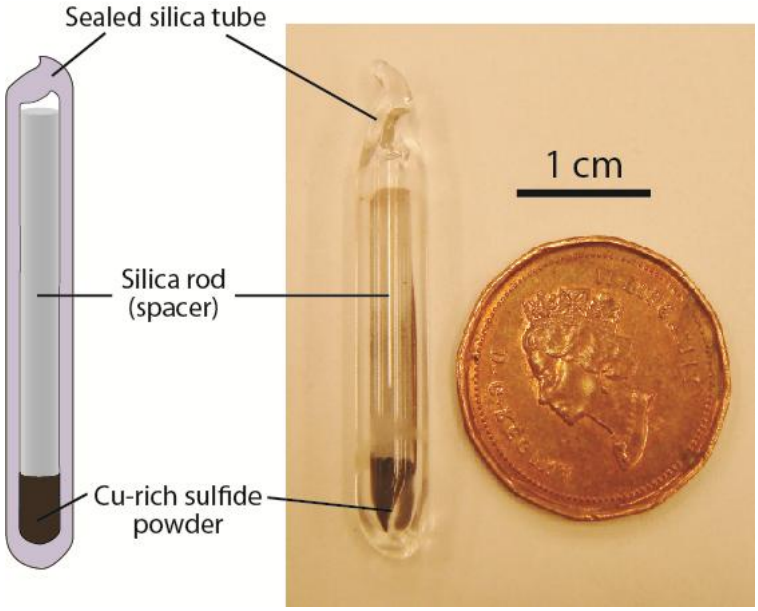

Figure 6. Sample assembly for phase equilibrium experiments.

A Deltech drop-down box furnace (DT-29-VTHN-E818P4) with a type-S thermocouple was used for the phase equilibrium experiments (Figure 7). Up to five samples, held in alumina crucibles, were placed inside the furnace at the same time (Figures 8 and 9). Isotherms of 1200 and 1100°C were run with five compositions each (red and blue dots in Figure 5). Three additional samples (yellow dots) were run for the 1200°C isotherm. Experiments were quenched after ~3 to 20 hours by quickly dropping the samples in cold water (Figure 10). In our early experiments with thinner-walled silica tubes (3 mm ID x 4 mm OD), samples exploded upon quench which led to sulfur loss. Recovered sulfide material was commonly magnetic, and reaction with the tube was also evident in some samples. With thicker-walled tubes (3 mm ID x 5 mm OD), samples were intact upon quench (Figure 11). Two experiments with bornite compositions were performed at 1300 and 1200°C following the same method as above.

Figure 7. The Deltech drop-down box furnace. A type-S measuring thermocouple is inserted at the top of the furnace.

Figure 8. Samples in alumina crucibles before placing them into the furnace. Notches were made on the rims of the crucibles to distinguish the samples from one another.

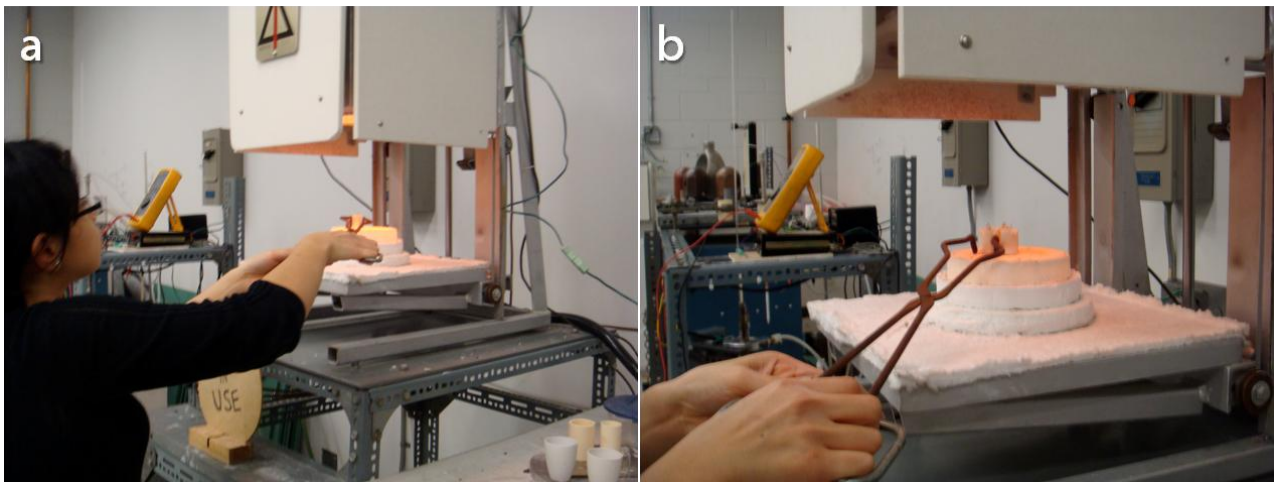

Figure 9. (a) Placing the crucibles into the furnace with tongs. (b) Crucibles were arranged close together in a circular pattern to minimize the thermal gradient between samples.

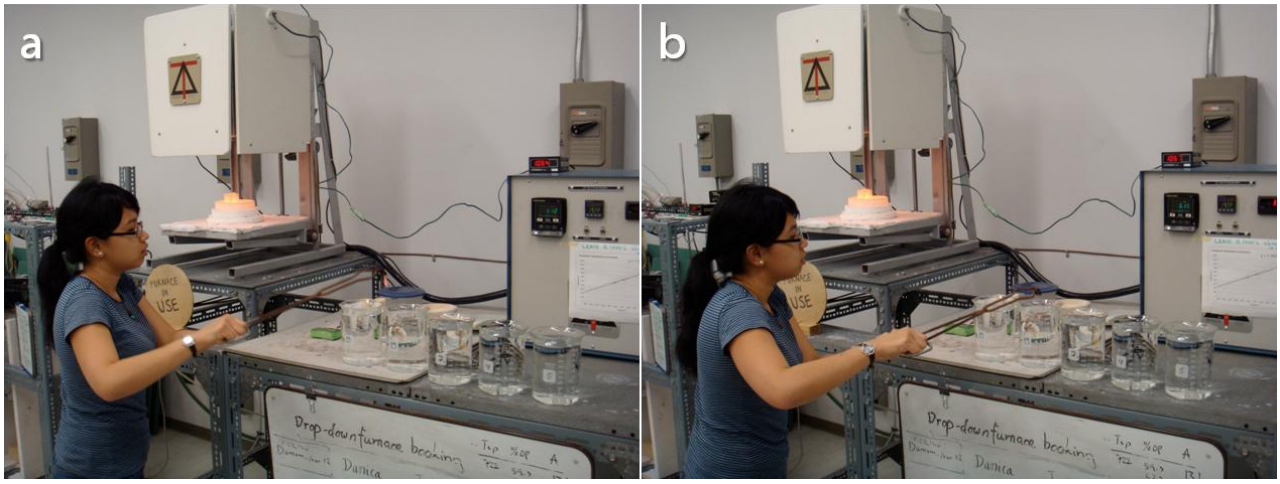

Figure 10. (a) Taking the hot silica tube out of the furnace and (b) dropping it in cold water.

Figure 11. Sample quenched in cold water.

2.2. Centrifuge experiments

We decided to focus our later experiments on two of our sulfide compositions, bornite and chalcocite. Preliminary observations on the bornite and chalcocite phase equilibrium experiments at 1100 to 1300°C (BN1100-5, BN1200-5a, Bornite-1200, Bornite-1300) suggested that the phases were homogeneous without any obvious evidence of liquid quench textures (Figures 27, 31 and 32). While this may indicate that these phases are solid (crystalline), Composition 1 showed the same homogenous texture (Figures 23 and 28), but plots in the field of liquid (Figure 5). It is important to determine whether these Cu-rich sulfides

exist as crystalline or liquid phases at magmatic temperatures because crystalline phases and their fixed lattice structures are key to ore metal fractionation.

To test whether these sulfides are solid or liquid phases at run conditions, we subjected samples to high acceleration in a vertical tube furnace rotated in a large-volume centrifuge at low speeds (<10,000 rpm). This technique was also employed by Brenan et al. (2008) to promote phase separation in Cu-Ni and Cu-Fe-Ni sulfides. In our experiments, we loaded 10 mg of high purity silica powder, followed by 25 mg of bornite into the bottoms of silica tubes. Silica is highly refractory with T_m = 1610°C (Weast, 1979), so it will remain as a solid powder during the experiment. If the sulfide is liquid at run conditions, then it should replace the silica powder at the bottom of the ampoule because it is much denser (specific gravities of bornite, chalcocite and silica are 5.06-5.08, 5.5-5.8 and 2.65, respectively; Klein and Dutrow, 2008). Gravitational separation of phases is greatly aided by accelerations reached in this set-up (~500 to 600g). If the sulfide is solid, then no phase inversion (top to bottom for the sulfide, bottom to top for the powdered silica) should be observed. Following the evacuated silica tube technique used in previous experiments, we ensured that the final capsule length was 23 to 25 mm so that the bottom part of the capsule would be in the 1 cm hotspot of the furnace. A typical sample is shown in Figure 12.

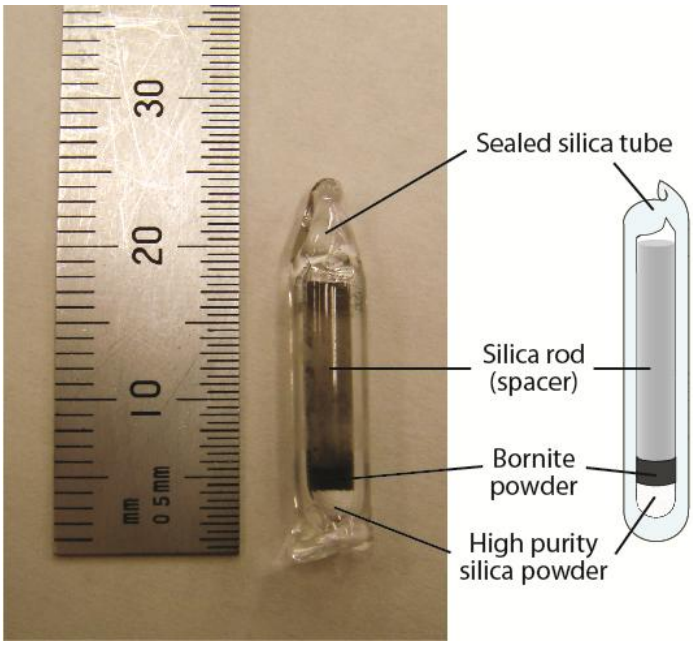

Figure 12. Sample assembly for centrifuge experiments.

A centrifuge experiment for one sample was preceded by a "static" first step. Two identical samples were run in the drop-down furnace at the same temperature for 1 to 3 hours, then air cooled. One sample was kept as the control, while the other was run in the centrifuge at the same temperature as the static step.

A complete description of the centrifuge and furnace apparatus is found in Roeder and Dixon (1977). Brenan et al. (2008) used the same system and provided a summary of its operational parameters. The centrifuge is an International Centrifuge Model UV equipped with a four rotating cups and a central slip-ring assembly on the rotating shaft (Figures 13 and 14). The slip-ring assembly provides a sliding electrical contact between the power and temperature controls and the rotating furnace. The furnace itself is shown in Figure 15. Inside the outer housing is an alumina tube wound with Cr-Al wire and covered with alumina paste to prevent contact between the wiring. A pyrophyllite cup holds the sample and thermocouple inside the alumina tube furnace (Figure 16). The sample is placed in the predetermined hotspot of the furnace, with two type-S measuring thermocouples positioned beside it. There is a 15-mm vertical separation between the two thermocouples, with the lower thermocouple positioned at the same level as the bottom of the sample. The upper thermocouple is monitored by a programmable controller which allows temperature control during the experiment. The thermal gradient between the two thermocouples ranged from 3 to 7°C. Additional pyrophyllite spacers above and below the cup hold the sample and thermocouple assembly in place.

Figure 13. The entire centrifuge system.

Figure 14. The centrifuge head with its four rotating cups and central slip-ring. The furnace is held by the bottom cup, with three pairs of wires connecting the top of the furnace to the slip-ring. The two pairs of wires connect the two thermocouples of the furnace to the main controller, while the remaining pair provides power to the furnace. A counterbalance filled with sand is held by the top cup.

Figure 15. The complete furnace assembly showing (from left to right) the outer housing, pyrophyllite cup and spacers, and two thermocouples held in a single alumina spaghetti. The long alumina spaghetti in the middle is only for removing or pushing components into the furnace. The furnace itself consisting of an alumina tube with Cr-Al wiring is inside the outer housing. Penny for scale.

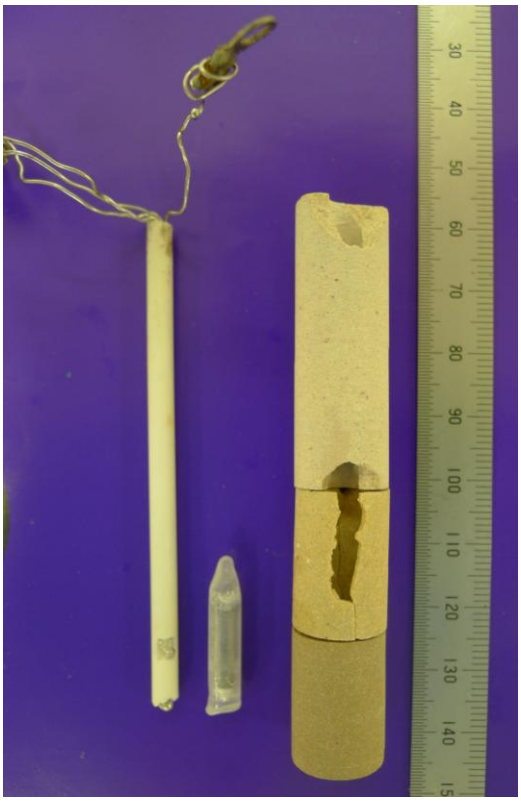

Figure 16. From left to right: the two measuring thermocouples (upper and lower) inside an alumina spaghetti; sample (quenched from the static first step); pyrophyllite cup and spacers. The thermocouple assembly and the sample are positioned in the pyrophyllite cup and spacers at the level shown. Scale bar in mm.

In a typical experiment, the sample was first rotated for a few minutes until the centrifuge was judged stable. The furnace was ramped to the run temperature after applying power to the slip-ring. The final run temperature was reached within 30 to 45 minutes, after which it was held for 1 to 3 hours. During the experiment, the sample rotation rate was usually ~1700 to 1800 rpm, as measured by an Extech digital photo tachometer (461893). The experiment was terminated by cutting the power to the furnace and allowing the sample to cool while decelerating. The sample was removed when the spinning stopped. In our earliest experiment, we quenched the sample by cutting the power to the furnace, disconnecting its power and thermocouple leads, and inverting it so that the sample and spacers fell in a beaker of cold water. We realized that we would still observe density inversions even when the sample was not quenched.

The following equation was used to relate the sample rotation rate to the acceleration to which the sample was exposed:

$$g = 11.18 \times 10^{-6} (rpm)^2 R \qquad \textbf{(1)}$$

This acceleration is expressed as a multiple of g, the normal acceleration due to gravity (9.8 m/s^2). R is the distance from the axis of rotation (17 cm in this configuration).

In addition to our bornite and chalcocite experiments, we ran two different compositions to demonstrate that the silica floation method faithfully records sample melting. Cent1100-FeS and Cent1100-Mix2 (synthetic troilite, FeS, prepared similarly as our sulfide mixtures, and Composition 2 of the phase equilibrium experiments, see Figure 5) were chosen as control samples. Troilite is expected to be solid with T_m = 1193 to 1199°C (Weast, 1979), while preliminary results from BN1100-2 suggested that Composition 2 is liquid at run conditions (Figure 29).

2.3. Buffered fusion experiments

2.3.1. Experimental design

2.3.1.1. Metal-free experiments with bornite

We first performed buffered, "metal-free" experiments with bornite to find a suitable configuration for our later experiments with chalcocite and Au and Re. These experiments followed the same evacuated silica tube technique. In our first attempt, we loaded a 6 mm ID x 8 mm OD outer capsule with a 1:1 mixture of the solid oxygen buffers MnO and Mn_3O_4 (100 mg total weight). This buffer mixture was packed down with a glass rod. An inner cup (3 mm ID x 5 mm OD x 11.5 mm long) was loaded with synthetic bornite doped with ~500 ppm each of Au, Ag, Re and Ru (95.9 mg). The doped bornite mixture was also packed down, and a glass spacer was placed above it. The entire inner cup was then slid into the outer capsule with the buffer. A glass spacer was inserted, and the outer capsule was evacuated and sealed.

The experiment (named 1200-DopedBN-MMO) was performed at 1201°C for 1 day in the drop-down box furnace, and quenched in cold water. Preliminary analysis with backscattered electron (BSE) images and energy dispersive spectrometry (EDS) on the scanning electron microscope (SEM) suggested that magnetite formed in equilibrium with bornite (Figure 38). Knowing that magnetite is stable at high fO_2 in the presence of bornite, we refined our experimental technique to include a magnetite cup instead of a silica cup to hold the bornite powder (Figure 17). This would prevent additional magnetite forming at the expense of O_2 in the system from the buffer mixture. To ensure that enough O_2 is present during the experiment even with magnetite stable, we used a 1:2 instead of a 1:1 mix of MnO and Mn_3O_4 as the buffer. We also included a layer of high purity silica powder between the buffer mixture and magnetite cup to prevent the two from coming into contact. Finally, we placed a hollow silica ring on top of the magnetite cup instead of a glass spacer inside the cup as in our first attempt. We also used a smaller outer capsule (4 mm ID x 6 mm OD) with this new configuration (Figure 18**,** Table 3). We then conducted the experiment (1100-Bornite-MMO) again at a lower temperature of 1100°C.

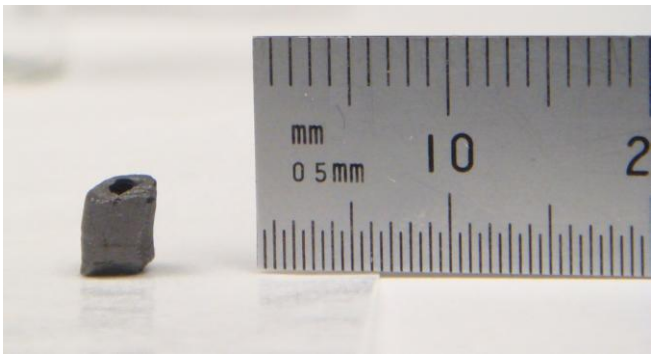

Figure 17. Magnetite cup to hold the bornite powder.

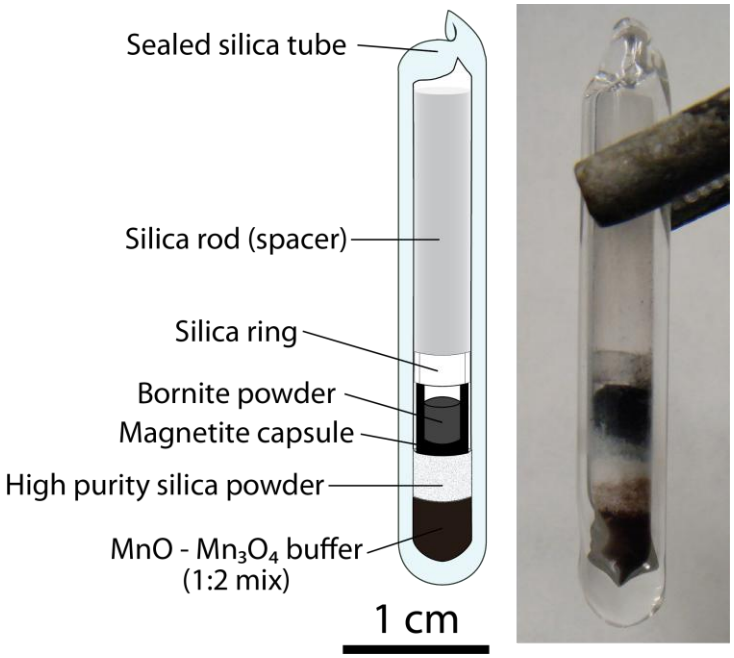

Figure 18. Refined sample assembly in the buffered bornite experiment (1100-Bornite-MMO).

Table 3. Summary of parameters in sample preparation of 1100-Bornite-MMO.

Sample assembly	
Weight of MnO powder	34.9 mg
Weight of Mn_3O_4 powder	67.5 mg
Weight of high purity SiO_2 powder	48.98 mg
Magnetite cup	Single crystal magnetite sourced from Balmat, New York state
Weight of bornite in magnetite cup	~15 mg
Dimensions of outer silica capsule	4 mm ID x 6 mm OD nominally

2.3.1.2. Cu-rich sulfides with Au and Re

We extended our sample assembly to include the sulfide (bornite or chalcocite) sandwiched between an upper and lower layer of Au or Re powder (Table 4), all contained in an inner capsule. Magnetite was still used as an inner capsule with bornite, while a silica cup (3 mm ID x 4 mm OD x 8 to 9 mm long) was used with chalcocite to prevent iron contamination. Thus four samples were prepared with the MMO buffer mixture:

1. Bornite + Au
2. Bornite + Re
3. Chalcocite + Au
4. Chalcocite + Re

The final length of the sample (spacer included) was 3.5 to 4 mm. Figures 19 and 20 show schematic diagrams and photos of the doped bornite and chalcocite samples. The samples, held in alumina crucibles, were annealed at 1050°C in the drop-down box furnace for 4 to 6 days, then air cooled when the experiment was terminated.

Table 4. Physical form and purity of metal reagents for the buffered fusion experiments.

Material	Source	Form	Size	Purity (%)
Au	Alfa Aesar	Powder, spherical	-325 mesh	99.9
Re	Aldrich Chemical Co.	Powder	n.d.	99.995

n.d.: Not determined

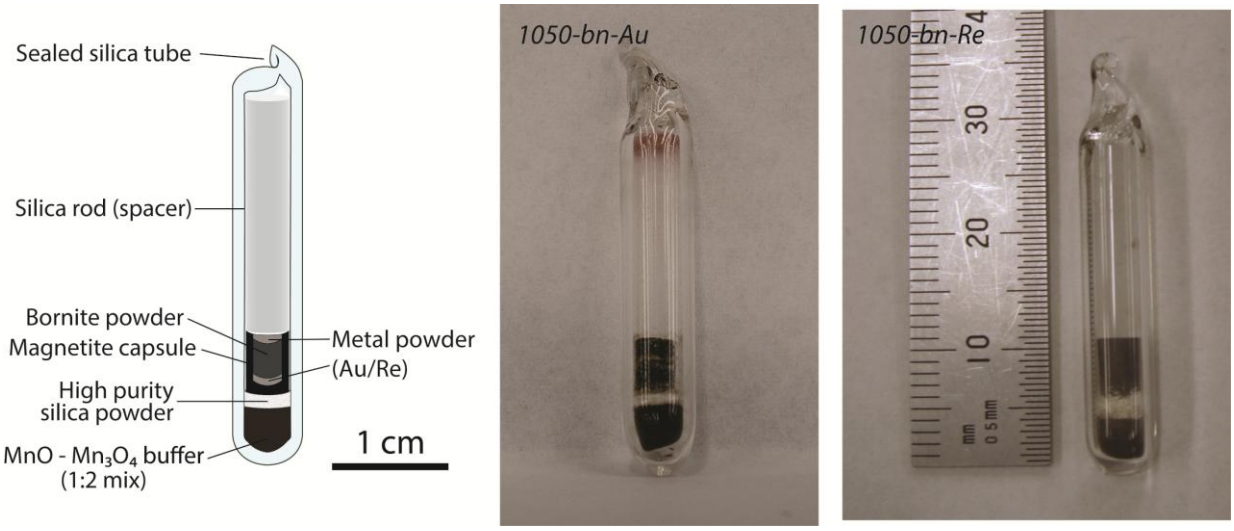

Figure 19. Sample assembly for samples with bornite and either Au or Re. Note that an inner capsule of magnetite was used in these experiments.

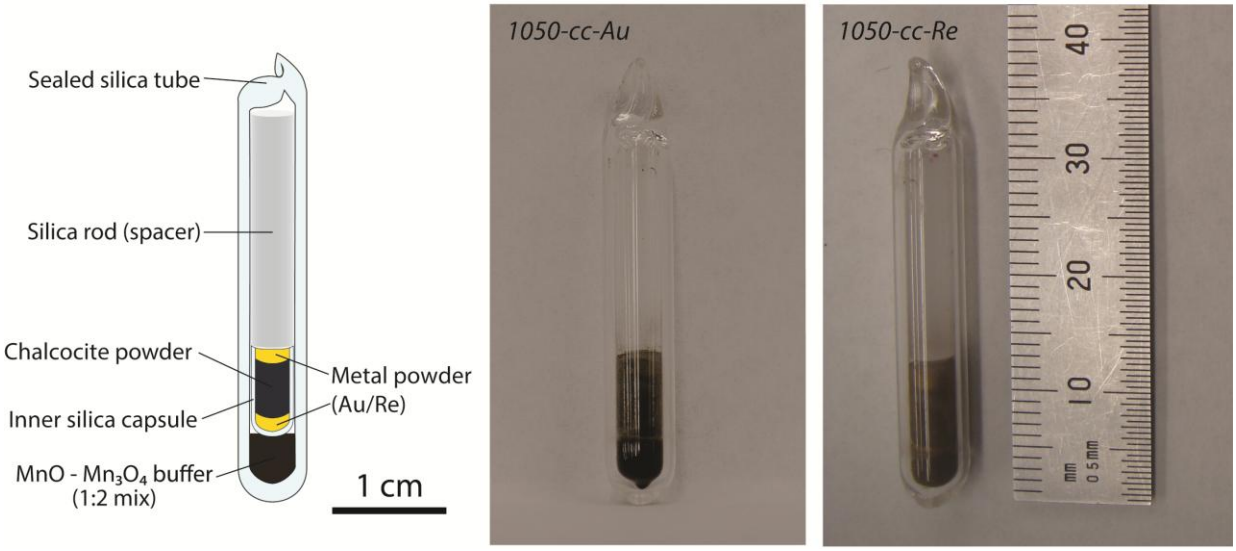

Figure 20. Sample assembly for samples with chalcocite and either Au or Re. Note that an inner silica capsule was used in these experiments.

2.3.2. Control of fO_2 and fS_2

In this section we show how we controlled both the fO_2 and fS_2 of our experiments by adding only an oxygen buffer to our samples. From our experiments, we found that magnetite was stable with bornite at high fO_2 (see Sections 2.3.1.1 and 4.2.1). The following reaction

describes the oxidation of bornite, resulting into the formation of magnetite, chalcocite and sulfur gas:

$$\underset{Bn}{3Cu_5FeS_4} + 2O_{2(g)} = \underset{Mt}{Fe_3O_4} + \frac{15}{2}\underset{Cc}{Cu_2S} + \frac{9}{4}S_{2(g)} \quad \textbf{(2)}$$

Assuming pure solid mineral phases ($a_i = 1$), the equilibrium constant (K_{eq}) of Reaction 2 and its natural logarithm can be written in terms of only fO_2 and fS_2:

$$K_{eq} = \frac{fS_2^{\frac{9}{4}}}{fO_2}$$

$$\ln K_{eq} = \frac{9}{4}\ln fS_2 - 2\ln fO_2 \quad \textbf{(3)}$$

The Gibbs free energy of the reaction ($\Delta_r G^o$) is related to K_{eq} and $\ln K_{eq}$ by the following relation:

$$\Delta_r G^\circ = -RT \ln K_{eq} \quad \textbf{(4)}$$

where R = $8.314 \frac{J}{mol - K}$ and T = temperature in K.

Substituting Equation 4 into Equation 3 results into the following relation:

$$\frac{9}{4}\ln fS_2 - 2\ln fO_2 = \frac{-\Delta_r G^\circ}{RT} \quad \textbf{(5)}$$

$\Delta_r G^o$ can be calculated from the Gibbs free energies of formation ($\Delta_f G^o$) of the products and reactants involved in Reaction 2, not including gaseous O_2 and S_2 for which ${}_fG^o = 0$:

$$\Delta_r G^\circ = \frac{15}{2}\,{}_f G^\circ_{Cu_2S} + {}_f G^\circ_{Fe_3O_4} - {}_f G^\circ_{Cu_5FeS_4} \quad \textbf{(6)}$$

Standard state free energies of the above phases were obtained from Robie et al. (1994) and allowed us to calculate $\Delta_r G^o$ as a function of temperature. Rearranging Equation 6 yields two equations for fO_2 and fS_2 in terms of known values of $\Delta_r G^o$ and T. Note that fO_2 and fS_2 are not independent of each other; control of one allows the determination of the other intensive parameter:

$$ln\ fS_2 = \frac{4}{9}\left(\frac{-\Delta_r G^\circ}{RT} + 2\,ln\ fO_2\right) \quad \textbf{(7)}$$

$$ln\ fO_2 = \frac{\frac{9}{4}ln\ fS_2 + \frac{-\Delta_r G^\circ}{RT}}{2} \quad \textbf{(8)}$$

We chose to control the fO_2 of our experiments at the MMO buffer for practical reasons. It is a convenient solid buffer, eliminating the need to control fO_2 in a gas-mixing furnace, and it does not react with S. log fO_2 values were obtained from the equation given by O'Neill and Pownceby (1993) for the MMO buffer:

$$MnO - Mn_3O_4 : \mu_{O_2}\left(J/mol\right) = -563,241 + 1,761.758T - 220.490T\ln T + 0.101819T^2 \quad \textbf{(9)}$$

where

$$\log\ fO_2 = \frac{\mu_{o_2}}{RT\ln(10)} \quad \textbf{(10)}$$

Using Equations 9 and 10, log fO_2 = -6.0 and log fS_2 = -0.80 at the MMO buffer at 1050°C (1323.15 K). This holds true provided that both MnO and Mn_3O_4 are still stable after the experiment. All phases defined in Reaction 2 should also be present. Figure 21 shows calculated log fS_2's for known fO_2's at the MMO and FMQ buffers. Buffer curves for the

oxygen buffers relevant in this work are shown in Figure 22. Although the MMO buffer is more oxidizing than the conditions at which arc rocks typically form (FMQ + 1), we still chose to use it out of practicality.

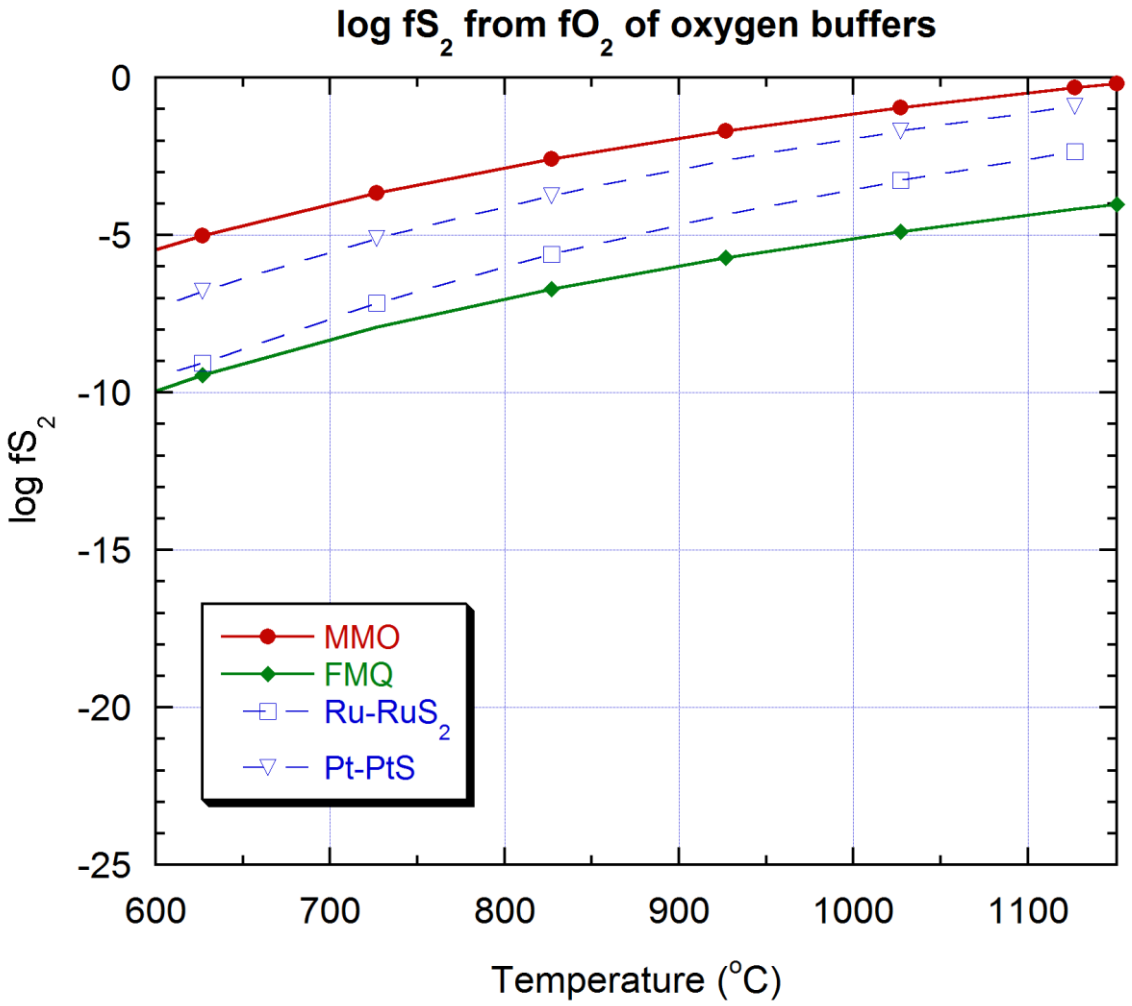

Figure 21. log fS_2 calculated for selected oxygen buffers using Equation 7. MnO-Mn_3O_4 (MMO): O'Neill and Pownceby, 1993; fayalite-magnetite-quartz (FMQ): O'Neill, 1987. Most reduced oceanic basalts crystallize at the Ru-RuS_2 and Pt-PtS sulfur buffers (blue) shown for reference. Values for log fS_2 for these sulfur buffers were calculated from standard state free energies from Barin (1995).

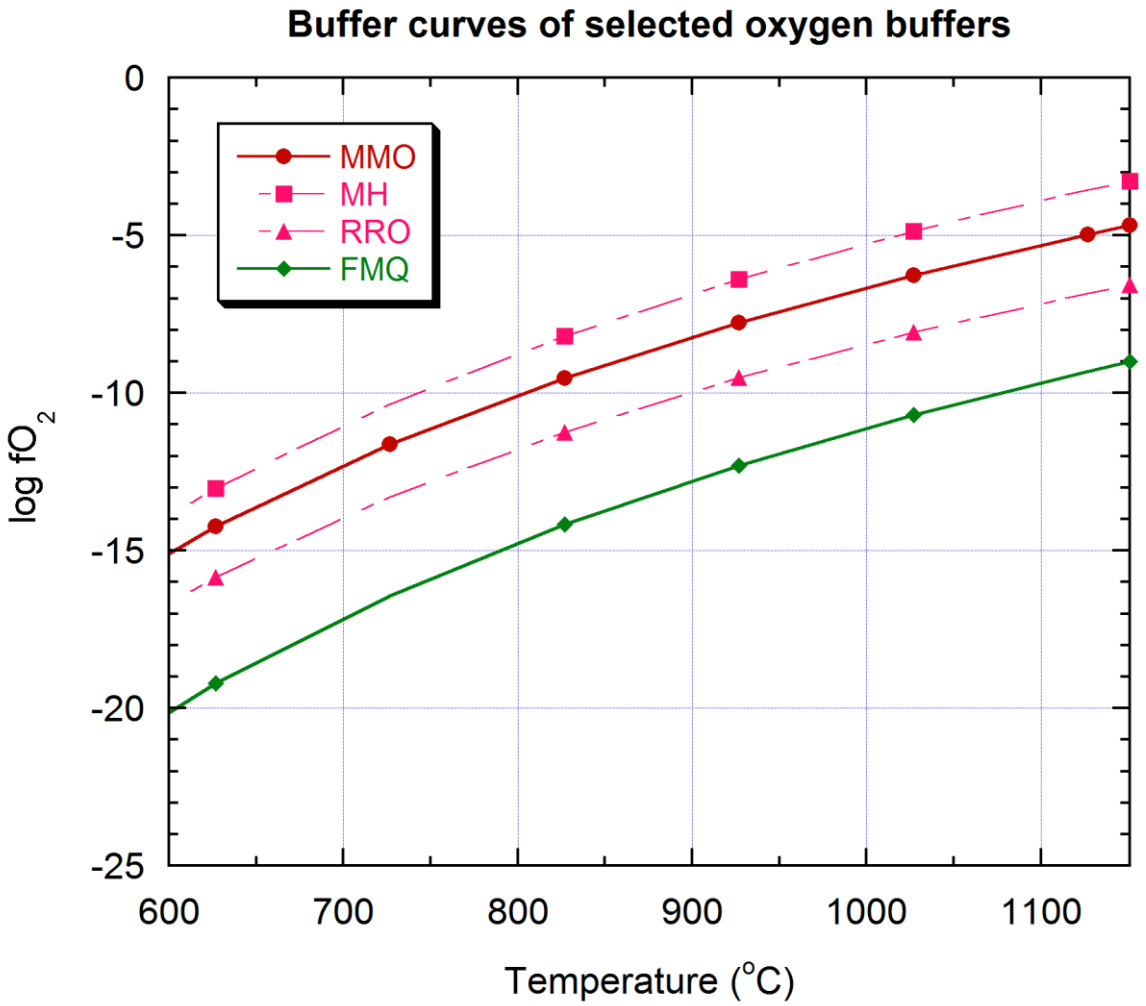

Figure 22. Buffer curves for relevant oxygen buffers in this work. References for the MMO and FMQ buffers are found in Figure 21. Magnetite-hematite (MH): Myers and Eugster, 1983; Re-ReO_2 (RRO): Pownceby and O'Neill, 1994.

3. Analytical methods

3.1. Sample preparation

In the phase equilibrium experiments, the quenched run products were broken open to remove the solid Cu-rich sulfide material. Some samples were easily removed as a metallic button, and others remained stuck to the silica tube. In the centrifuge and buffered fusion experiments, entire silica tubes and magnetite capsules were mounted.

Run products were mounted in epoxy in 1" polycarbonate rings, then ground with progressively finer waterproof sandpaper and SiC grit paper to expose a cross-section of the quenched sulfide. Sectioned samples were subsequently polished with 1 and 0.3 µm alumina. Centrifuged samples in particular were first polished with 9 then 1 µm diamond suspension prior to polishing with 0.3 µm alumina.

3.2. Scanning Electron Microscopy

Samples were first examined with reflected light microscopy for preliminary observations of textures and homogeneity. Samples were then carbon coated in preparation for analyses on the scanning electron microscope (SEM). Characterization of run product textures was performed using a JEOL JSM-6610LV SEM at the Department of Geology at the University of Toronto. Samples were typically imaged with backscattered electrons (BSE) to highlight textures and phases of different compositions. Beam conditions were 15 to 20 kV accelerating voltage, 0.8 nA specimen current, and 50 to 60 spot size at a 12 mm working distance. Major element concentrations were measured with an Oxford Instruments energy dispersive spectrometry (EDS) detector that complements this SEM system. The EDS detector is a 20 mm^2 silicon drift detector (SDD) with a 35° takeoff angle and a 0.3 µm ultra thin Mylar window. Three to four point analyses were done for samples with homogenous textures. Where quench textures were observed, analyses were done over an area defined by a rectangle. Any holes or bubbles were avoided in both cases. Data acquisition lasted 30 s, with total counts typically reaching 28 kcps.

3.3. Laser Ablation Inductively Coupled Plasma Mass Spectrometry

Trace element concentrations were determined by laser ablation inductively coupled plasma mass spectrometry (LA ICP-MS) at the Department of Geology at the University of Toronto. This system employs a frequency-quintupled Nd:YAG laser operating at 213 nm with a VG PQ Excell quadropole ICP-MS. He was used as a carrier gas, flushing the sample cell throughout the analyses. Analyses were acquired using factory-supplied time-resolved software (ThermoElectron PlasmaLab). Analyses were collected in blocks of 12 and 14 (bornite and chalcocite fusion samples, respectively), with the first and last two spectra collected on an in-house sulfide standard reference material (mss5).

Analyses were obtained using a laser output of 60%, repetition rate of 4 Hz, scan rate of 20 µm/s, and a line of 40 to 75 µm beam width. Prior to data acquisition, the surface was of the sample was pre-cleaned by passing the laser beam twice over the surface. The ablation cell was then allowed to flush this material out for at least 60 s. A typical analysis consisted of 20 s of background collection (laser off), followed by 60 s of laser ablation of the sample (laser on). The following isotopes were measured: ^{33}S, ^{197}Au, ^{185}Re, and ^{187}Re. Both isotopes of Re were measured to check for interferences of ^{187}Os on ^{187}Re (possibly from contamination during sample preparation). Both isotopes yielded very similar concentrations, suggesting that there was no interference of ^{187}Os on ^{187}Re.

Data reduction was performed using GLITTER version 5.3.1 with ^{33}S as an internal standard. S concentrations (wt. %), as determined by EDS, were converted to SO concentrations (wt. %) to correct for ablation yields. ^{185}Re and ^{187}Re spectra, in particular, showed inconsistent counts likely due to micronuggets. Only those regions with the lowest counts were selected for data reduction. Concentrations obtained from only ^{185}Re were used in our sulfide solubility and partitioning calculations.

3.4. Powder X-ray Diffraction

The stability of the MnO-Mn_3O_4 solid oxygen buffer was checked with powder X-ray diffraction (XRD). After the experiment, the buffer mixture was recovered and finely ground under ethanol in an agate mortar. Powdered buffers were analyzed with a Philips Powder Diffractometer at the Department of Geology at the University of Toronto. This system has a Cu X-ray tube operating at an accelerating voltage of 40 keV and a current of 40 mA. Spectra were acquired from 25 to 65°, at a step size of 0.02° at 2 s per step (2θ values). Identification of phases was done with XPert Quantify software and the ICDD Powder Diffraction File 1998 database.

4. Results and discussion

4.1. Thermal stability of Cu-rich sulfide compositions

4.1.1. Phase equilibrium experiments

Our phase equilibrium experiments were a first-order approach in determining sub-solidus conditions for our sulfide compositions. Tables 5 and 6 provide summaries of the initial compositions and run conditions and compositions of these experiments, respectively. Samples with clear quench textures confirmed the existence of a liquid phase at run conditions, but those that were homogenous were ambiguous as to whether they were solid or liquid phases.

At both 1200 and 1100°C, Compositions 2 and 3 shows extensive liquid quench textures as fine lamellae or blebs (Figures 24, 25, 29 and 30) . It is interesting to note that the quenched phases are Cu-rich (Cu/S > 1) in the more Cu-poor composition (2), and Cu-poor (Cu/S < 1) in the Cu-rich composition (3). Our results for these compositions agree with the Cu-Fe-S phase diagram of Kullerud et al. (1969), at least at their highest temperature of 1100°C (Figure 5), where these compositions lie in the field of liquid. At 1200°C, the field of liquid is expected to expand and liquid phases should still be observed.

In contrast, homogeneity is observed in Compositions 1, 4 and 5 at both 1200 and 1100°C (Figures 23, 27, 28 and 31), and stoichiometric bornite at 1300 and 1200°C (Figure 32). The absence of liquid quench textures in these homogenous samples, however, does not mean that these were truly solid or crystalline during run conditions. For example, Composition 1 lies in the field of liquid at 1100°C (Figure 5), and should remain liquid at higher temperatures of 1200°C. It is therefore unclear whether Compositions 4 and 5 are liquid or not at these temperatures.

Compositions 6, 7 and 8, which lie in between Compositions 4 (solid/liquid) and 3 (liquid), were run at 1200°C to see whether we could find co-existing solid and liquid phases in the same sample. We found textures in Composition 6 very difficult to interpret (Figure 26a). It is possible that the ovoid masses are solid and are surrounded by melt, or both phases are melt. From the 1100°C phase diagram in Figure 5, Composition 6 lies in the field of liquid. At the actual run temperature of 1200°C, this composition should be liquid as the field of bornite solid solution is expected to only decrease at higher temperatures and not extend out into this composition. The pervasive liquid textures in Compositions 7 and 8 (Figure 26, b and c) suggest that these samples, at least, are liquid.

Table 5. Summary of initial compositions and run conditions of the phase equilibrium experiments.

Experiment ID	Composition[a]	Composition based on starting materials (wt. %)		Composition (wt. %)			Temperature (°C)	Run duration (hours)	Method of quenching
		Cu-Fe-S liquid (1)	Chalcocite (5)	Cu	Fe	S			
1200°C isotherm									
BN1200-1-1[b]	1	100		35	33.4	31.6	1202	3	H_2O-NaCl-H_2O_{ice}
BN1200-1-2	1	100		35	33.4	31.6	1202	3	H_2O-NaCl-H_2O_{ice}
BN1200-2a	2	74.42	25.58	46.83	24.50	28.67	1202	15.25	Cold water
BN1200-3a	3	56.59	43.41	54.75	18.63	26.63	1202	15.25	Cold water
BN1200-6	6	25.97	74.03	59.05	15.44	25.51	1202	14.5	Cold water
BN1200-7	7	36.43	63.57	63.69	11.99	24.31	1202	14.5	Cold water
BN1200-8	8	46.9	53.1	68.33	8.55	23.12	1202	14.5	Cold water
BN1200-4a	4	15.5	84.5	72.98	5.10	21.92	1202	15.25	Cold water
BN1200-5a	5		100	79.86		20.14	1202	15.25	Cold water
1100°C isotherm									
BN1100-1	1	100		35	33.4	31.6	1101	19.25	Cold water
BN1100-2	2	74.42	25.58	46.83	24.50	28.67	1101	19.25	Cold water
BN1100-3	3	56.59	43.41	54.75	18.63	26.63	1101	19.25	Cold water
BN1100-4	4	15.5	84.5	72.98	5.10	21.92	1101	19.25	Cold water
BN1100-5	5		100	79.86		20.14	1101	19.25	Cold water
Runs with bornite									
Bornite-1300	Stoichiometric bornite			63.32	11.13	25.56	1301	1.25	Cold water
Bornite-1200	Stoichiometric bornite			63.32	11.13	25.56	1201	3.5	Cold water

[a]*See coloured dots in Figure 5*

[b]*Used thicker-walled silica tubing (3 mm ID x 8 mm OD)*

Table 6. Compositions of run products of the phase equilibrium experiments.

Experiment ID	n	Cu	Fe	S	Total
1200°C isotherm					
BN1200-1-1	4	33.77(0.23)	32.03(0.18)	34.19(0.15)	100.00
BN1200-1-2	3	32.69(0.27)	32.37(0.21)	34.95(0.18)	100.00
BN1200-2a	4	43.96(0.22)	24.49(0.17)	31.55(0.15)	100.00
BN1200-3a	3	52.94(0.24)	18.32(0.17)	28.74(0.17)	100.00
BN1200-6	3	59.22(0.23)	13.97(0.16)	26.8(0.17)	100.00
BN1200-7	4	63.12(0.19)	11.07(0.13)	25.82(0.14)	100.00
BN1200-8	3	67.51(0.20)	8.14(0.13)	24.35(0.16)	100.00
BN1200-4a	3	70.82(0.19)	5.14(0.12)	24.03(0.16)	100.00
BN1200-5a	3	78.03(0.15)		21.97(0.15)	100.00
1100°C isotherm					
BN1100-1*	3	40.01(0.09)	28.91(0.08)	31.08(0.06)	100.00
BN1100-2	5	43.50(0.48)	25.63(0.36)	30.87(0.327)	100.00
BN1100-3	4	52.78(0.20)	18.19(0.15)	29.04(0.14)	100.01
BN1100-4	3	71.64(0.18)	5.04(0.11)	23.32(0.15)	100.00
BN1100-5*	3	81.44(0.05)		18.56(0.05)	100.00
Runs with bornite					
Bornite-1300	3	62.42(0.21)	10.03(0.13)	27.56(0.16)	100.00
Bornite-1200	4	62.03(0.18)	10.26(0.12)	27.71(0.14)	100.00

Analyses are reported in wt. %. Numbers in parentheses refer to the standard deviations of n analyses.

** Analyses where the L-line for Cu was used (K-line was used in most analyses).*

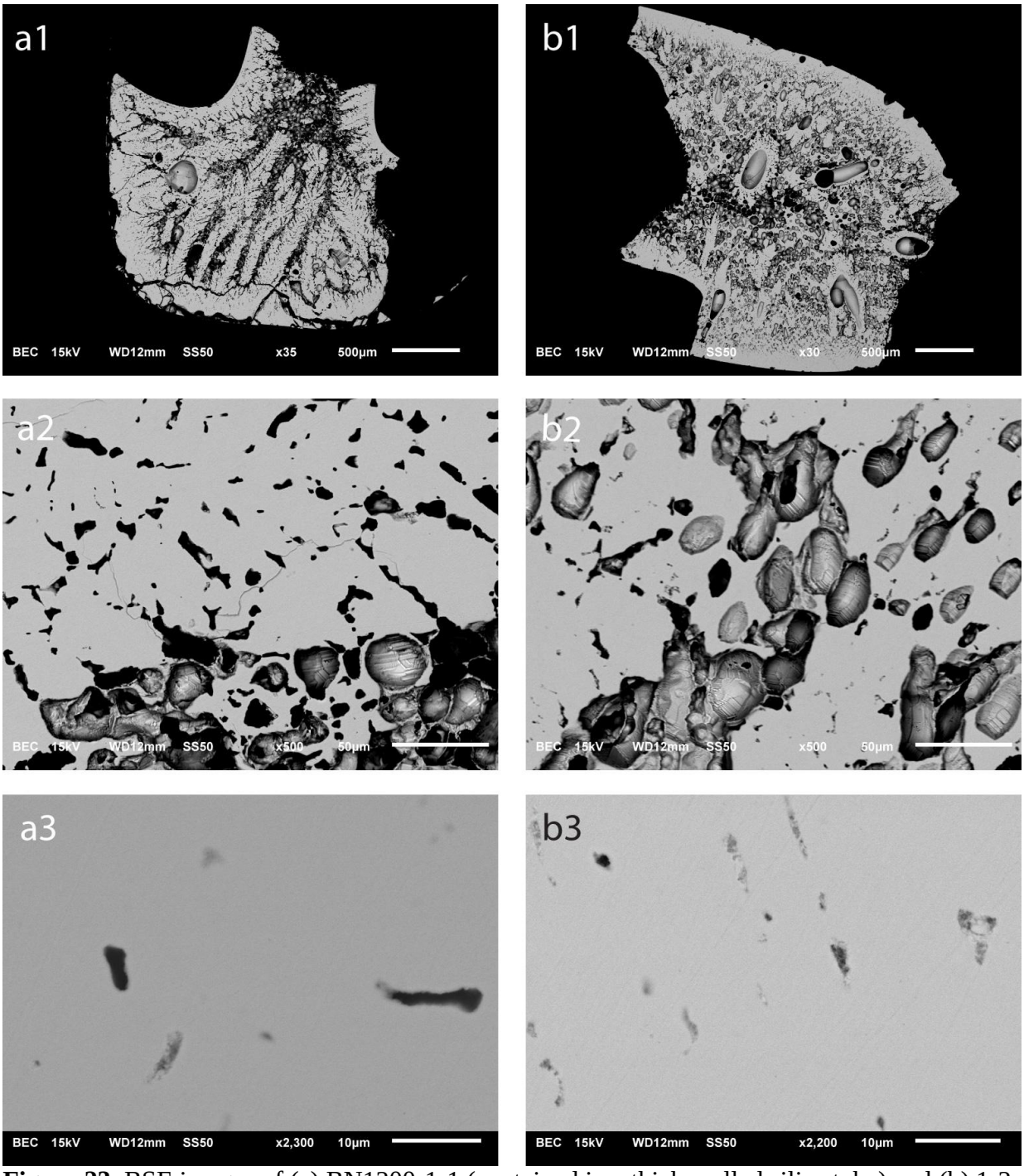

Figure 23. BSE images of (a) BN1200-1-1 (contained in a thick-walled silica tube) and (b) 1-2 (thin-walled) showing no difference in textures at different magnifications (1 to 3). Samples are homogenous, display no quench textures, and have pervasive bubbles.

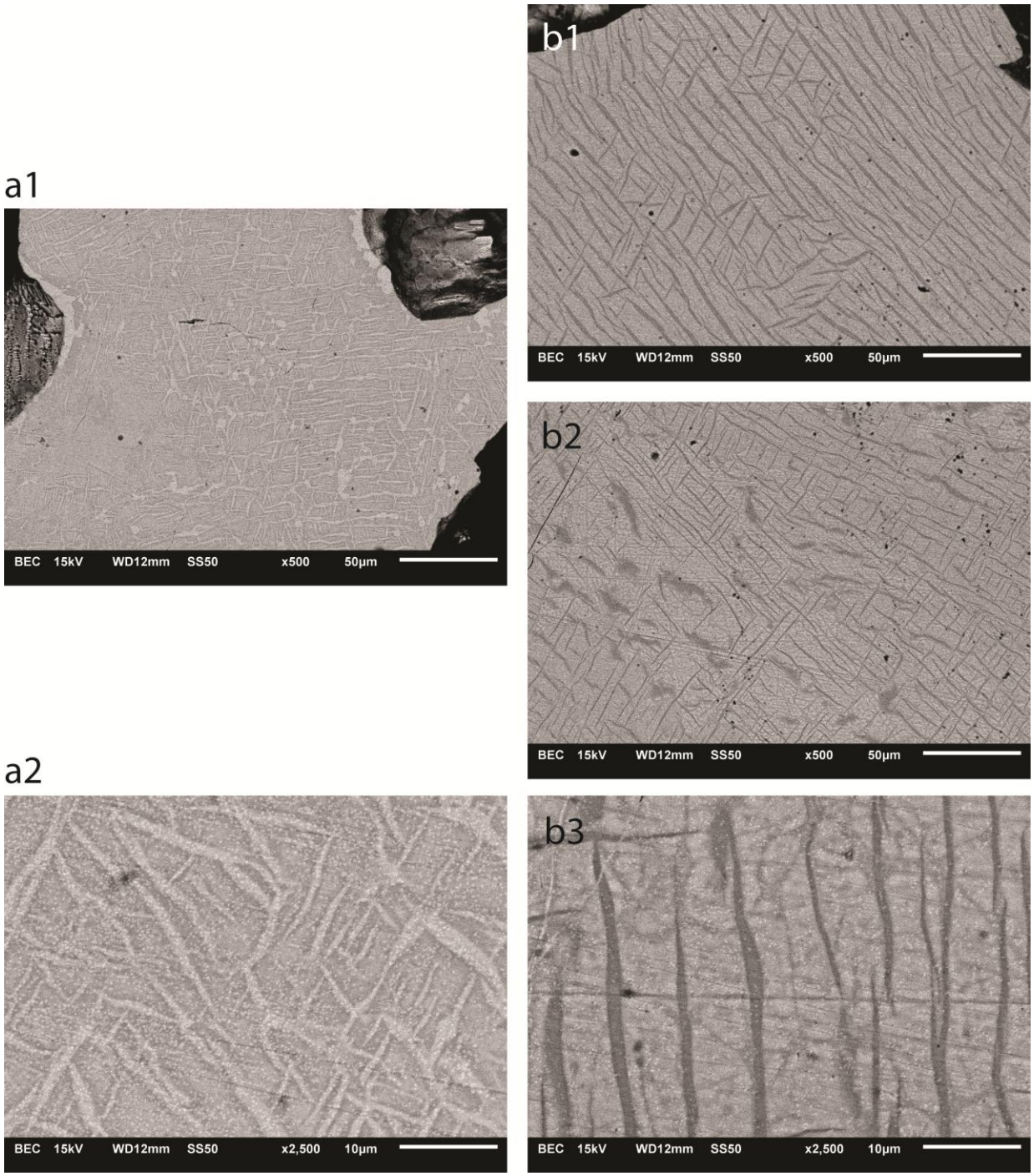

Figure 24. BSE images of (a) BN1200-2a and (b) BN1200-3a clearly showing inhomogeneity within the sample. At 500x (a1, b1, b3), lamellae resulting from quench and/or exsolution are evident throughout. The colour (composition) of the lamellae is also different depending on the amount of Cu in the sulfide (relatively Cu-rich lamellae in Cu-poor sulfide, and vice-versa). At higher magnifications of 2500x (a2, b3), sub-micron-sized dots are observed over the main lamellae and surrounding matrix. In a2 in particular, the light-coloured main lamellae seem to be outlined by a darker phase. In b3, there are thinner lamellae together with the thicker, main lamellae observed at lower magnifications. It is unclear whether these thinner lamellae overprint or are cross-cut by the main lamellae.

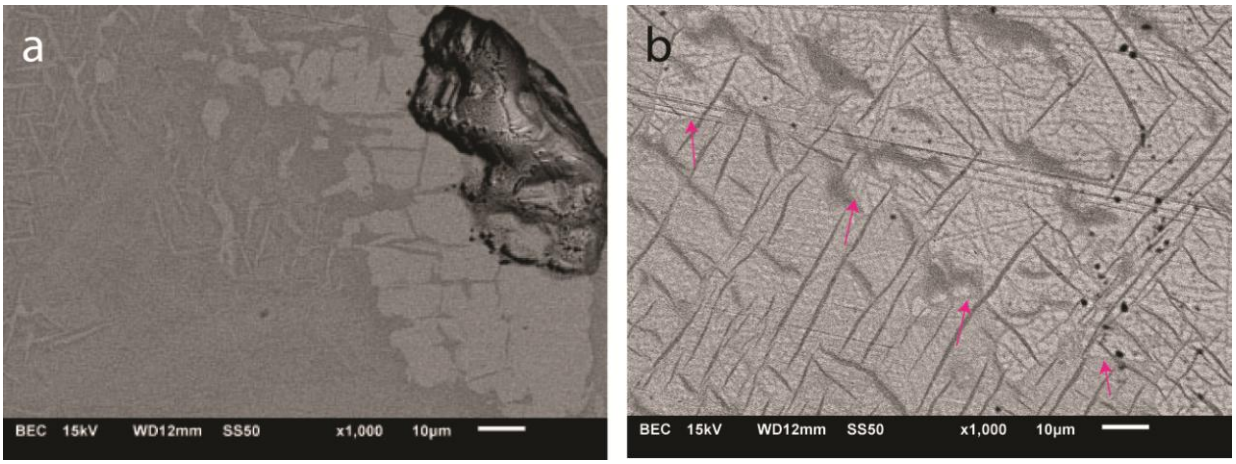

Figure 25. BSE images of (a) BN1200-2a and (b) BN1200-3a at 1000x (intermediate of magnifications shown in Figure 24). Domains relatively richer in Cu exist within the sample, as shown by the lighter colour of these domains (in b, the outline is shown by pink arrows).

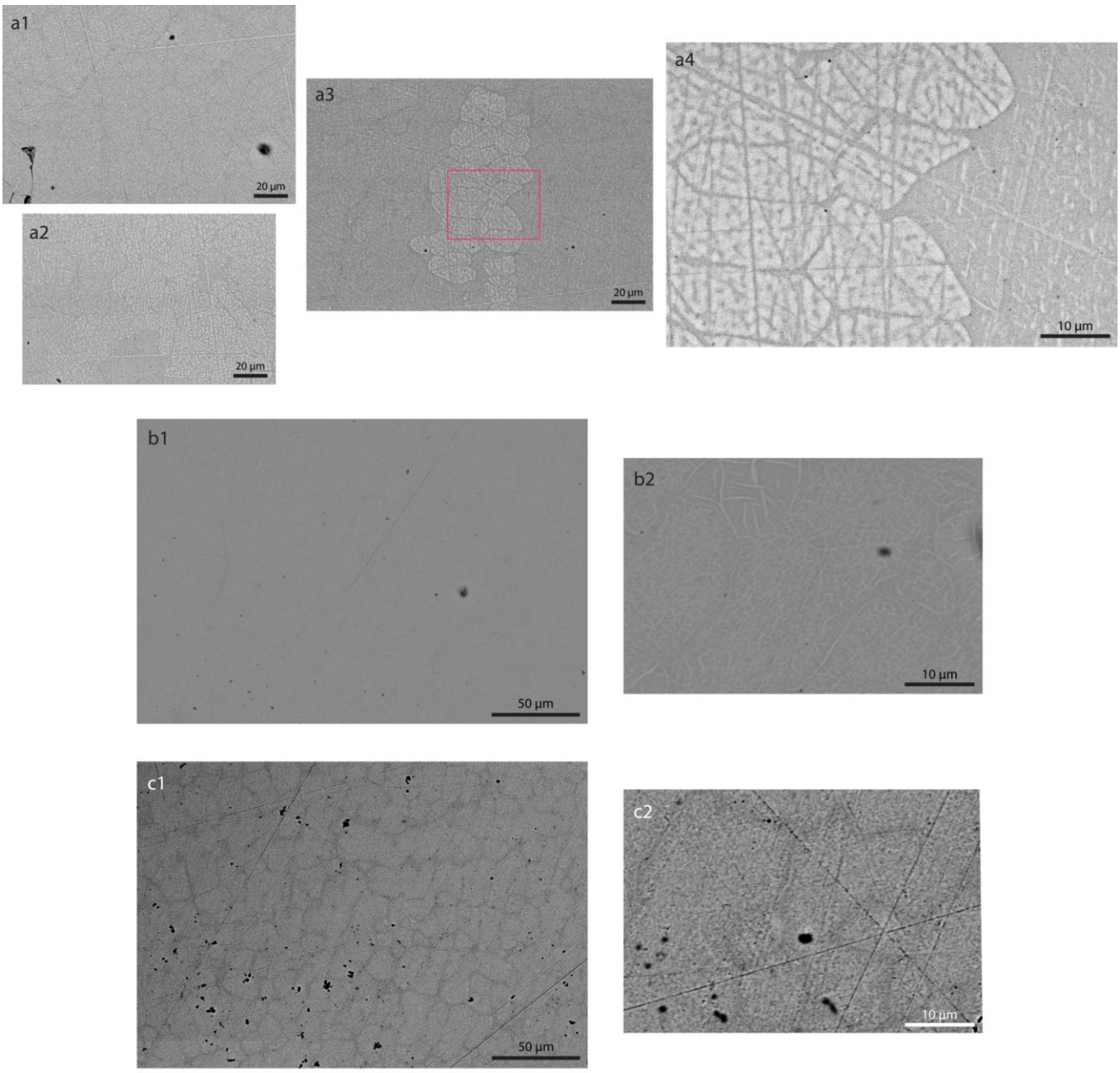

Figure 26. BSE images of (a) BN1200-6, (b) BN1200-7, and (c) BN1200-8 showing liquid quench textures. (a) BN1200-6: a1 and a2 show complex ovoid-shaped masses in the melt (solid phases?). a3 shows a smaller aggregate, with a pink box magnifying its contact with the surrounding melt in a4. Inhomogeneity still exists within the ovoid masses and the melt. (b) BN1200-7 and (c) BN1200-8: Less complex quench textures found mainly on the margins of ovoid domains. The domains are smaller and the outlines are lighter (more Cu-rich) in b.

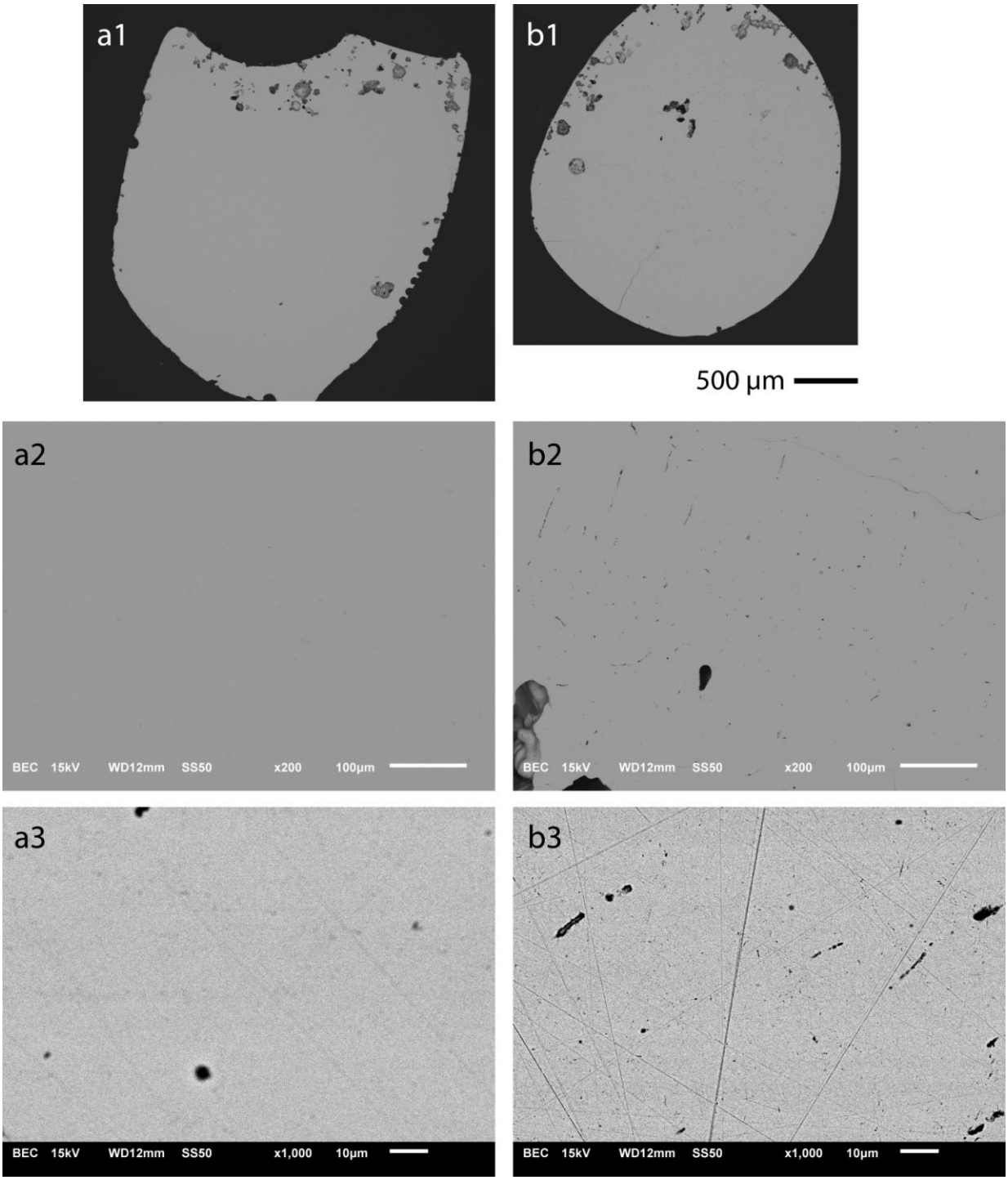

Figure 27. BSE images of (a) BN1200-4a and (b) BN1200-5a showing homogeneity and the absence of quench or exsolution textures. Vesicles are concentrated at the top of the samples (a1 and b1), and are much less pervasive that the Cu-poor, Fe-bearing samples (e.g., BN1200-1, Figure 23, a1 and b1).

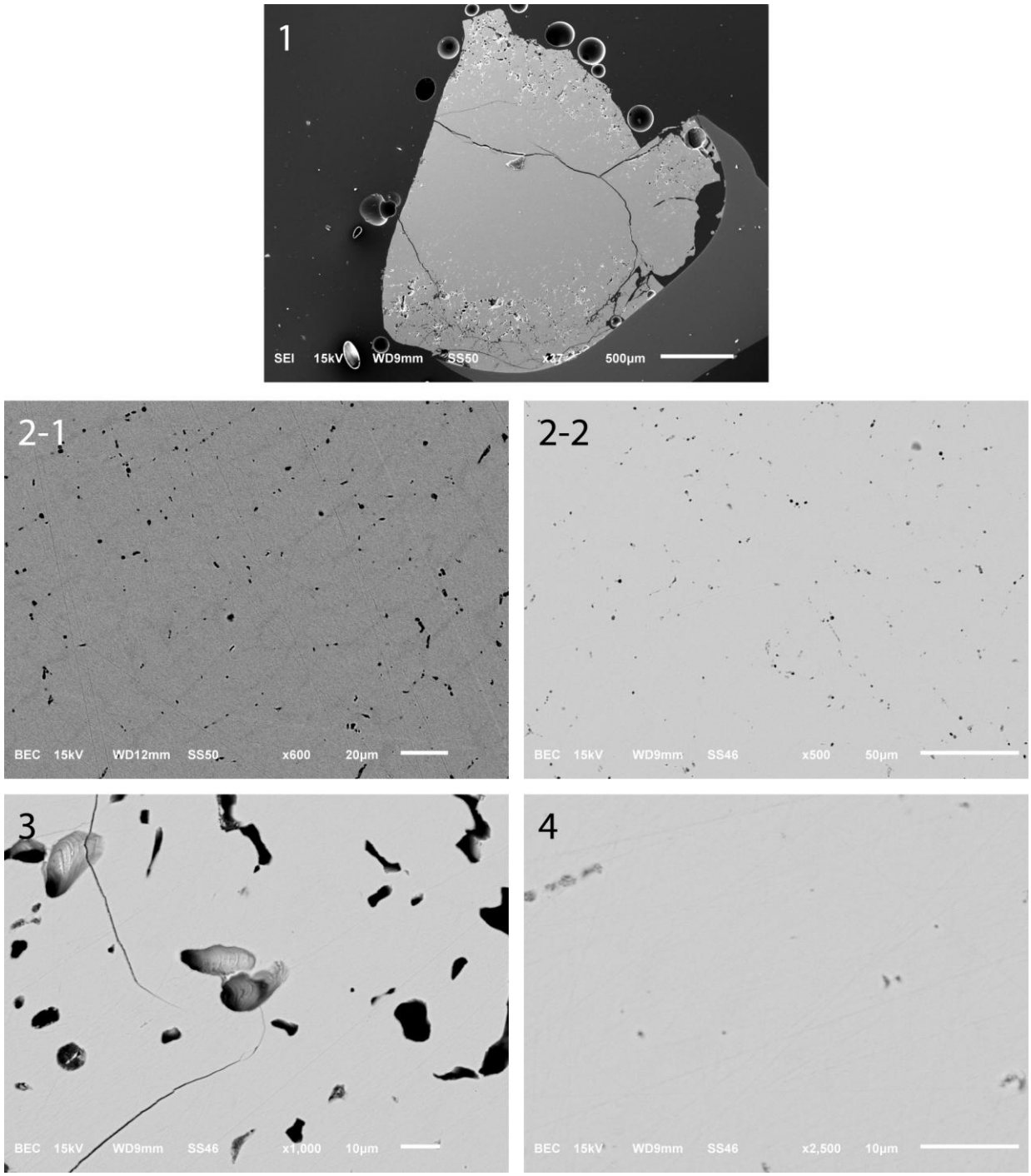

Figure 28. BSE images of BN1100-1. (1) The entire sectioned sampled at low magnification. (2-1) At 600x, dark-coloured rims around ovoid phases can be observed. It is ambiguous whether the rims were formed from a quenched liquid or are grain boundaries. This texture is similar to that observed in BN1200-8 (Figure 26c1). (2-2) to (4) Rims were not observed with higher brightness settings, instead the sample seemed homogeneous.

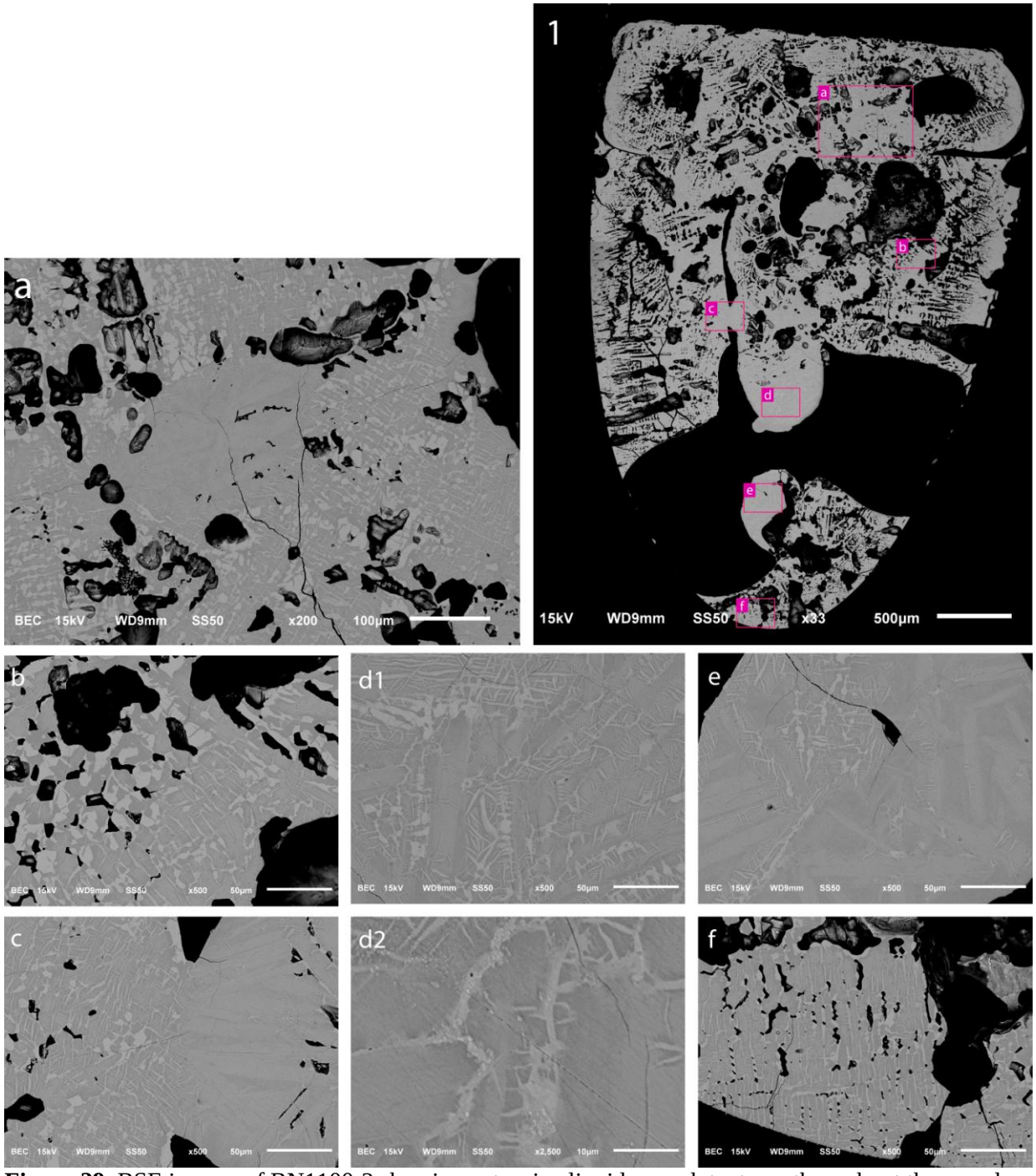

Figure 29. BSE images of BN1100-2 showing extensive liquid quench textures throughout the sample. (1) View of the entire sectioned sample indicating areas shown in a to f. (a) At low magnifications, quench textures are evident as light-coloured blebs and lamellae. Also shown in the middle of the image is an area devoid of blebs and lamellae, but have lath-like phases present. (b) to (f) Same textures mentioned in a at 500x (except d2 which is at 2500x) at different areas of the sample. The distribution of textures is not uniform. For example, in c, a region dominated by lath-like phases terminates against a region dominated by blebs and lamellae. (d2) Area in d1 shown at higher magnification showing fine light-coloured dots nucleating on lamellae found on the margins of the lath-like phases. This could represent another stage or scale of quenching.

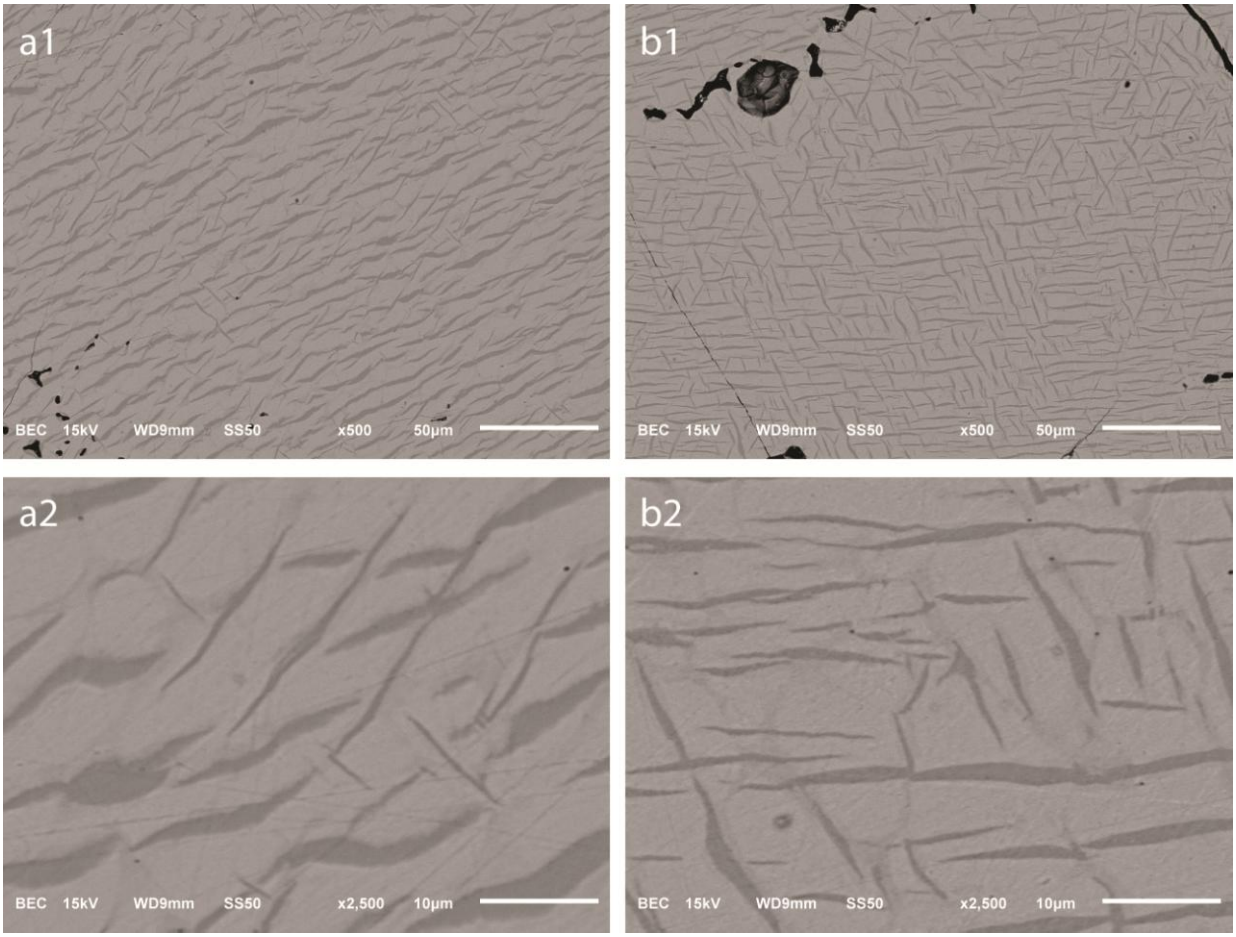

Figure 30. BSE images of BN1100-3 showing extensive liquid quench textures. (a1) and (b1) Dark-coloured lamellae are found throughout the sample in various orientations. (a2) and (b2) Fields of view in a1 and b1 at higher magnifications showing wispy grey phases together with the main dark lamellae. Cross-cutting relationships are not clear (i.e., whether the former is overprinting the latter, or vice-versa). The grey phase also seems to be rimming the main dark lamellae, at least locally in a2.

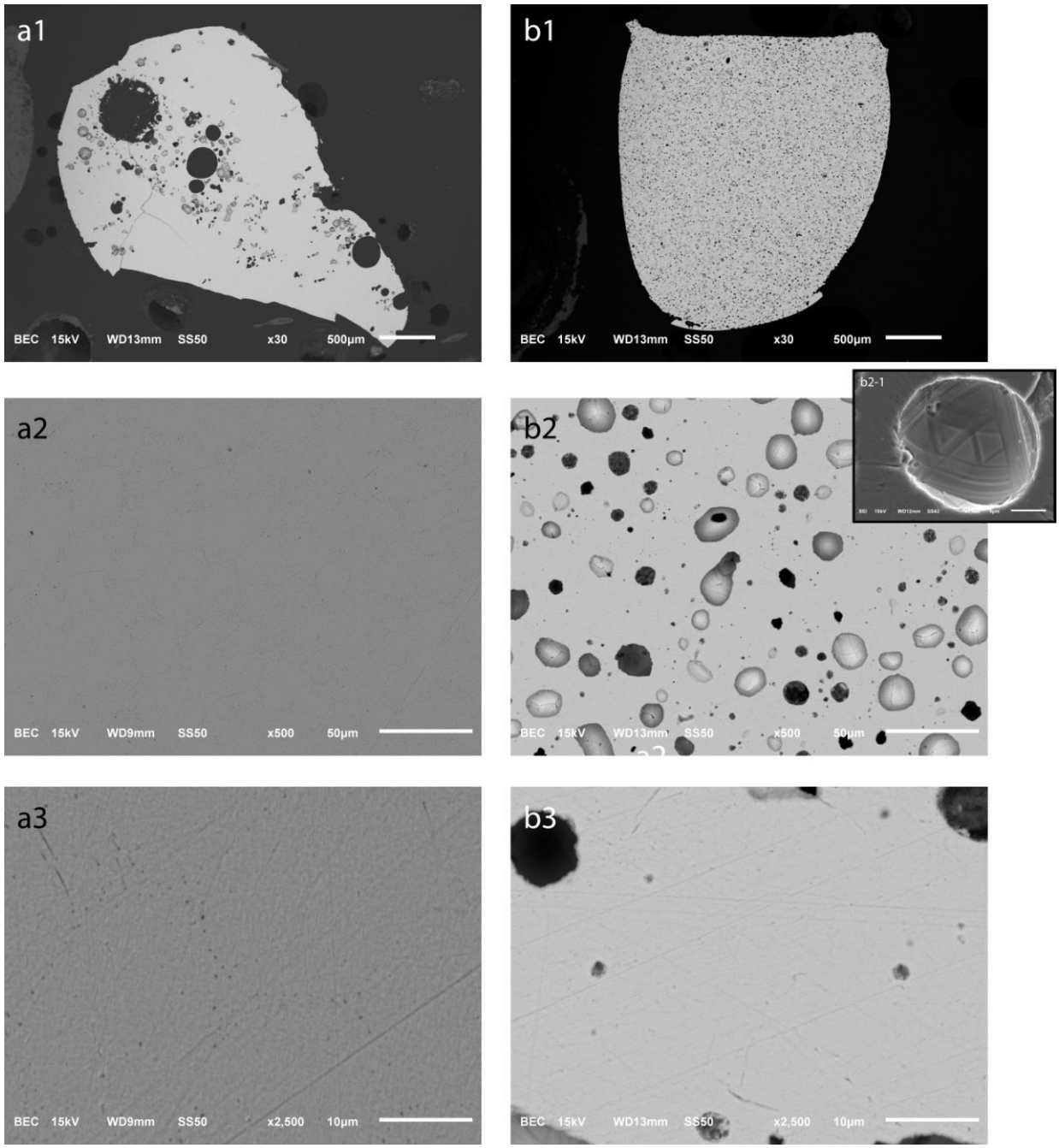

Figure 31. BSE images of (a) BN1100-4 and (b) BN1100-5 showing homogeneity at various scales of the sample. (b1) and (b2) BN1100-5 has a uniform distribution of fine vesicles throughout the sample. (b2-1) SEI image of a typical vesicle.

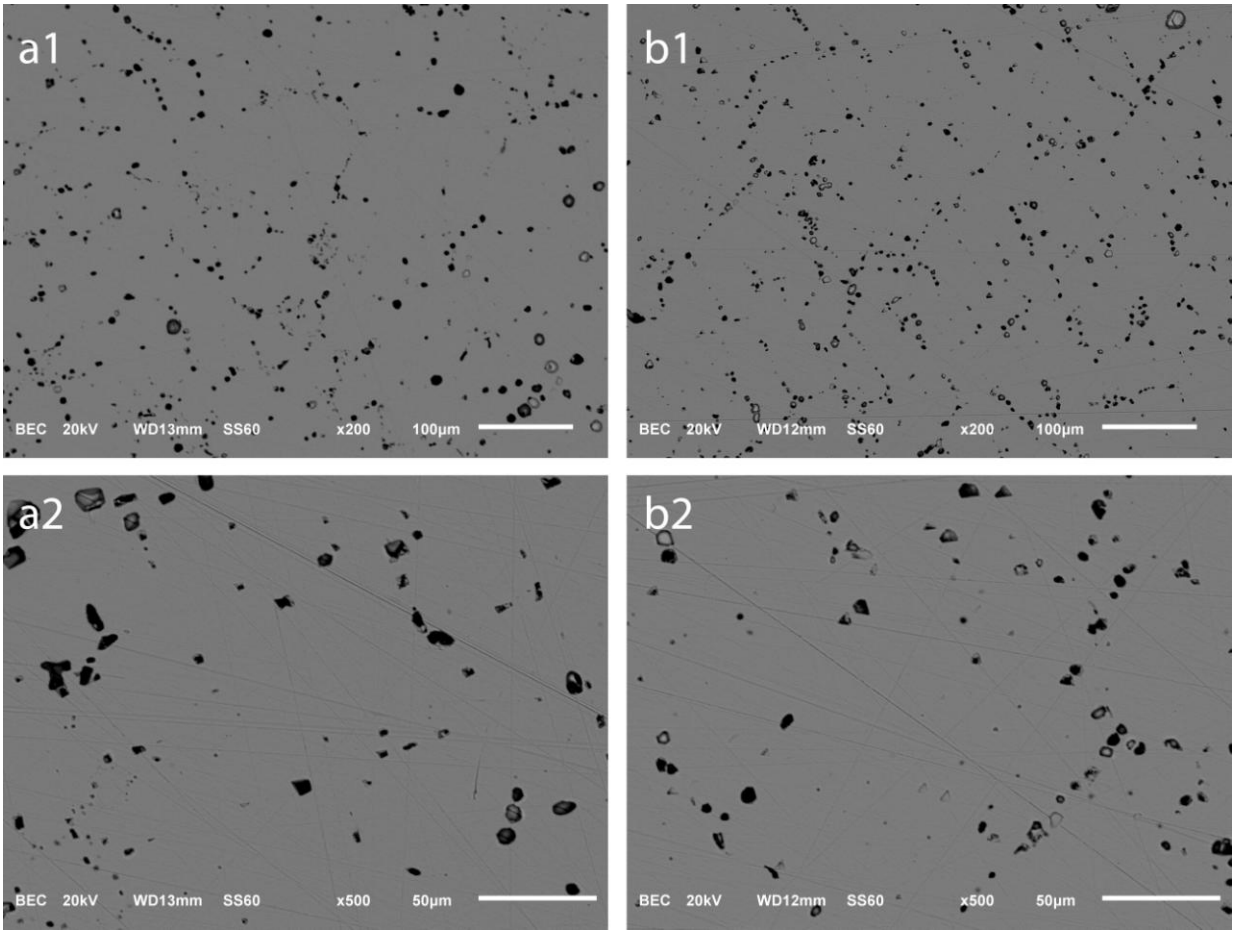

Figure 32. Stoichiometric bornite compositions run at (a) 1300 and (b) 1200°C showing clear homogeneity and no obvious liquid quench textures. Black dots throughout are bubbles/holes in the sample.

4.1.2. Centrifuge experiments

In our difficulty in interpreting liquid quench textures or absence thereof, we focused on our main goal of determining the highest temperature at which our sulfide compositions would be solid. Results from our centrifuge experiments involving bornite and chalcocite were much less ambiguous. Tables 7 and 8 summarize the run conditions and compositions of these experiments. Figures 33 to 37 are reflected light photomicrographs of the run products (detailed textures of which are found in Appendix 1). At 1200 and 1100°C, bornite was clearly liquid, as it coalesced into a globule in the static run and replaced the silica powder at the bottom of the ampoule in the centrifuge run (Figures 33 and 34). This agrees with the Cu-Fe-S phase diagram

of Kullerud et al. (1969) (Figure 2a) where stoichiometric bornite plots in the field of liquid at 1100°C. Although no data exists for phase relations above 1100°C, bornite is still likely liquid at 1200°C. Chalcocite is also observed to be liquid at 1100°C (Figure 35), although Kullerud et al. (1969) (Figure 2a) report that it is crystalline. At a slightly lower temperature of 1050°C, chalcocite did not melt and remained solid. It did not coalesce into a globule in the static run, and did not replace silica in the centrifuge run (Figure 36). Thus, above 1100°C, bornite and chalcocite are liquid, and below 1050°C, chalcocite is solid. We did not perform an experiment at 1050°C for bornite, and so we are not certain that it is also solid at this temperature. However, at 1000°C, stoichiometric bornite plots within the field of bornite solid solution (Figure 2b). If bornite is known to be liquid at 1100°C, and solid at 1000°C, then it must transition from liquid to solid between the two temperatures. For the purposes of our buffered fusion experiments, we assumed that both chalcocite and bornite are solid phases at 1050°C.

The result of our control experiment with troilite (Figure 37a) was ambiguous, as troilite appeared to have moved to the bottom of the ampoule, surrounding some silica particles. We assumed that this was a liquid texture in all our centrifuge runs. There are also distinct grain boundaries throughout the sample which suggest that it was solid at run conditions. No grain boundaries were observed in the 1050°C chalcocite experiments (Figure 36). The result of our run with Composition 2 (Figure 37b) was in closer agreement to what we had established as liquid textures.

Table 7. Summary of static and centrifuge experiments.

Experiment ID	Composition[a]	Static step		Centrifuge step				Relative g
		Temperature (°C)	Run duration (min)	Temperature (°C)	Average temperature gradient[b]	Run duration (min)	Average rpm	
Cent1200bn-1	Bornite	1201	180					1
Cent1200bn-2	Bornite	1201	180	1200	7	33	1750	582
Cent1100bn-1a	Bornite	1100	180					1
Cent1100bn-2	Bornite	1100	180	1100	3.25	60	1793.5	611
Cent1100cc-1	Chalcocite	1101	185					1
Cent1100cc-2	Chalcocite	1101	185	1102	1	62	1686.6	541
Cent1050cc-1	Chalcocite	1050	192					1
Cent1050cc-2	Chalcocite	1050	192	1050	0.6	65	1658.4	523
Cent1100-FeS	Troilite	1100	82	1100	5	58	1696.5	547
Cent1100-Mix2	Composition 2	1100	82	1100	4.625	75	1732	570

[a]*Composition placed above silica powder*
[b]*Between the upper and lower thermocouple over the course of the experiment*

Table 8. Summary of compositions of run products of the centrifuge experiments.

Experiment ID	n	Cu	Fe	S	Total
Cent1200bn-1	3	61.66(0.21)	10.33(0.14)	28.01(0.16)	100.00
Cent1200bn-2	4	61.87(0.18)	10.17(0.12)	27.97(0.14)	100.01
Cent1100bn-1a	4	61.85(0.18)	10.36(0.12)	27.8(0.14)	100.01
Cent1100bn-2	4	62.42(0.19)	10.15(0.12)	27.44(0.14)	100.01
Cent1100cc-1	4	78.62(0.13)	-	21.39(0.13)	100.01
Cent1100cc-2	3	78.65(0.14)	-	21.35(0.14)	100.00
Cent1050cc-1	3	78.46(0.21)	-	21.54(0.21)	100.00
Cent1050cc-2	3	78.48(0.22)	-	21.52(0.22)	100.00
Cent1100-FeS	3	-	60.79(0.15)	39.21(0.15)	100.00
Cent1100-Mix2	4	43.55(0.22)	24.53(0.16)	31.93(0.15)	100.01

Reference compositions					
Stoichiometric bornite	-	63.32	11.13	25.56	100.01
Stoichiometric chalcocite	-	79.86	-	20.14	100.00
Stoichiometric troilite	-	-	63.53	36.47	100.00
Composition 2	-	46.83	24.5	28.67	100.00

Analyses are reported in wt. %. Numbers in parentheses refer to the standard deviations of n analyses.

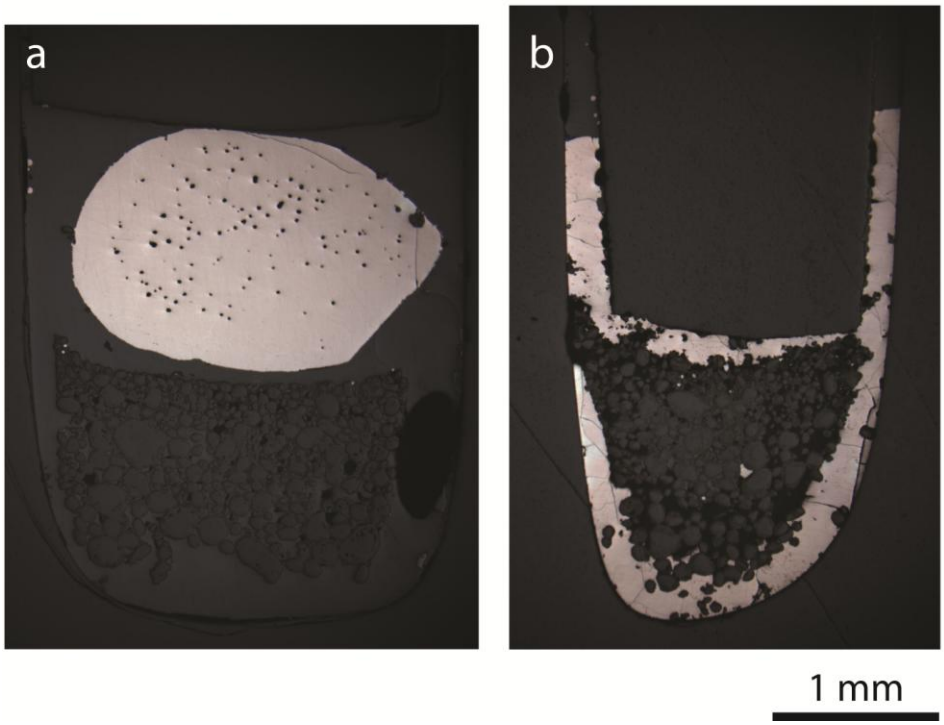

Figure 33. Reflected light photomicrographs of (a) Cent1200bn-1 (static run) and (b) Cent1200bn-2 (centrifuged run). (a) Bornite coalesced into a globule, clearly indicating that it melted and became liquid even at static run conditions. The silica powder remained packed at the bottom of the ampoule. (b) Bornite replaced the silica powder at the bottom of the ampuoule, and even rose and filled the sides of the spacer. The spacer was also lowered, as the top of the spacer was at a higher level before the run. Silica powder rose nearly to the top, and the main mass is surrounded by bornite melt.

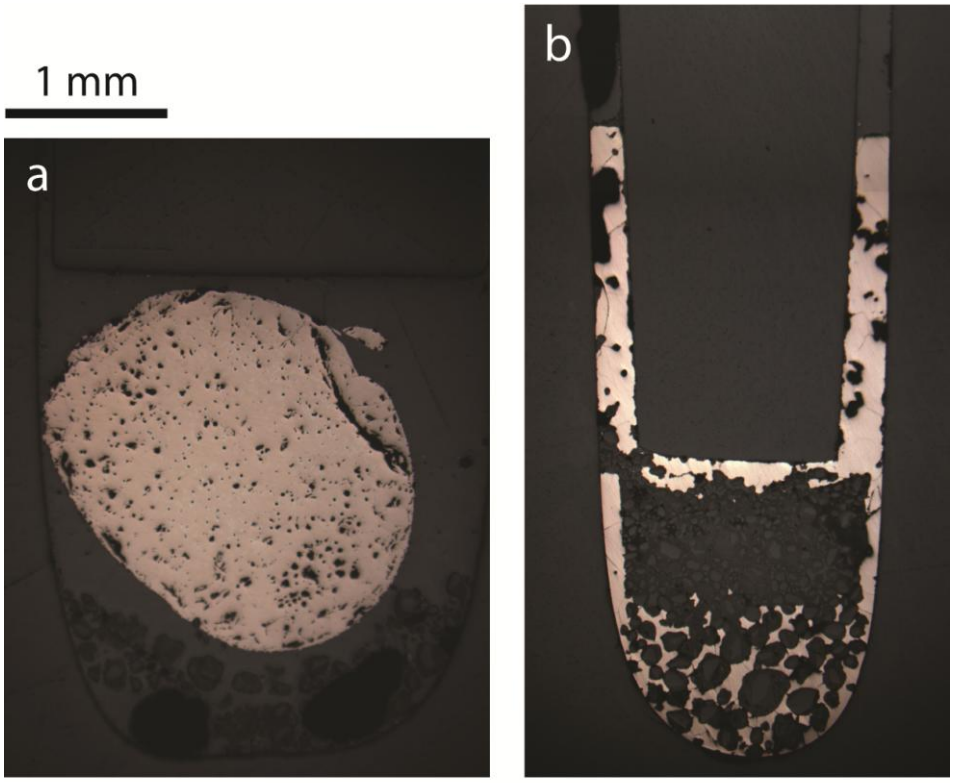

Figure 34. Reflected light photomicrographs of (a) Cent1100bn-1a (static run) and (b) Cent1100bn-2 (centrifuged run) showing the same evidence for melted bornite as observed in the Cent1200bn experiments (
Figure **33**). (a) The bornite globule was moved from its original, upright position during grinding of the mount. (b) Individual silica particles are enclosed by bornite melt as they moved from the bottom of the ampoule. A large mass of silica has risen nearly to the top.

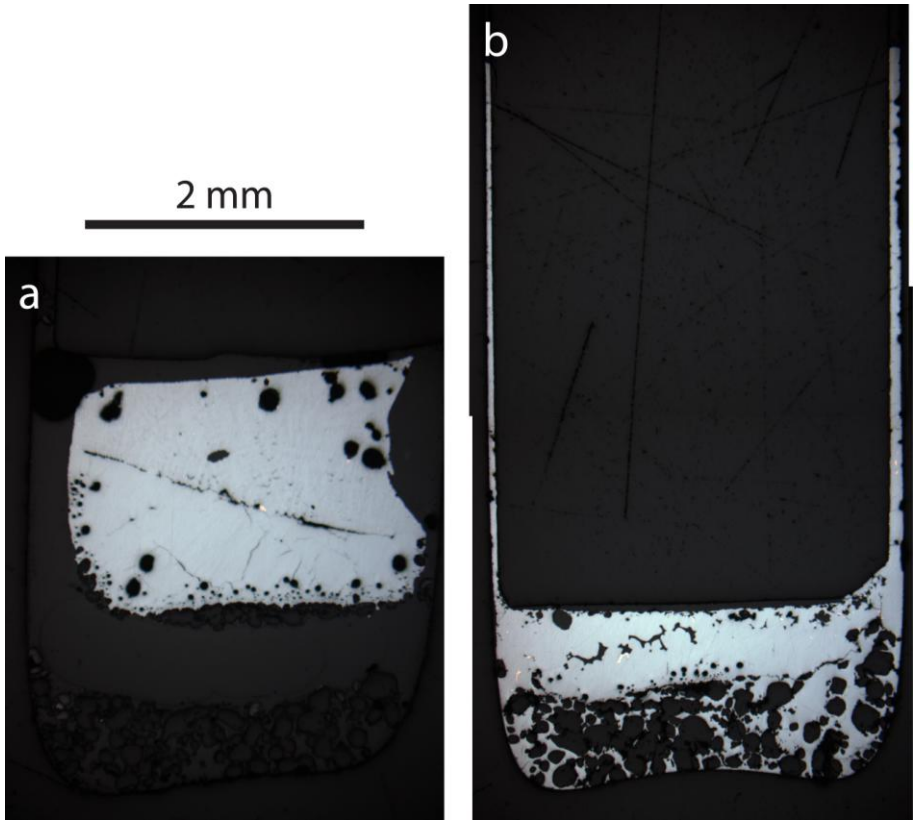

Figure 35. Reflected light photomicrographs of (a) Cent1100cc-1 (static run) and (b) Cent1100cc-2 (centrifuged run). (a) Chalcocite did not form a distinct globule like bornite when run statically (Figures 33a and 34a). Its sides have moved away from the container, which may suggest that it still melted. (b) Chalcocite has infiltrated the space between the silica powder and has risen up the sides of the spacer, providing clear evidence that it melted during the experiment.

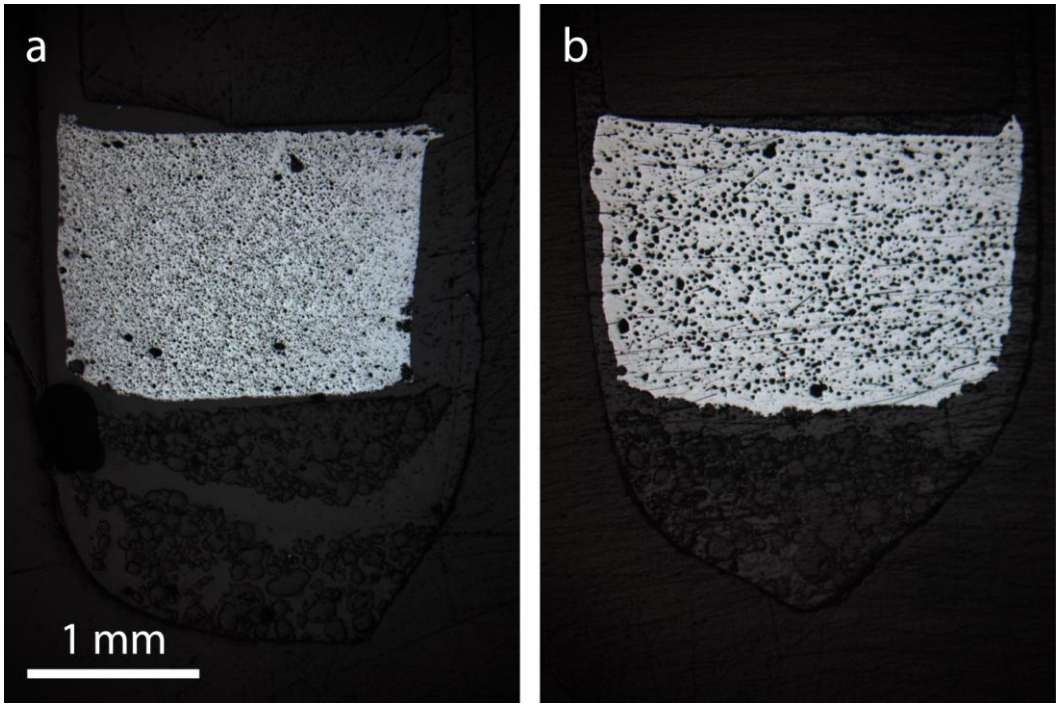

Figure 36. Reflected light photomicrographs of (a) Cent1050cc-1 (static run) and (b) Cent1050cc-2 (centrifuged run). (a) Chalcocite did not coalesce into a globule and still adheres to the sides of the ampoule. (b) Chalcocite did not move to the bottom of the ampoule. Both the chalcocite and silica powder remain in place.

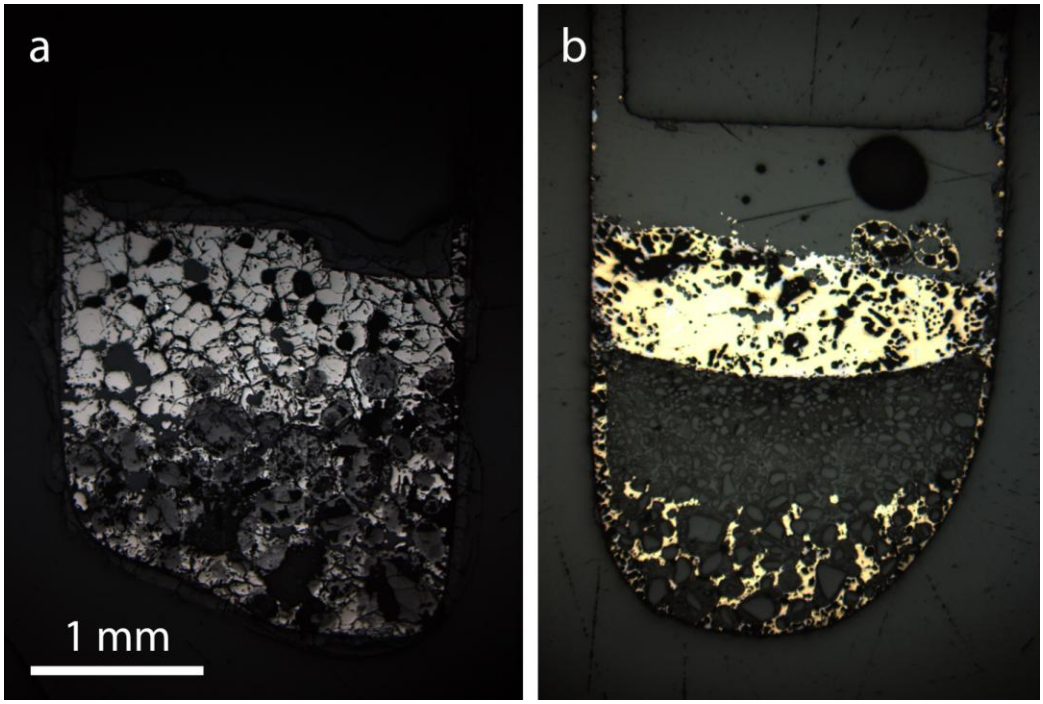

Figure 37. Reflected light photomicrographs of control samples (a) Cent1100-FeS and (b) Cent1100-Mix2, both run in the centrifuge. (a) Troilite, expected to be solid at run conditions, shows distinct grain boundaries throughout the sample. However, it surrounds individual silica powder at the bottom of the ampoule. (b) Composition 2 shows convincing liquid textures: it has replaced the silica at the bottom of the ampoule and surrounds individual silica particles that appear to be making their way to the main mass. Together with the yellow phase are purple blebs, which are likely the quench phases seen in the static equivalent of this experiment (1100°C phase equilibrium experiment, Figure 29).

4.2. Buffered fusion experiments

4.2.1. Metal-free experiments with bornite

Table 9 is a summary of the run conditions and compositions of the two buffered, "metal-free" experiments with bornite. The first experiment was actually doped with trace amounts of Au, Ag, Re and Ru (as described in Section 2.3.1.1), but we are only concerned with the bornite itself here. Our most significant finding from this experiment was that magnetite was a major phase present in equilibrium with the bornite melt (Figure 38, Table 10). The fO_2 of the experiment as defined by the MMO buffer, however, was not maintained as only MnO remained in the buffer mixture (Figure 39). As seen in Figure 40, the magnetite-hematite (MH) buffer curve is above that of MMO in a plot of log fO_2 vs. T. At the MMO buffer, the high fO_2 phase (Mn_3O_4) was likely consumed by the formation of magnetite, placing the log fO_2 range in between -4.1 (MMO) and -2.7 (MH) at 1200°C. At FMQ + 4.3 to 5.7, the experiment was at very oxidizing conditions (with FMQ + 1 as the relevant fO_2 for arc rocks). We thus found that magnetite is stable in the presence of bornite at high fO_2's, allowing us to use magnetite capsules for our subsequent experiments with bornite.

Table 9. Summary of run conditions and compositions of buffered metal-free experiments.

Experiment ID	Temperature (°C)	Run duration (hrs)	Method of quenching	Composition (wt. %)				
				n	Cu	Fe	S	Total
1200-DopedBN-MMO	1201	25	Cold water	4	63.62(0.18)	10.41(0.12)	25.98(0.14)	100.01
1100-Bornite-MMO	1100	40.25	Air cooled	6	77.99(0.10)	-	22.01(0.10)	100.00

Numbers in parentheses refer to the standard deviations of n analyses.

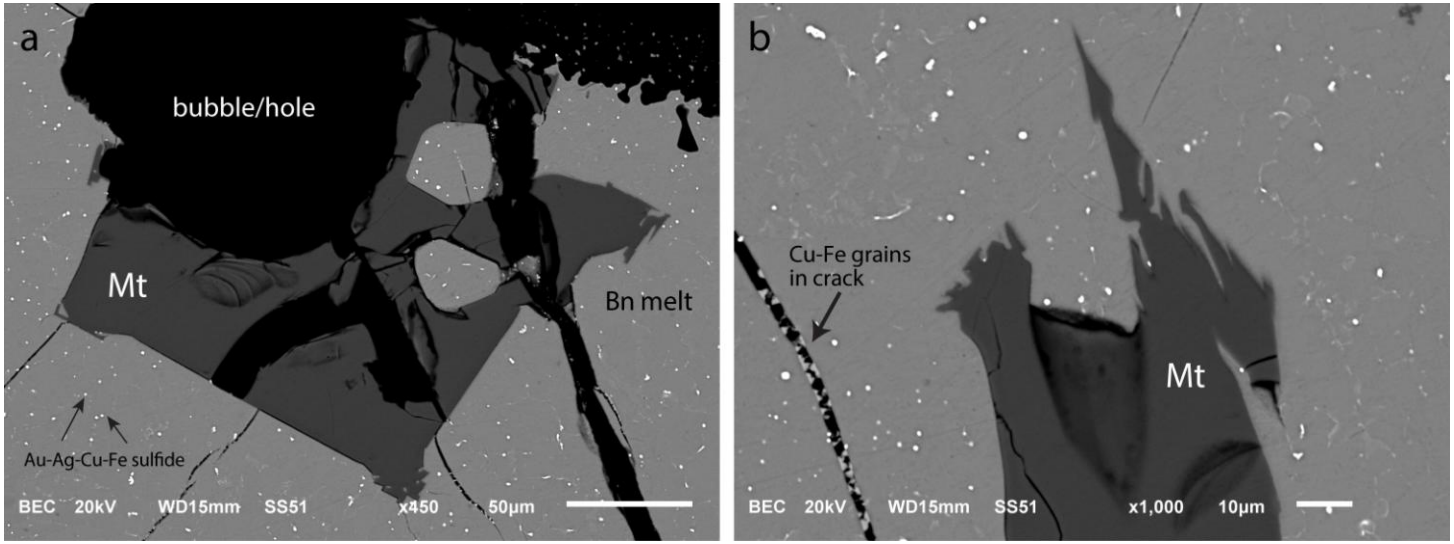

Figure 38. BSE images of 1200-DopedBN-MMO. (a) A grain of magnetite growing on the sides of a bubble/hole from the surrounding bornite melt. Bright specs and faint blebs of an Au-Ag Cu-Fe sulfide are found throughout. (b) The skeletal form of the magnetite grain suggests diffusion-controlled growth from the melt. Cracks in the sample contain Cu-Fe grains, which probably resulted from the evolution of sulfur when the sample exploded upon quench. Phase identification was done by EDS (Appendix 2).

Table 10. Magnetite analyses (in wt. % and at %).

Point	Composition in wt. %			Composition in at %		
	Fe	**O**	**Total**	**Fe**	**O**	**Total**
1	69.63(0.29)	30.37(0.29)	100.00	39.64	60.36	100.00
2	70.02(0.29)	29.98(0.29)	100.00	40.08	59.92	100.00
3	69.87(0.29)	30.13(0.29)	100.00	39.91	60.09	100.00
Average	69.84(0.17)	30.16(0.29)	100.00	39.88	60.12	100.00
Stoichiometric magnetite	77.73	22.27	100	42.86	57.14	100.00

Numbers in parentheses refer to standard deviations (for point analyses), and standard deviations of n analyses (for averages).
Results of point analyses are in fair agreement with the composition of stoichiometric magnetite, especially when expressed in at %.

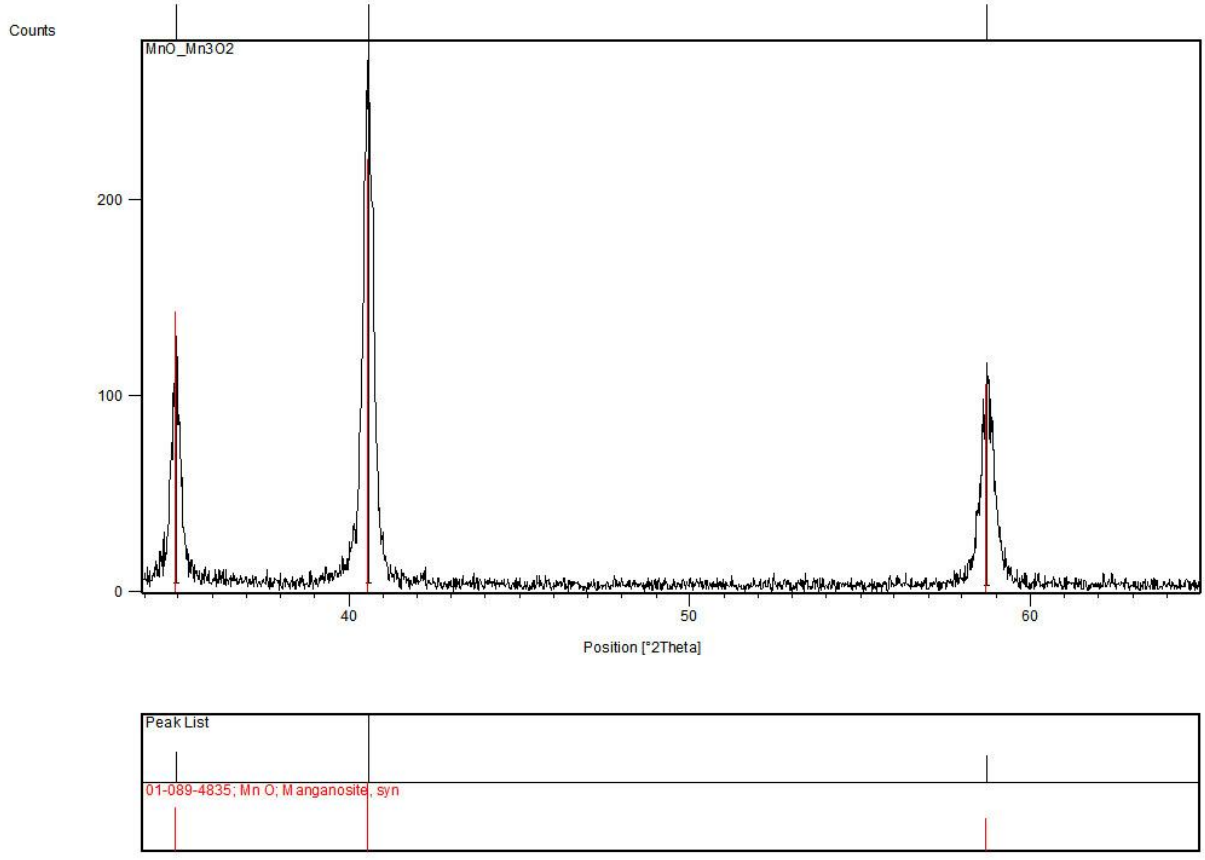

Figure 39. XRD pattern of the buffer mixture from sample 1200-DopedBN-MMO. Mn_3O_4 was not present after the experiment.

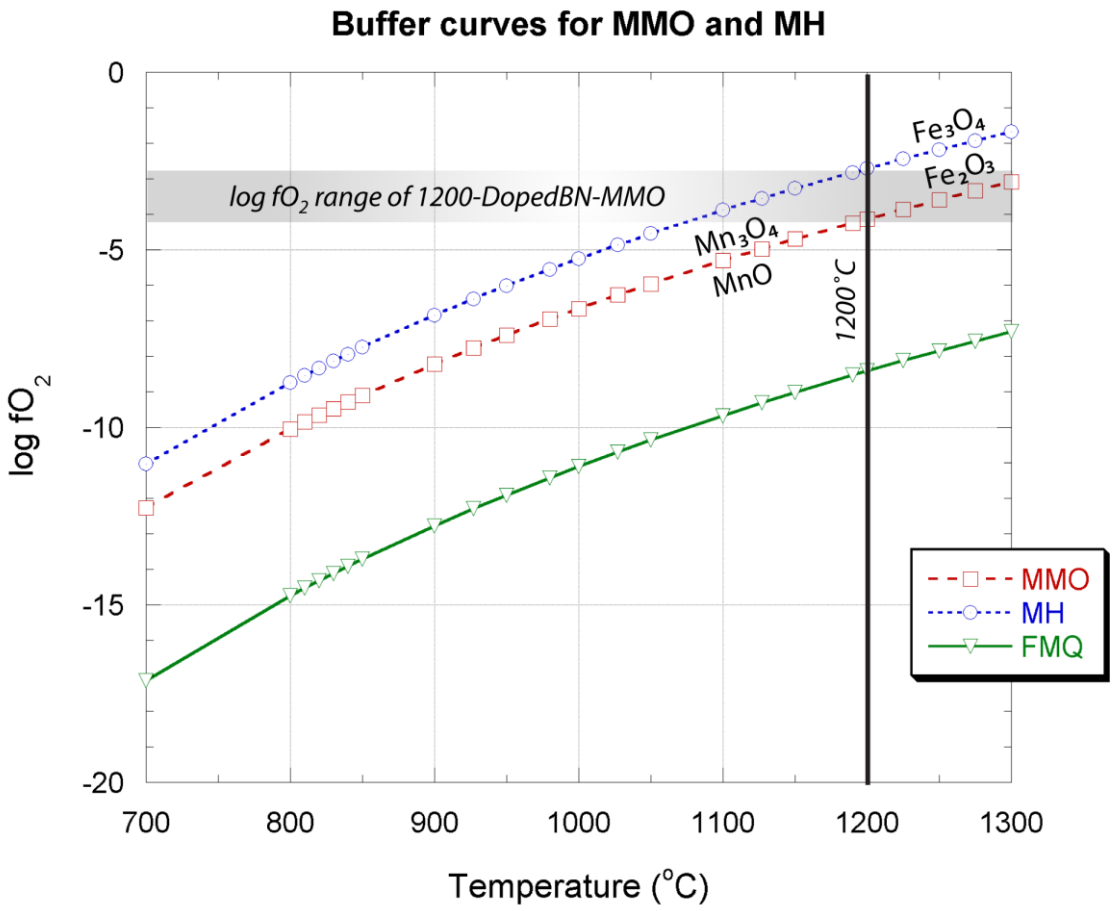

Figure 40. Plot of log fO_2 vs. T showing the log fO_2 range of sample 1200-DopedBN-MMO. MMO: MnO-Mn_3O_4 (O'Neill and Pownceby, 1993); MH: magnetite-hematite (Myers and Eugster, 1983); FMQ: fayalite-magnetite-quartz (O'Neill, 1987).

Our second attempt yielded a fairly homogenous sulfide (Figure 41), although bornite decomposed to chalcocite (Table 9). Fe, presumably from bornite, was found in minor Fe-bearing grains found above the chalcocite and around one large bubble/hole (Figure 41). Both buffering phases were present, however, allowing us to better constrain the fO_2 of the experiment (Figure 42). At the MMO buffer at 1100ºC, log fO_2 = -6.

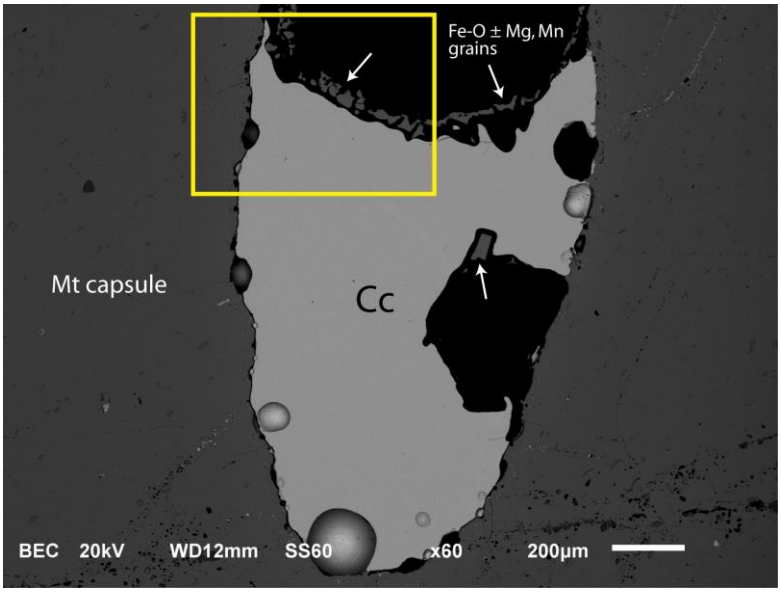

Figure 41. BSE image of 1100-Bornite-MMO. Bornite decomposed into chalcocite, and grains of an FeO ± Mg, Mn phase were found above the chalcocite and around a bubble/hole. Yellow box shows area analyzed by EDS (Appendix 2).

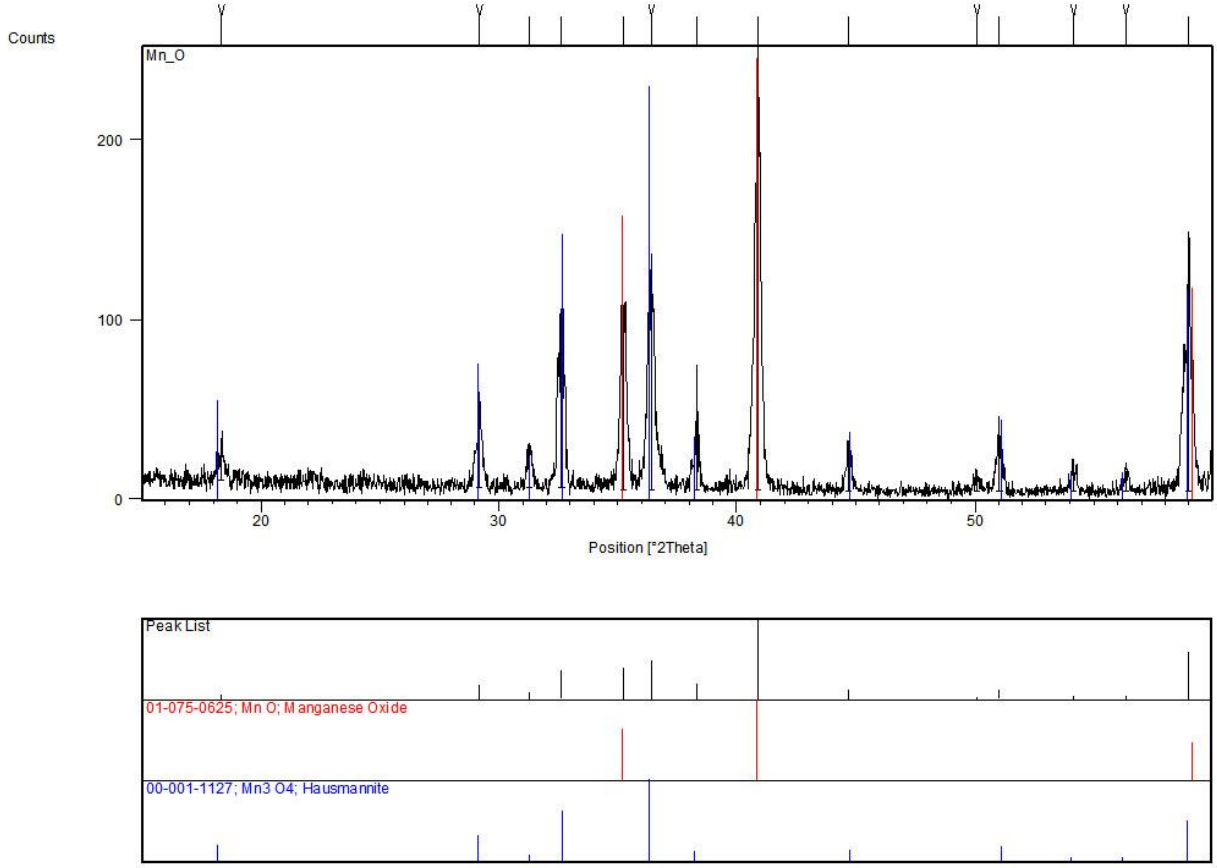

Figure 42. XRD pattern of the buffer mixture from sample 1100-Bornite-MMO. Both MnO and Mn_3O_4 were present after the experiment.

4.2.2. Cu-rich sulfides with Au and Re

Table 11 is a summary of run conditions and compositions of the buffered fusion experiments. Figures 43 and 44 show the sectioned run products to be discussed in detail later. In both our experiments with bornite (1050-cc-bn-Au and 1050-cc-bn-Re), bornite decomposed into chalcocite. We had the same result in our buffered metal-free experiment with bornite at 1100°C (1100-Bornite-MMO). Therefore our solubility measurements have been made only in chalcocite and we do not have data for bornite. We now discuss our results for our Au and Re fusion experiments with chalcocite separately.

Table 11. Summary of run conditions and compositions of the buffered fusion experiments.

Experiment ID	Temperature (°C)	Run duration (hrs)	Method of quenching	Composition (wt. %)			
				n	Cu	S	Total
1050-cc-bn-Au	1050	143.45	Air cooled	5	77.86(0.09)	22.14(0.09)	100.00
1050-cc-bn-Re	1050	116.20	Air cooled	3	78.06(0.11)	21.94(0.11)	100.00
1050-cc-Au	1050	143.45	Air cooled	3	77.79(0.12)	22.21(0.12)	100.00
1050-cc-Re	1050	143.45	Air cooled	3	78.11(0.13)	21.89(0.13)	100.00

Numbers in parentheses refer to the standard deviations of n analyses.

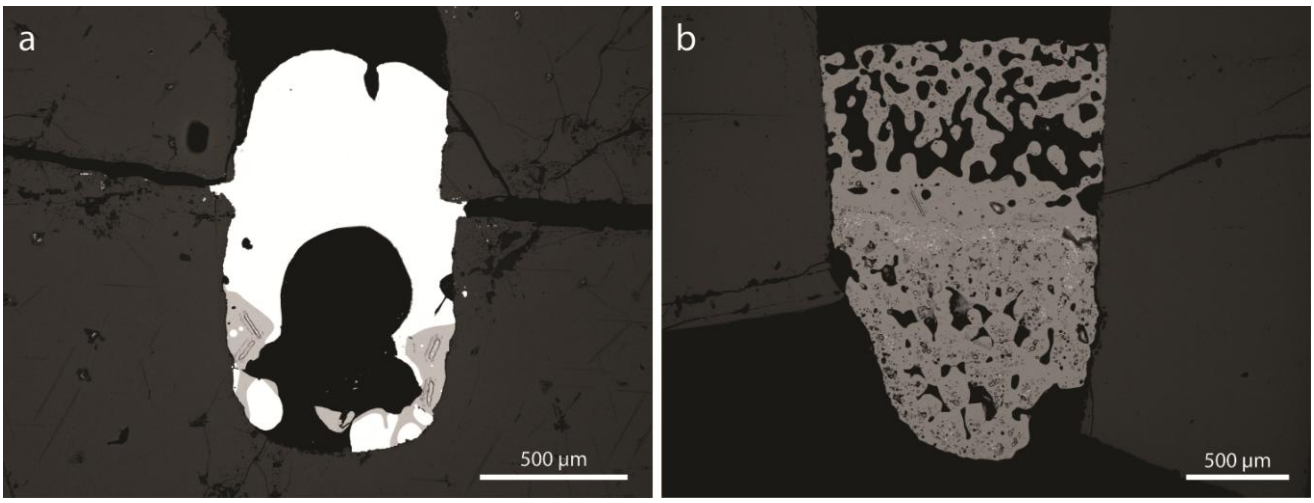

Figure 43. BSE images of (a) 1050-cc-bn-Au and (b) 1050-cc-bn-Re.

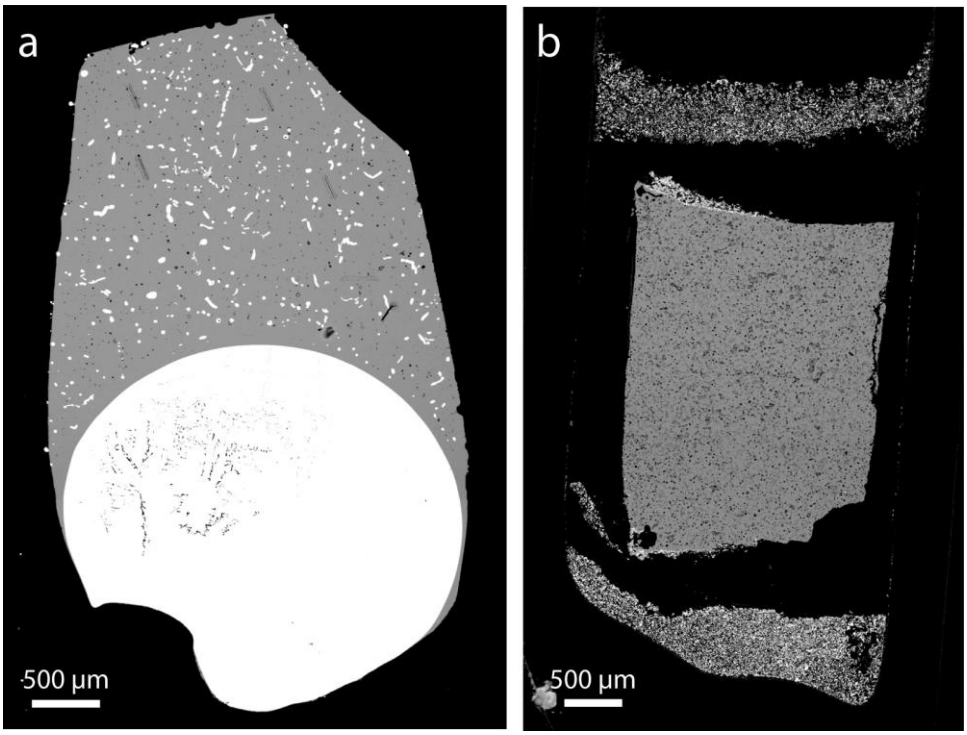

Figure 44. BSE images of (a) 1050-cc-Au and (b) 1050-cc-Re.

4.2.2.1. Au fusion experiments

The upper and lower layer of Au in both experiments (1050-cc-bn-Au and 1050-cc-Au) coalesced into fairly large blobs at the top (Figure 45) and bottom (Figure 46) of the sample. Au clearly melted, and analysis with EDS shows that Au alloyed with Cu (Appendix 3). Using EDS, mole fractions of Au (x_{Au}) were found to be 0.64 and 0.79 for 1050-cc-bn-Au and 1050-cc-Au, respectively (Table 12). Melting of Au and alloying with Cu follow from the Au-Cu phase diagram of Hultgren et al. (1973) which shows that the melting point of Au (1336.15 K or 1063°C according to this reference) is lowered in the presence of Cu. At the slightly lower run temperature of 1323.15 (1050ºC), the Au-Cu alloy is in the field of liquid.

Barely any chalcocite was left in 1050-cc-bn-Au (Figure 45), as it likely collapsed into the void shown in Figure 45a when the mount was ground. We still had enough material to analyze for Au solubility in chalcocite by LA ICP-MS. In 1050-cc-bn-Au (Figure 46), Au-Cu blebs are dispersed throughout the sample. Our interpretation of this texture is that the Au-Cu alloy filled

the bubbles or pore spaces of the solid chalcocite. Many of these bubbles or pore spaces are still found in the chalcocite, and the Re counterpart of this run (1050-cc-Re, Figure 44b) shows the extensive distribution of fine bubbles throughout the sample. Since most of the Re remained in the upper and lower layers, this is probably how the chalcocite looked like when the voids were not filled with metal.

As for the buffer mixture, both MnO and Mn_3O_4 were still present after the experiment (Figures 47 and 48), allowing us to use the MMO buffer for our later calculations involving fO_2. Since not all phases defined by the equilibrium in Reaction 2 were present after the experiment, we can only constrain the log fS_2 to be at least -0.80 as bornite is the low fS_2 phase. The consistent LA ICP-MS spectra obtained for all point analyses (Figures 49 and 50) indicated that the samples were nugget-free. Au concentrations found after data reduction were similar with one another, although 1050-cc-bn-Au had two distinct groups of data. In this case, Au concentrations were not homogenous within the sample (Spectra 1 and 2 were collected on the right side, and Spectra 3 and 4 on the left, Figure 45a). Samples contained very trace amounts of Re (often below detection limit), indicating that there was no cross-contamination within the mount (where an Au sample was mounted with a Re sample) and between analyses. Table 12 summarizes the fO_2, fS_2 and concentrations obtained for these experiments.

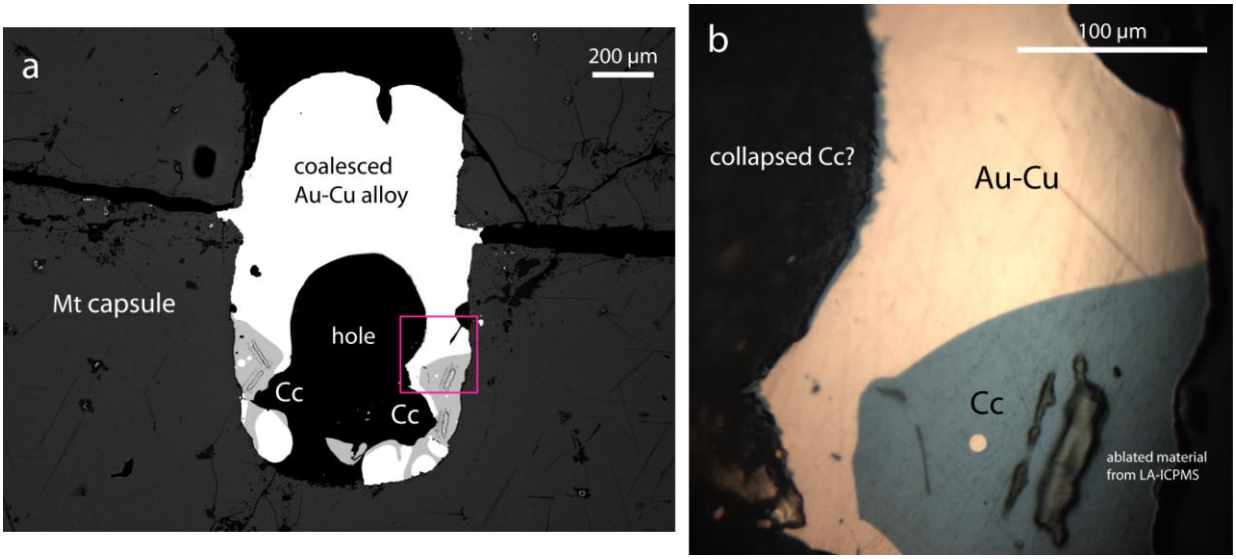

Figure 45. (a) BSE image of 1050-cc-bn-Au. The upper and lower Au layer melted and coalesced into a fairly large blob of Au-Cu alloy. Barely any chalcocite was left in the sample. The pink box shows the area shown in b. (b) Reflected light photomicrograph showing the Au-Cu alloy in contact with chalcocite. Chalcocite is also found on the fringes of the large hole in

the middle of the sample, suggesting that it collapsed when grinding the sample. Identification of the Au phase was done by EDS (Appendix 3).

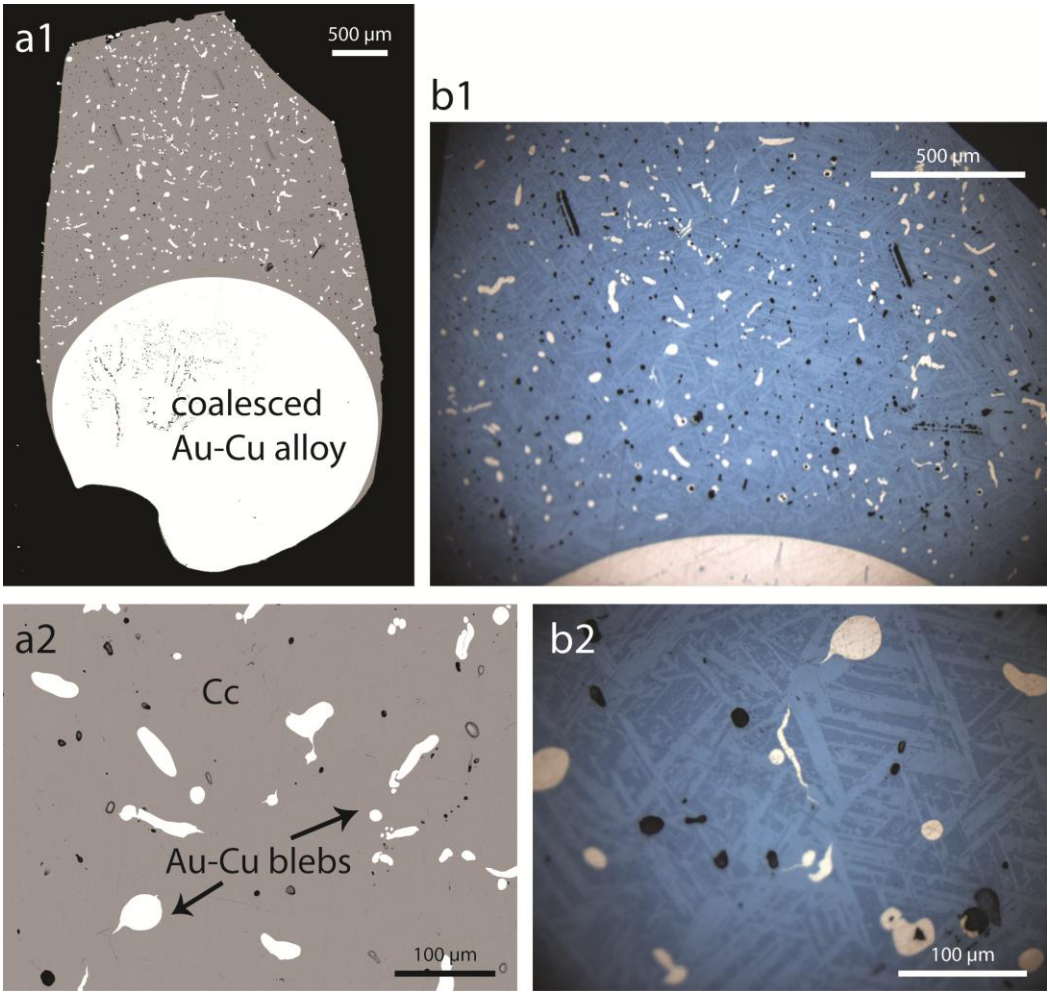

Figure 46. 1050-cc-Au. (a) BSE image of the whole sample with the coalesced Au-Cu alloy at the bottom. Au-Cu blebs are dispersed in the sulfide. (b) Reflected light photomicrograph showing strong pleochroism of the sulfide. Identification of the Au phase was done by EDS (Appendix 3).

Table 12. Summary of experimentally determined parameters for the Au fusion experiments.

Experiment ID	log fO_2	log fS_2	EDS analyses		LA ICP-MS analyses	
			n	x_{Au}^{alloy}	n	C_{Au}^{alloy} (ppm)
1050-cc-bn-Au	-6	>-0.80	5	0.64	2	37.40(1.02)
					2	63.46(1.91)
1050-cc-Au			9	0.79	5	17.71(1.25)

Numbers in parentheses refer to standard deviations of n analyses.

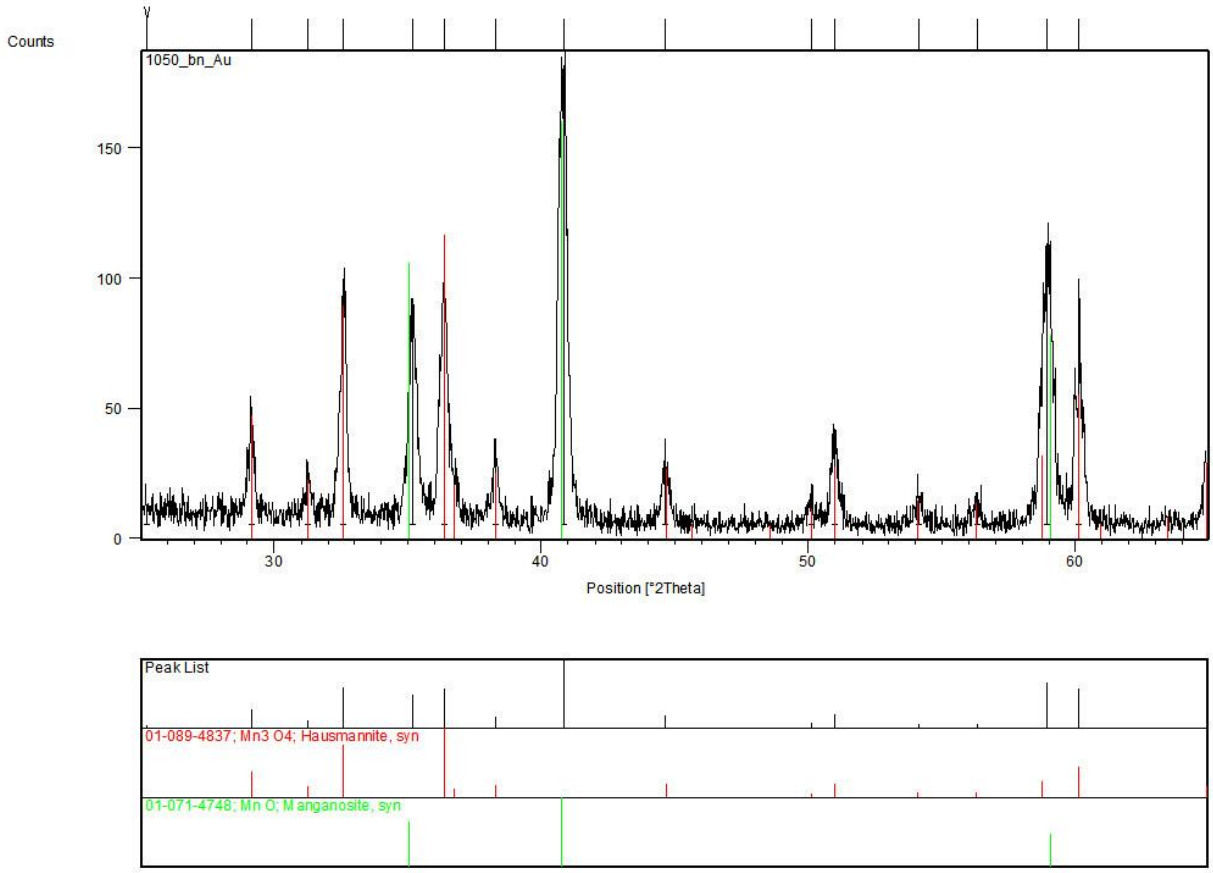

Figure 47. XRD pattern of 1050-cc-bn-Au showing the presence of both MnO and Mn_3O_4.

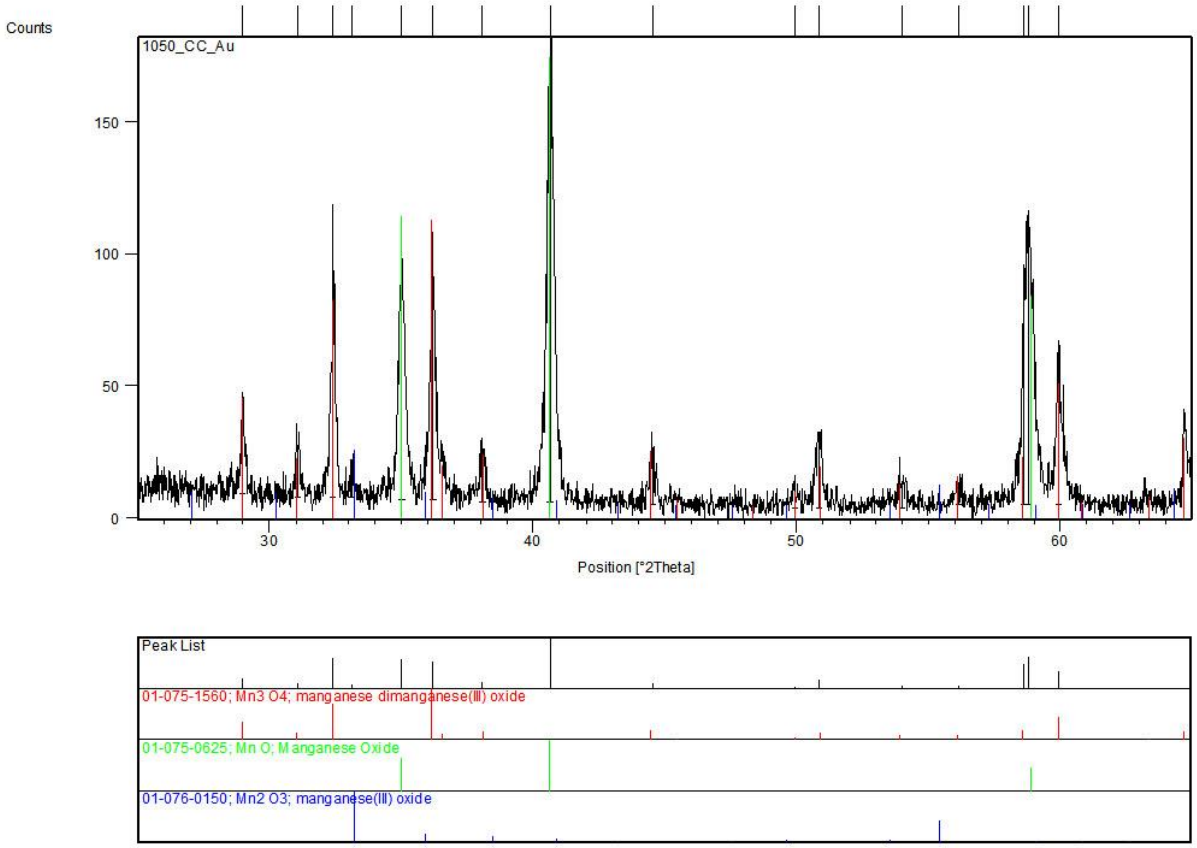

Figure 48. XRD pattern of 1050-cc-bn-Au showing the presence of both MnO and Mn_3O_4. Mn_2O_3, with an intermediate 3+ oxidation state of Mn, was also found.

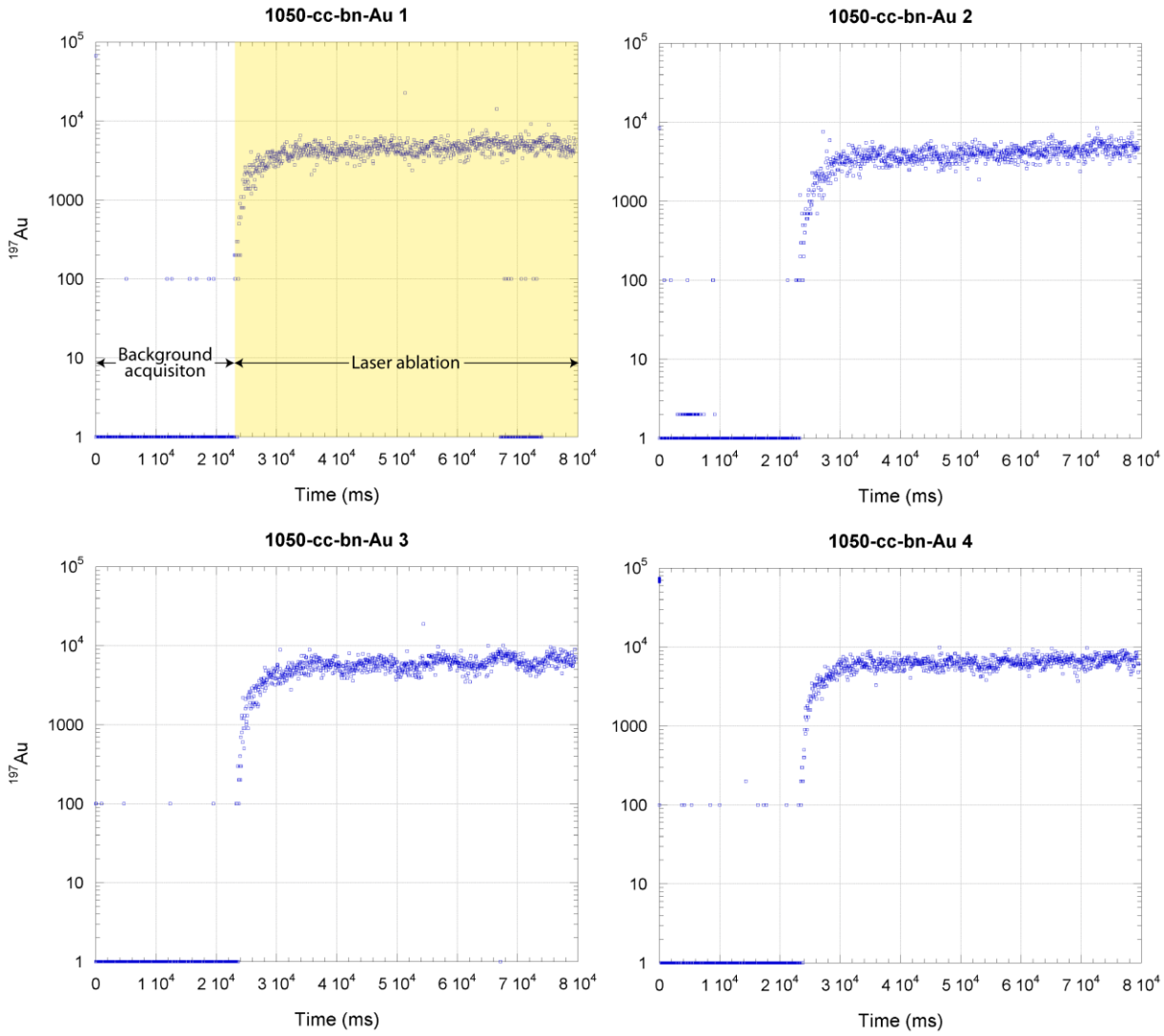

Figure 49. LA ICP-MS spectra of point analyses in 1050-cc-bn-Au. The first two and second two analyses each had similar counts, forming two distinct groups of data.

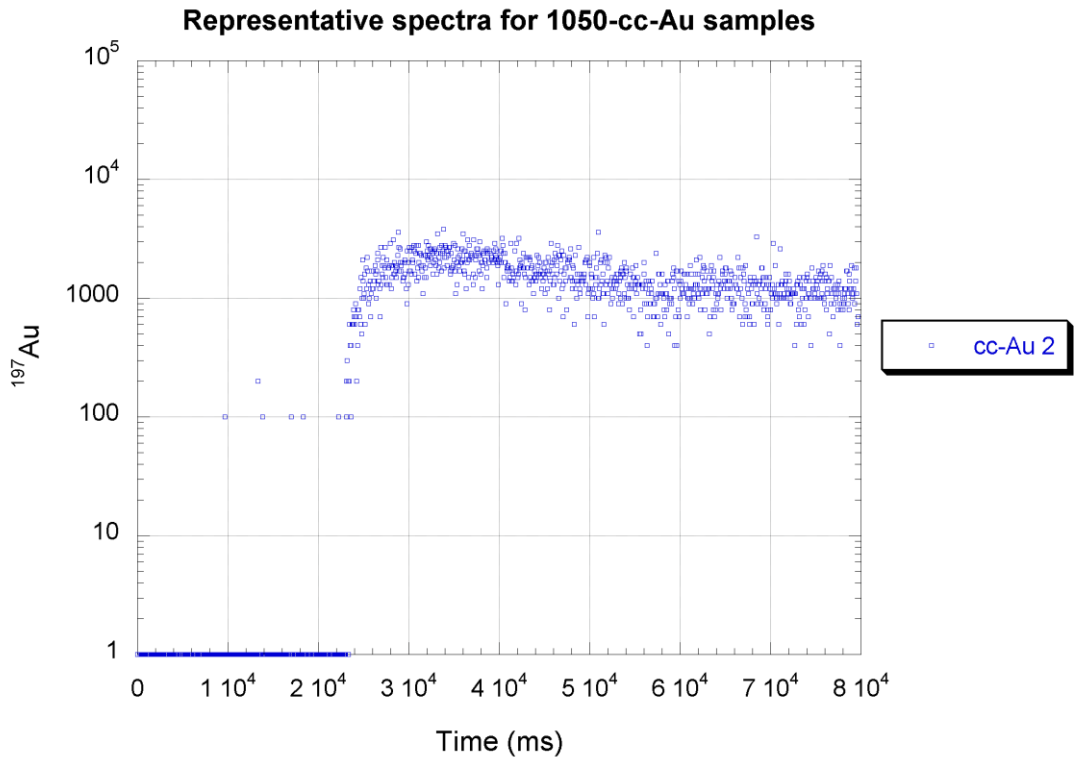

Figure 50. Representative spectra of measurements on 1050-cc-Au.

4.2.2.2. Re fusion experiments

Results for Re were much less straightforward than those for Au. The upper and lower Re layers were not present in 1050-cc-bn-Re (Figure 51), but remained in 1050-cc-Re (Figure 53). Re grains were often rimmed by another phase, either with additional O and S (1050-cc-bn-Re, Figure 52) or oxidized with O only (1050-cc-Re, Figure 54). Our later calculations do not require the mole fraction of Re in these phases, so the amount of Re present in these phases is actually not important for our purposes.

Mn_3O_4 was lost completely during the experiments (Figures 55 and 56) as the MMO buffer was above the Re-ReO_2 (RRO) buffer imposed by Re present in the samples (Figure 57). Above the RRO buffer, all Re should have oxidized to ReO_2 via the reaction:

$$Re_{metal} + O_{2(g)} = ReO_{2ox} \quad \textbf{(11)}$$

Since Mn_3O_4 was not present after the experiment, the log fO_2 range of the experiment must be below the MMO buffer (-6) but above the RRO buffer (-7.8) (Table 13). We do not report a value or range for log fS_2 since all phases in Reaction 2 are not present, and the experiments are no longer at the MMO buffer as required by our method of determining fS_2 from fO_2. LA ICP-MS spectra were also problematic, as inconsistent peaks and troughs were often observed (Figures 58 and 59). This suggests inhomogeneity or the presence of micronuggets, and so data was integrated over the lowest counts. In 1050-bn-cc-Re in particular, only one out of four analyses was used in our later calculations, as the others yielded erratic Re concentrations. Table 13 shows Re concentrations measured by LA ICP-MS. Severe contamination of Au was also noted in 1050-cc-Re where a consistent Au signal was observed even when there were inconsistent Re signals measured over the same point. We attribute this to contamination in the mount where the Au counterpart of this run (1050-cc-Au) was also placed. Grinding of the soft Au and chalcocite must have transferred Au into the Re sample. This is still puzzling, since the surfaces were pre-cleaned before analyses and Au contamination was not observed in the runs initially composed of bornite.

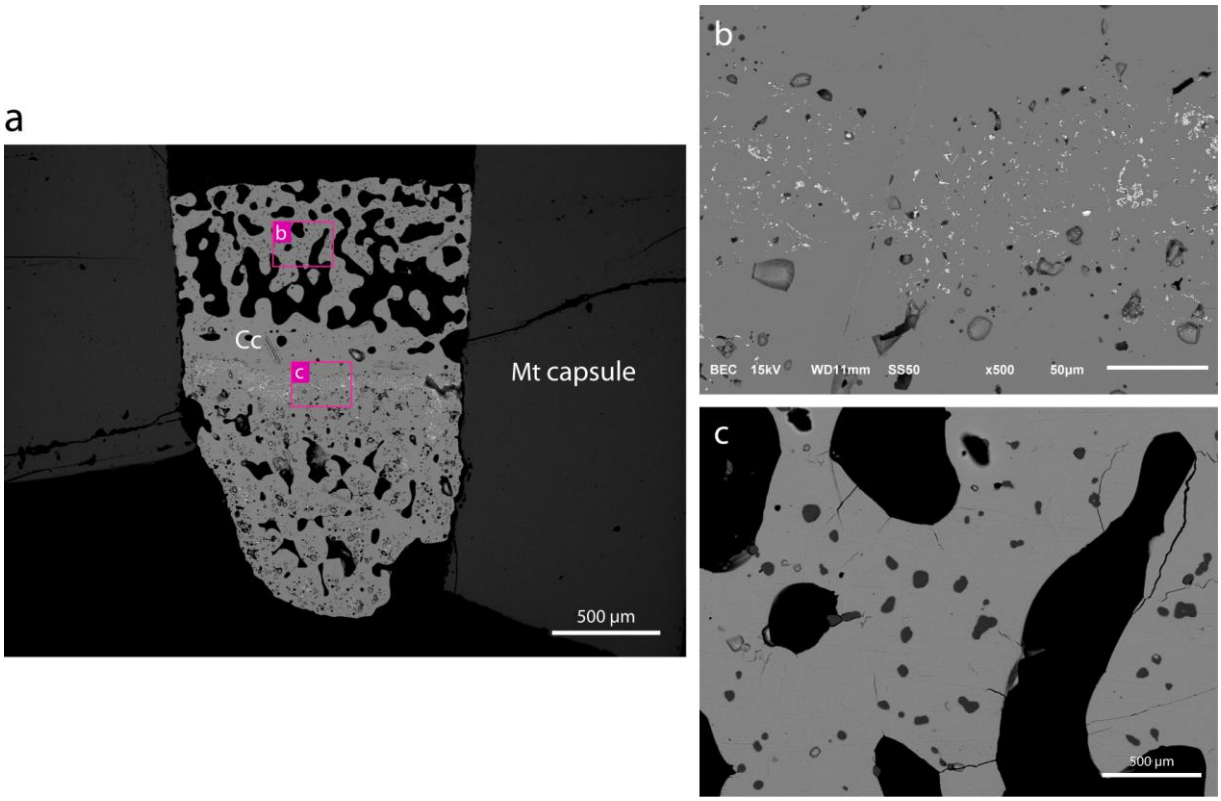

Figure 51. BSE images of 1050-cc-bn-Au. (a) Entire sample without the upper and lower Re layers present before the experiment. (b) View of region shown in (a) with a band of a bright, fine grained Re-bearing phase. (c) Grains of Fe-O-Cu (Cu-bearing magnetite?) were found in between large, elongate vesicles in the upper portion of the sample. Phase identification was done by EDS (Figure 52).

a

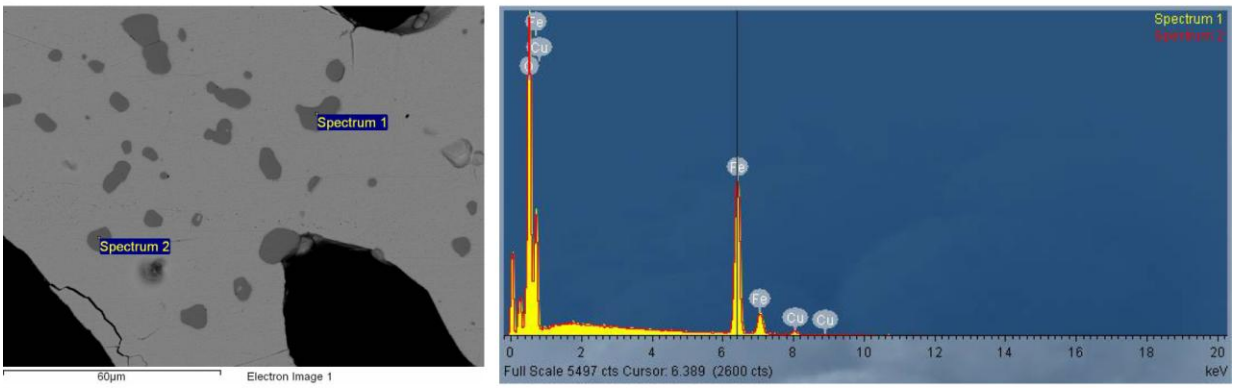

b

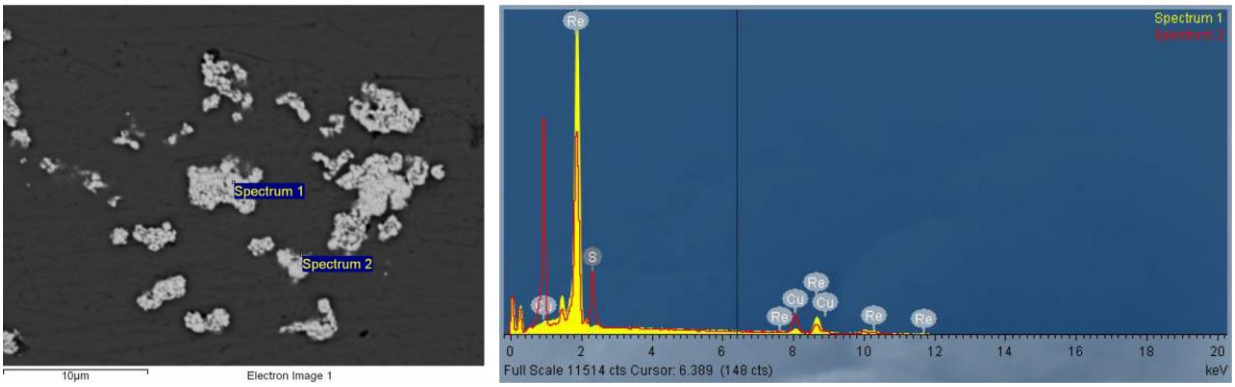

Figure 52. EDS analyses of phases in Figure 51, b and c. (a) Dark-coloured grains shown in Figure 51c are composed mainly of Fe and O (close to magnetite compositions of 1200-DopedBN-MMO, Table 10) plus minor Cu (~3 wt. %). (b) The bright, fine grains shown in Figure 51b consist mainly of Re. Bright cores are composed of Re and Cu (~5-7 wt. % only), while the darker-coloured rims contain additional S and O. Results of analyses of the rims were not very consistent with one another.

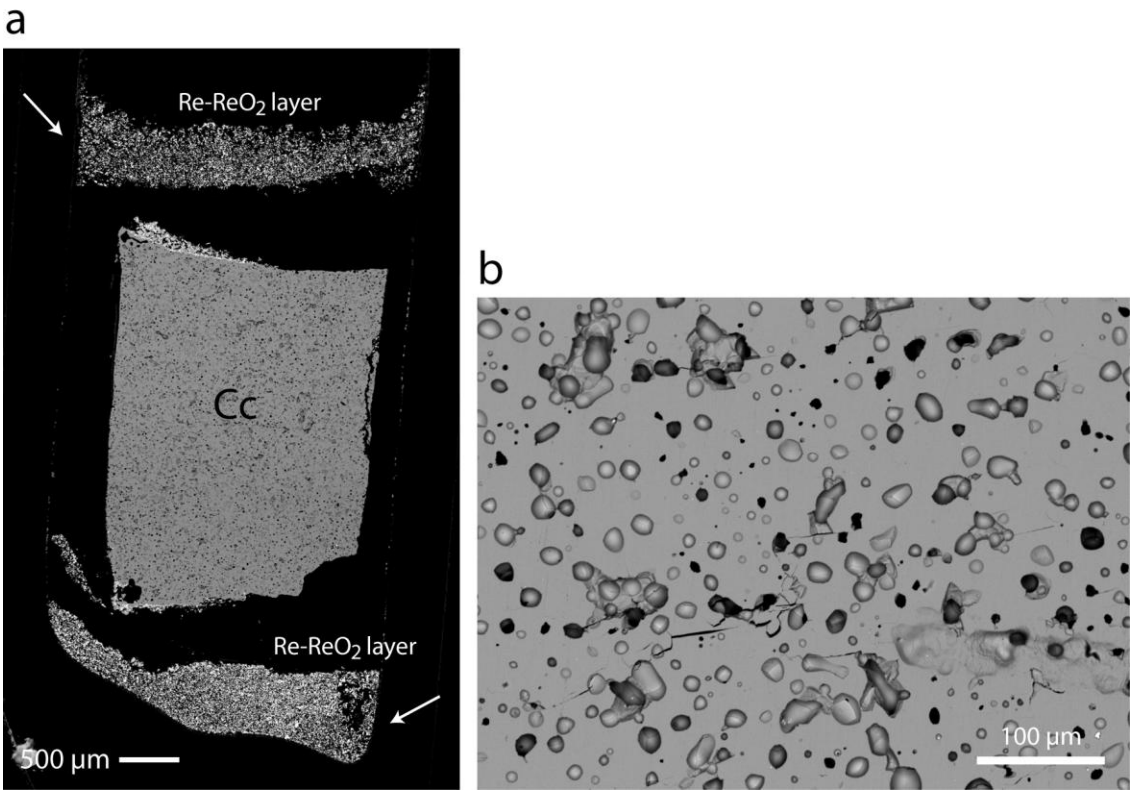

Figure 53. BSE images of 1050-cc-Re. (a) View of entire sample showing the upper and lower Re layers in the run product. (b) Extensive bubbles or pore spaces in chalcocite.

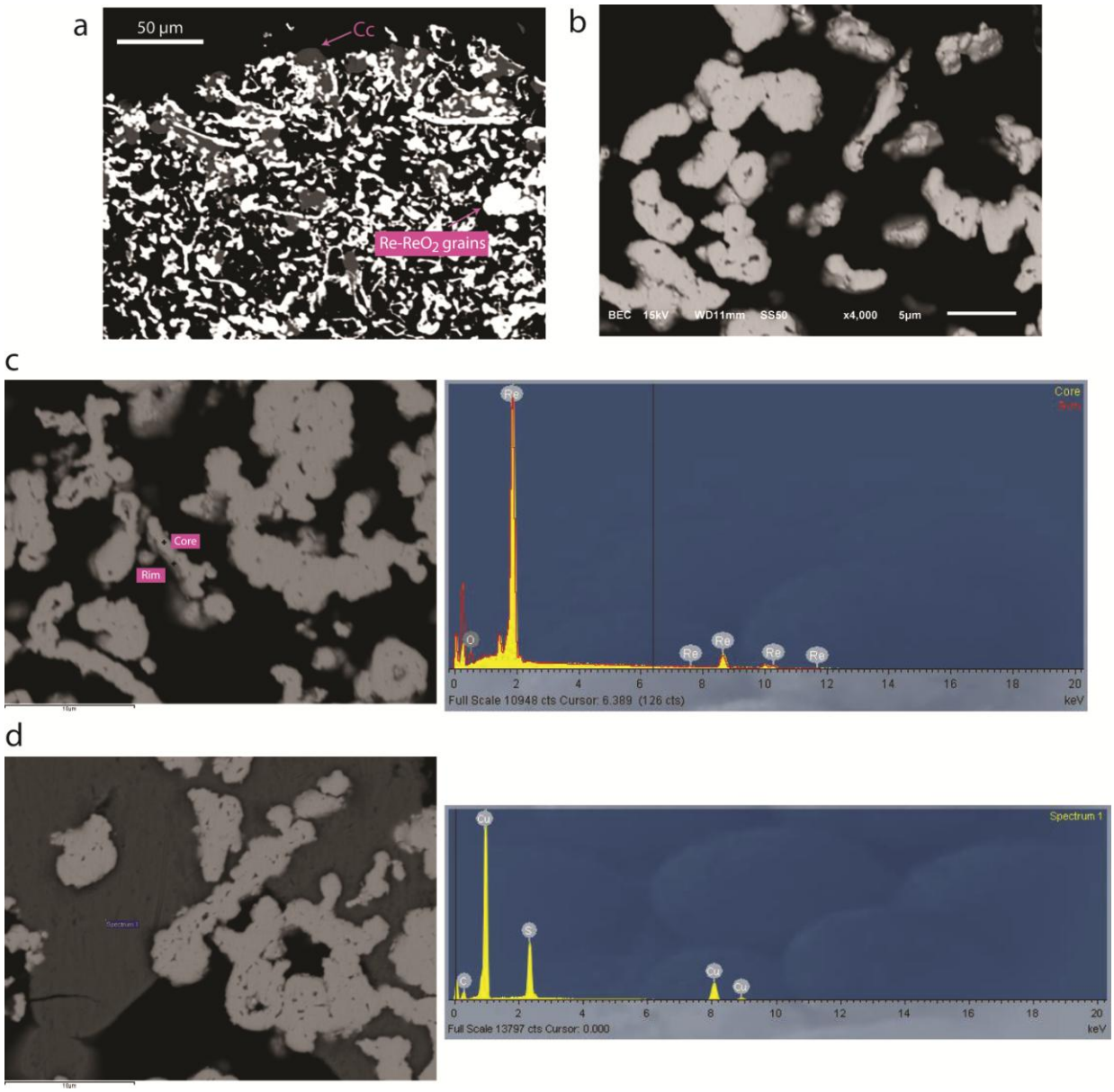

Figure 54. (a) Area in the top portion of the lower layer (closest to chalcocite) with bright Re-bearing grains together with minor chalcocite. (b) Close-up of Re-bearing grains showing their corroded appearance. There are distinct core and rim phases. (c) EDS analysis of the core and rim phases showing a core of Re with an oxidized rim (Re plus ~5 to 10 wt. % O). (d) EDS analysis of chalcocite with the Re-bearing grains.

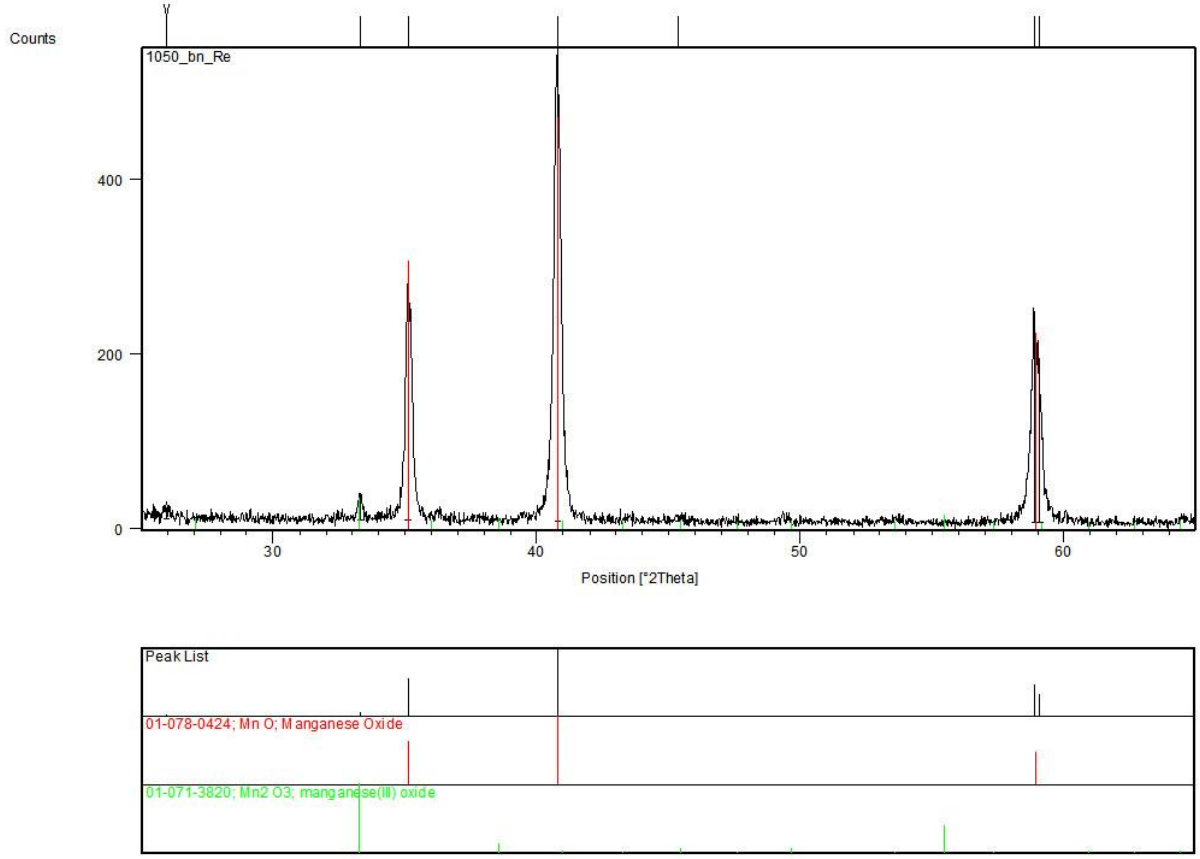

Figure 55. XRD pattern of 1050-cc-bn-Re. MnO was present, but not Mn_3O_4. Mn_2O_3, with an intermediate 3+ oxidation state of Mn, was also found.

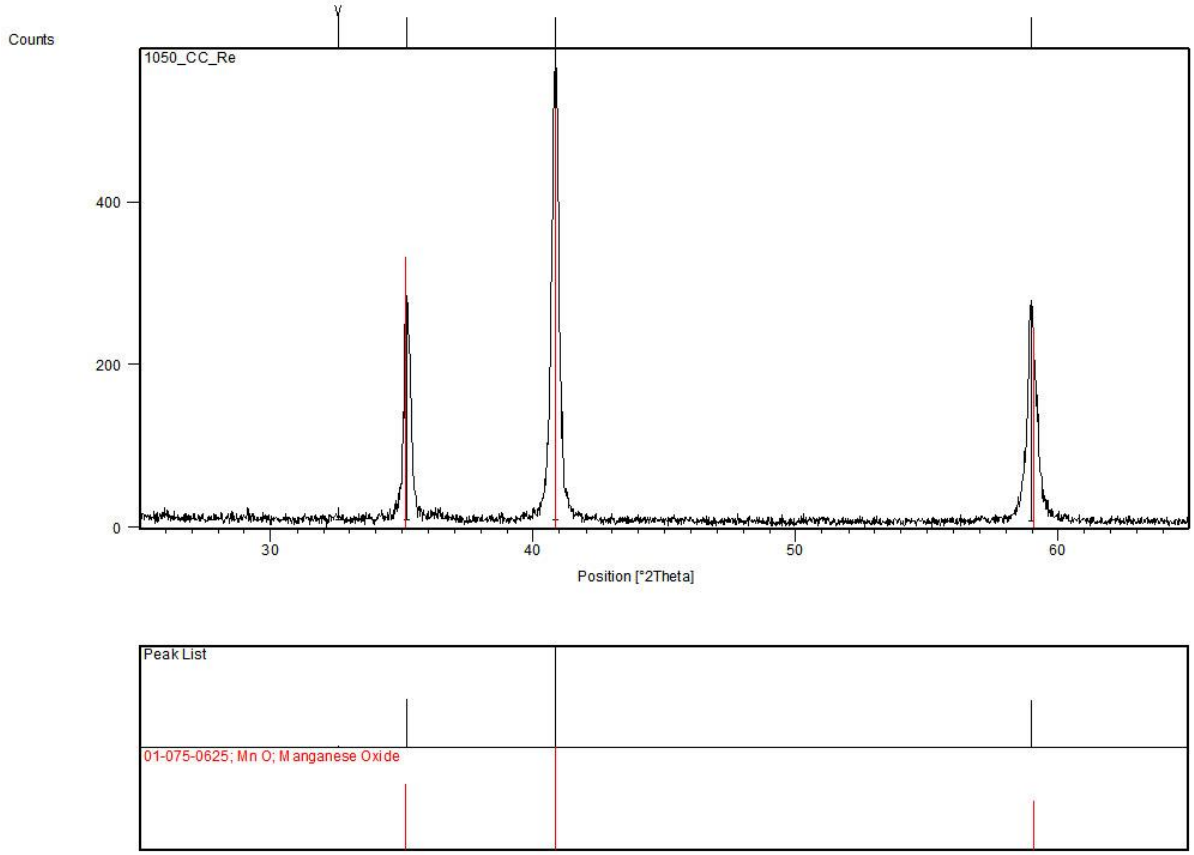

Figure 56. XRD pattern of 1050-cc-bn-Re. MnO was present, but not Mn_3O_4.

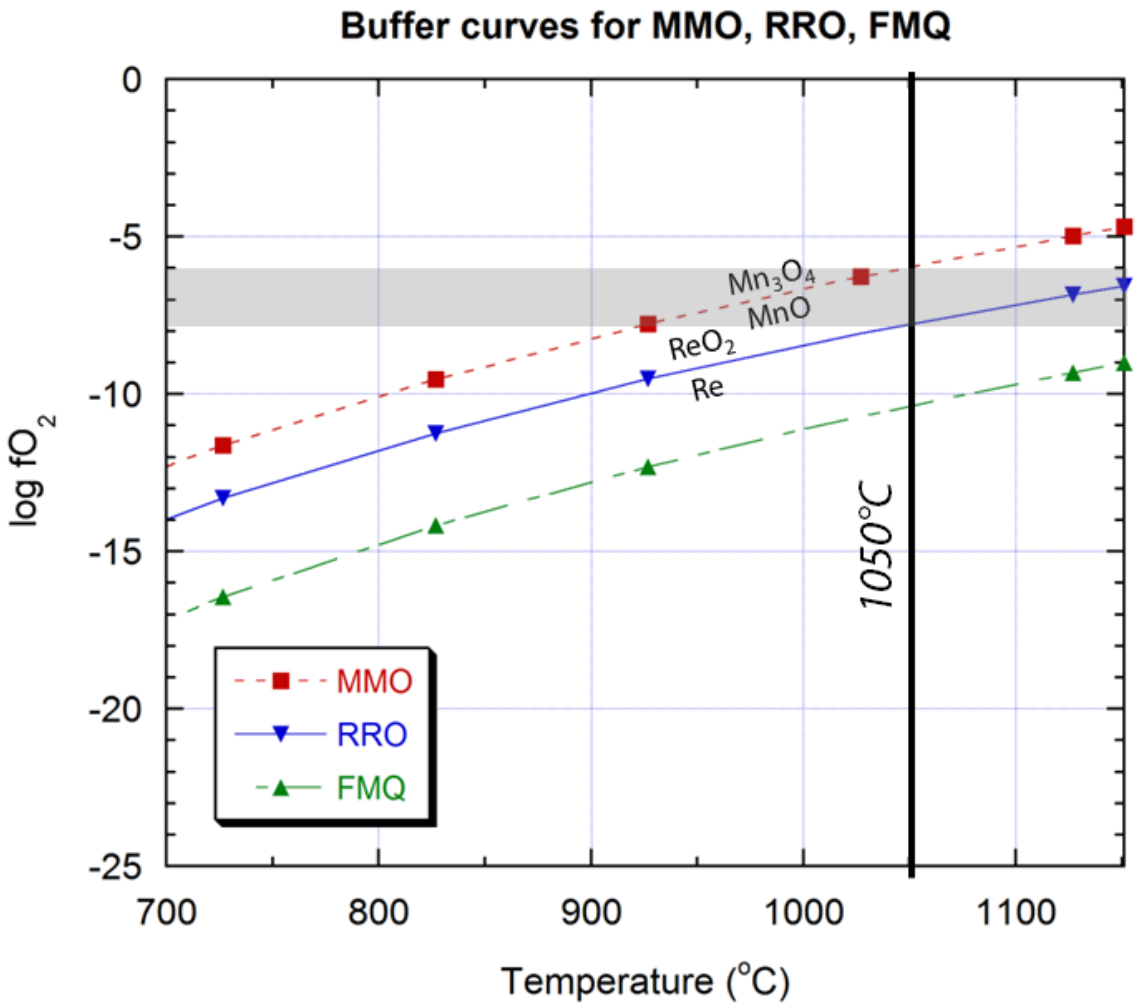

Figure 57. Plot of log fO_2 vs. T showing the log fO_2 range of the Re fusion experiments (shaded grey area). MMO: MnO-Mn_3O_4 (O'Neill and Pownceby, 1993); RRO: Re-ReO_2 (Pownceby and O'Neill, 1994); FMQ: fayalite-magnetite-quartz (O'Neill, 1987).

Table 13. Range of log fO_2 and measured Re concentrations for the Re fusion experiments.

Experiment ID	log fO_2		LA ICP-MS analyses	
	MMO	RRO	n	C_{Re} (ppm)
1050-cc-bn-Re	-6	-7.8	1	95.69(12.63)*
1050-cc-Re			4	99.41(3.60)

[a]*Number in parenthesis refers to the 1 sigma error of the analysis.*
[b]*Number in parenthesis refers to standard deviation of n analyses.*

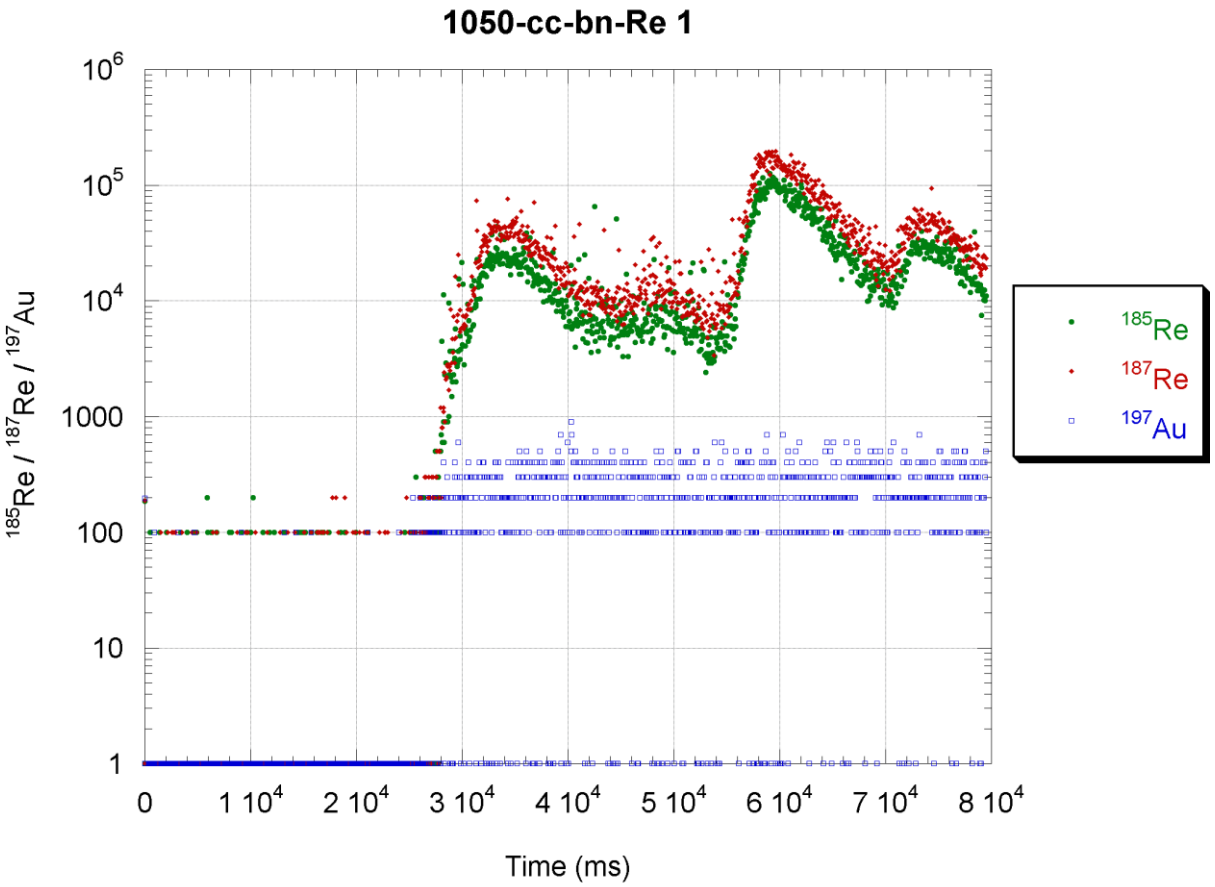

Figure 58. LA ICP-MS spectrum of one point analysis in 1050-cc-bn-Re. ^{187}Re yielded similar counts to ^{185}Re, indicating no interference with ^{187}Os. Re spectra are inconsistent with peaks and troughs, suggesting micronuggets in the sample. No contamination with Au was observed.

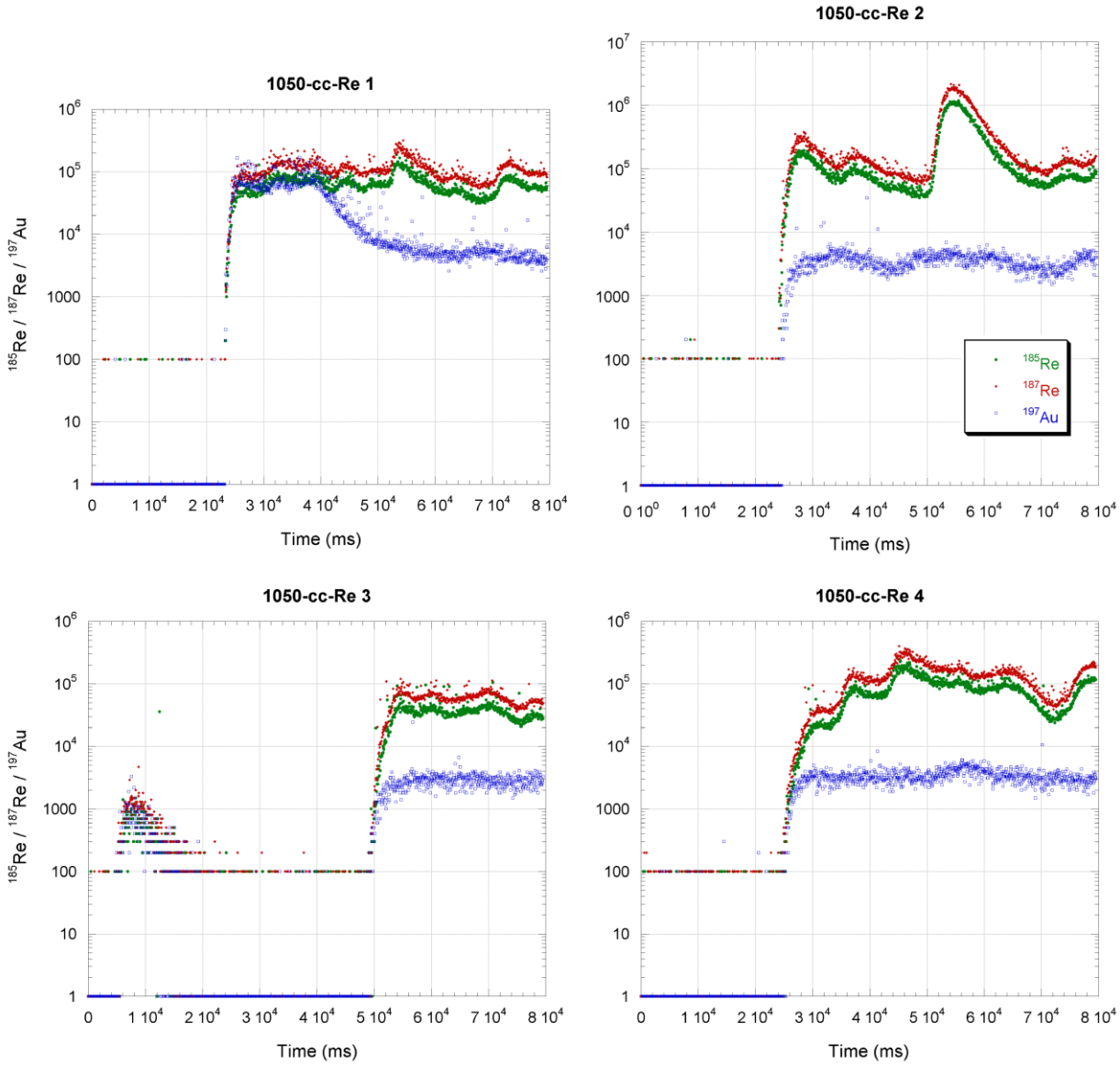

Figure 59. LA ICP-MS spectra of point analyses in 1050-cc-Re. Spectra were similar to that of 1050-cc-bn-Re (Figure 58). However, severe Au contamination was observed in all analyses, as shown by the consistent, homogenous blue spectra. There was a decrease in counts in the first part of the Au signal of 1050-cc-Re 1 as the surface in this particular analysis was not pre-cleaned.

4.3. Thermodynamic treatment of the data

Our end goal is to determine partition coefficients (D) for both Au and Re between chalcocite and silicate melt which is defined as:

$$D_{metal}^{sulfide/melt} = \frac{C_{metal}^{sulfide}}{C_{metal}^{melt}} \quad \textbf{(12)}$$

where $C_{metal}^{sulfide}$ is the concentration of the metal in chalcocite, and C_{metal}^{melt} is the concentration of the metal in silicate melt, both at saturation. Compatible metals have D >> 1, while incompatible metals have D << 1. Our hypothesis is that the partition coefficient for Au is much larger than that for Re, such that ore metal fractionation of Au in crystalline chalcocite occurs in a silicate melt. Since $C_{metal}^{sulfide}$ former requires a pure metal phase and our experimental results do not involve pure metal phases, we first discuss the activity models we have used in order to correct for the activities of the metal phases in our experiments. We then calculate $C_{metal}^{sulfide}$ for a pure metal phase from our measured concentrations, and compare the results with estimates of C_{metal}^{melt} from the literature to estimate partition coefficients.

4.3.1. Au solubility in chalcocite and silicate melt

The metal phase in the Au fusion experiments was a Au-Cu alloy as determined by EDS (Appendix 3). We constructed an activity model from the data of Hultgren et al. (1973) (Figure 60) to determine the activity of Au (a_{Au}) given measured mole fractions (x_{Au}, Table 12). Concentration of pure Au metal in chalcocite (C_{Au}^{cc}) were obtained by dividing measured concentrations obtained from LA ICP-MS (C_{Au}^{alloy}) by their respective values of a_{Au} from our activity model.

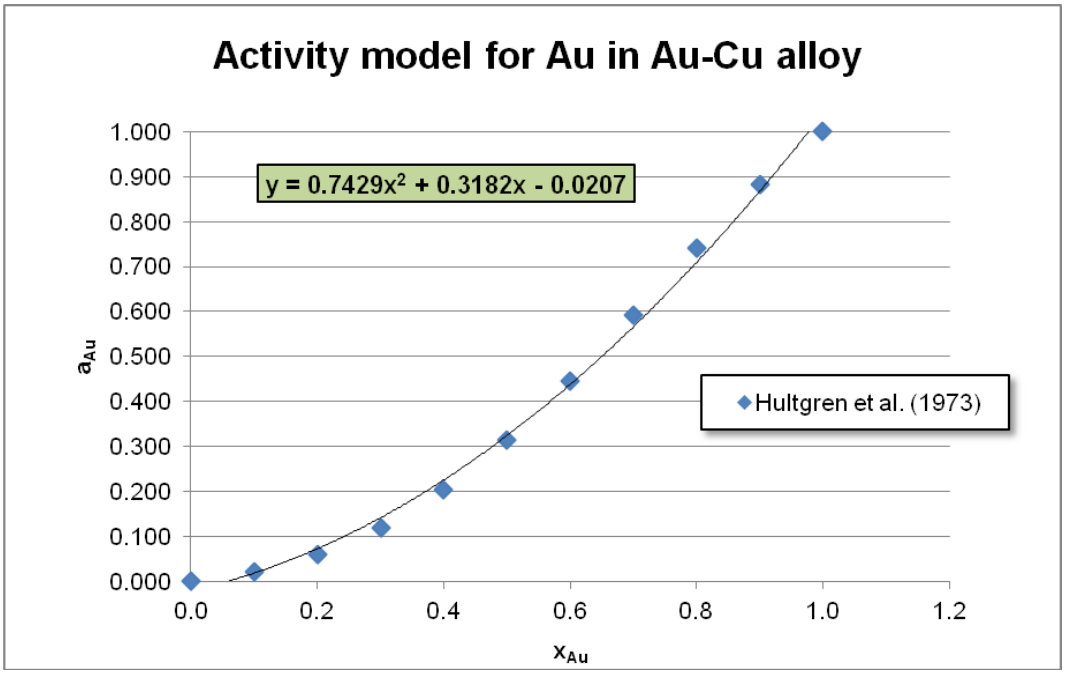

Figure 60. Activity model for Au based on thermodynamic data of Hultgren et al. (1973).

Au solubility in silicate melt (C_{Au}^{melt}) was estimated from the equation given by Borisov and Palme (1996), accounting for both fO_2 and temperature dependence of the solubility:

$$log\left(C_{Au,ppm}^{melt}\right) = 0.25 log\ fO_2 + \frac{2080}{T} + 0.59 \qquad \textbf{(13)}$$

Using the relevant variables for our experiments yields C_{Au}^{melt} = 4.6 ppm. While the experiments of Borisov and Palme (1996) were done over a wide log fO_2 range (including that of our experiments), temperatures were much higher (1300 to 1480ºC). Our value for C_{Au}^{melt} is thus an extrapolation from their data set and is used with caution in this preliminary work.

Table 14 is a summary of the results of our solubility calculations using experimental data in Table 12. $D_{Au}^{Cc/melt}$ (from Equation 13) ranges from 6 to 29. Since these values are >> 1, Au should be much more compatible in chalcocite than in the silicate melt.

4.3.2. Re solubility in chalcocite and silicate melt

Our activity model for Re uses the Re-ReO_2 equilibrium defined in Reaction 11 as all Re would have oxidized to ReO_2 below the MMO buffer. K_{eq} for this reaction can be written as:

$$K_{eq} = \frac{a^{ox}_{ReO_2}}{a_{Re}^{metal} \times fO_2} \quad \textbf{(14)}$$

Assuming $a^{ox}_{ReO_2} = 1$, ln K_{eq} is expressed as:

$$\begin{aligned} \ln K_{eq} &= -\ln a_{Re}^{metal} - \ln fO_2 \\ \ln a_{Re}^{metal} &= -\ln K_{eq} - \ln fO_2 \\ \ln a_{Re}^{metal} &= \frac{\Delta_r G^\circ}{RT} - \ln fO_2 \end{aligned} \quad \textbf{(15)}$$

Calculation of a_{Re}^{metal} requires knowledge of $\Delta_r G^\circ$ of Reaction 11. This was determined using Equation 14, assuming both $a^{ox}_{ReO_2}$ and a_{Re}^{metal} are equal to 1. ln K_{eq} is expressed only in terms of ln fO_2 and consequently, $\Delta_r G^\circ$ is dependent only on ln fO_2 and T:

$$\begin{aligned} \ln K_{eq} &= -\ln fO_2 \\ \frac{\Delta_r G^\circ}{RT} &= \ln fO_2 \\ \Delta_r G^\circ &= RT \ln fO_2 \end{aligned} \quad \textbf{(16)}$$

Values of a_{Re}^{metal} were calculated at the two bounding log fO_2's (-7.8 at RRO and -6 at MMO) using their respective values for $\Delta_r G^\circ$ (i.e., at the same log fO_2). As in our treatment of the Au data, we divided measured concentrations obtained from LA ICP-MS (C_{Re}) by a_{Re}^{metal} at the two bounding fO_2's to determine concentrations of pure Re metal in chalcocite (C_{Re}^{cc}).

We attempted to estimate the Re solubility in silicate melt from the data of Mallmann and O'Neill (2007) (Figure 61) Extrapolation of their data set to the same relative log fO_2 of FMQ + 2.6 (RRO) and FMQ + 4.4 (MMO) yields solubilities of ~90 and 41,000 wt. %, respectively. Clearly these erroneous solubilities cannot be used. Mallmann and O'Neill's (2007) data set lacks high fO_2 data relevant to our experiments (most of the data is clustered at ΔFMQ = -0.5 to -2) and does not take the effect of temperature into account. It is likely that solubilities level off at wt. % levels (10^4 ppm) at ΔFMQ > 1.5. We therefore use a conservative estimate of 1 wt. % (10,000 ppm) in our calculations for the partition coefficient.

Table 15 is a summary of the results of our solubility calculations using experimental data in Table 13 and a conservative estimate of 1 wt. % for C_{Re}^{melt}. Partition coefficients range from 0.01 to 0.63, indicating that Re would be incompatible in chalcocite and would remain in the silicate melt. An increase in C_{Re}^{melt} would only decrease $D_{Re}^{Cc/melt}$, allowing for a more dramatic fractionation of Au from Re.

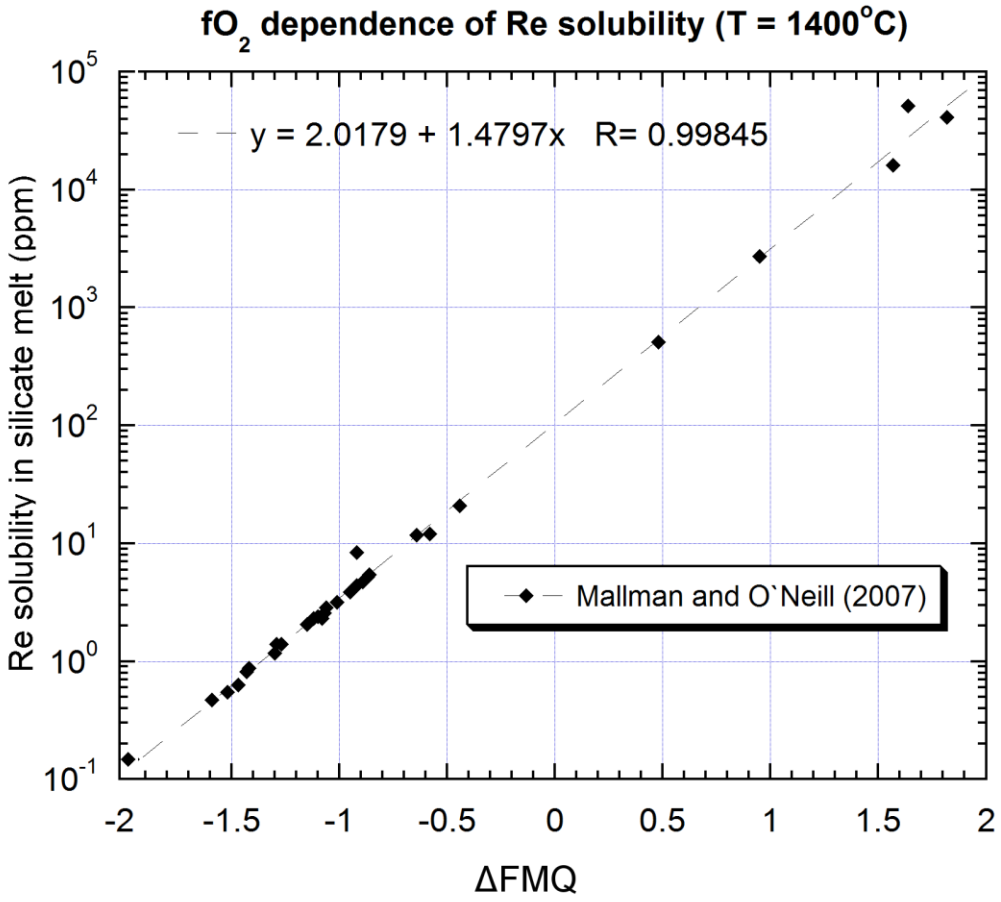

Figure 61. Plot of Re solubility vs. ΔFMQ showing the fO_2 dependence of solubility at a fixed temperature of 1400ºC. Data from Mallmann and O'Neill (2007).

Table 14. Summary of results of Au solubility calculations.

Experiment ID	log fO_2	log fS_2	EDS analyses		a_{Au} in alloy	LA ICP-MS analyses		Corrected C_{Au}^{Cc} (ppm)	C_{Au}^{melt} (ppm)	$D_{Au}^{Cc/melt}$
			n	x_{Au}^{alloy}		n	C_{Au}^{alloy} (ppm)			
1050-cc-bn-Au	-6	>-0.80	5	0.64	0.48	2	37.40(1.02)	77	4.6	17
						2	63.46(1.91)	131		29
1050-cc-Au			9	0.79	0.69	5	17.71(1.25)	26		6

Table 15. Summary of results of Re solubility calculations.

Experiment ID	log fO_2		a_{Re}		LA ICP-MS analyses		Corrected C_{Re}^{Cc} (ppm)		C_{Re}^{melt} (ppm, conservative estimate)	$D_{Re}^{Cc/melt}$	
	MMO	RRO	MMO	RRO	n	C_{Re} (ppm)	MMO	RRO		MMO	RRO
1050-cc-bn-Re	-6	-7.8	0.02	1	1	95.69(12.63)	6,037	95.69	10,000	0.60	0.01
1050-cc-Re					4	99.41(3.60)	6,273	99.41		0.63	0.01

5. Conclusions and future work

We have preliminary experimental evidence for the fractionation of Au from Re in crystalline chalcocite in a silicate melt at oxidizing conditions relevant to arc magmas. Experiments were performed with Re to demonstrate parallel behavior in PGEs. Our estimates for $D_{Au}^{Cc/melt}$ and $D_{Re}^{Cc/melt}$ range from 6 to 29 and 0.01 to 0.63, respectively, at FMQ + 2.6 to 4.4 at 1050°C. These estimates were obtained by experimentally determining the solubilities of Au and Re in chalcocite and compared these to their respective solubilities in the silicate melt from the literature. We initially had two sets of evacuated silica tube fusion experiments that consisted of a Cu-rich sulfide (bornite or chalcocite) doped with either Au or Re. In the runs that initially had bornite as the Cu-rich sulfide, bornite decomposed into chalcocite, and so our results pertain to only chalcocite.

Control of fO_2 was achieved using the $MnO\text{-}Mn_3O_4$ oxygen buffer (MMO, FMQ + 4.4). We anticipated controlling the fS_2 by only controlling the fO_2 using an equilibrium involving bornite, oxygen, magnetite, chalcocite and sulfur (Reaction 2). Not all phases were present in our experiments, so the fS_2 was not well constrained. Experiments with Au were still at the MMO buffer, while those with Re were between the MMO and Re-ReO_2 buffer (RRO, FMQ + 2.6). We performed our experiments at 1050°C, the maximum thermal stability of crystalline chalcocite as determined by phase equilibrium and centrifuge experiments that used the same evacuated silica tube technique. The latter was much more effective in demonstrating liquid and solid textures at run conditions.

Our results and subsequent treatment of the data were more straightforward for Au for various reasons: the composition of the Au-Cu alloy phase was well constrained; data was available to construct an activity model for Au; LA ICP-MS spectra for Au in chalcocite were consistent and homogenous; and the solubility in silicate melt is well known at high fO_2. In contrast, data for Re were problematic: Re grains in the run products were difficult to characterize compositionally; LA ICP-MS spectra for Re in chalcocite were inconsistent indicating inhomogeneity; and the solubility in silicate melt is not well constrained at high fO_2. In order to

still get an estimate for Re partition coefficients, we devised a Re activity model that did not require measured X_{Re} in the Re grains, selected regions in the spectra with the lowest counts, and used a conservative estimate for the solubility. We used Au and Re solubilities in a silicate melt of basaltic composition and assumed that there was no dependence on melt composition. Arc magmas are typically intermediate to felsic in composition and this was not accounted for in our estimates for partition coefficients. At least for Au, however, silicate melt composition only has a minor effect on the solubility, compared to other intensive parameters such as redox conditions, temperature, and the activity of volatiles (Botcharnikov et al., 2010; Jégo et al., 2010).

Considerably more time and effort was spent in the phase equilibrium and centrifuge experiments that we lacked time to do the actual partitioning experiments that we intended. Nonetheless, we had significant results from our preliminary fusion experiments. The set-up of future partitioning experiments will consist of a solid buffer, felsic melt, bornite and chalcocite, and the metal of interest. The fS_2 at which bornite and chalcocite will both be stable would have to be controlled by the solid sulfur buffer (e.g., Ru-RuS_2, Pt-PtS). A low viscosity melt needs to be used to enhance diffusion of metals into the melt and into the sulfides. Although felsic melts are typically highly viscous owing to SiO_2 network formers, peralkaline compositions are relatively less viscous than metaluminous compositions with the same SiO_2 content (Dingwell et al., 1998). The effect of S on metal solubility in the melt will also be investigated with the addition of melt into the experimental set-up. For example, S-bearing magmas dissolve more Au compared with S-free magmas, but the difference decreases with increasing fO_2 (Jégo and Pichavant, 2012). Complexation of Au with S in the melt is likely, thereby increasing the solubility in the melt and lowering its partition coefficient. Finally, PGEs should be investigated with Au and perhaps Ag, as what was originally intended in this work.

Acknowledgements

I am grateful for the guidance of my mentor and supervisor, Professor James Brenan, not only during all stages of this thesis project, but also during the last two years of my involvement with the High Pressure Laboratory. Beginning with my summer NSERC research assistantship after my second year, I have learned a great deal about the world of experimental petrology under his wing.

I would also like to thank the graduate students and staff in the lab, Yanan Liu, Neil Bennett, Duane Smythe and Boris Foursenko, who never hesitated to help me with any aspect of my work. This included putting out some fires I have caused, both figuratively and literally. Lastly, George Kretschmann is thanked for providing invaluable support with SEM and XRD analyses.

References

Barin, I., Ed. (1995) Thermochemical data of pure substances, 3rd ed. VCH, New York.

Barton, P.B. (1973) Solid solutions in system Cu-Fe-S. Part I: The Cu-S and CuFe-S joins. Economic Geology, 68, 455-465.

Borisov, A. and Palme, H. (1996) Experimental determination of the solubility of Au in silicate melts. Mineralogy and Petrology, 56, 297-312.

Botcharnikov, R.E., Linnen, R.L. and Holtz, F. (2010) Solubility of Au in Cl- and S-bearing hydrous silicate melts. Geochimica et Cosmochimica Acta, 74, 2396-2411.

Brenan, J.M., Haider, N. and Andrew, D. (2008) Experimental evaluation of liquid immiscibility in a portion of the system Fe-Ni-S using high gravitational acceleration. Economic Geology, 103, 1563-1570.

Cabri, L.J. (1973) New data on phase relations in the Cu-Fe-S system. Economic Geology, 68, 443-454.

Cook, N.J., Ciobanu, C.L., Danyushevsky, L.V. and Gilbert, S. (2011) Minor and trace elements in bornite and associated Cu-(Fe)-sulfides: A LA-ICP-MS study. Geochimica et Cosmochimica Acta, 75, 6473-6496.

Craig, J.R. and Scott, S.D. (1974). Sulfide phase equilibria. In P.H. Ribbe, Ed., Sulfide Mineralogy, 1, p. CS-1-110. Reviews in Mineralogy, Mineralogical Society of America, Washington DC.

Dingwell, D.B., Hess, K.U. and Romano, C. (1998) Extremely fluid behavior of hydrous peralkaline rhyolites. Earth and Planetary Science Letters, 158, 31-38.

Hattori, K. (1996) Occurrence and origin of sulfide and sulfate in the 1991 Mount Pinatubo eruption products. http://pubs.usgs.gov/pinatubo/hattori/

Hedenquist, J.W. and Lowenstern, J.B. (1994) The role of magmas in the formation of hydrothermal ore deposits. Nature, 370, 519-527.

Hultgren, R., Desai, P.D., Hawkins, D.T., Gleiser, M. and Kelley, K.K. (1973) Selected values of the thermodynamic properties of binary alloys. American Society of Metals, Metals Park.

Jego, S., Pichavant, M. and Mavrogenes, J.A. (2010) Controls on gold solubility in arc magmas: An experimental study at 1000°C and 4 kbar. Geochimica et Cosmochimica Acta, 74, 2165-2189.

Jégo, S. and Pichavant, M. (2012) Gold solubility in arc magmas: Experimental determination of the effect of sulfur at 1000°C and 0.4 GPa. Geochimica et Cosmochimica Acta, 84, 560-592.

Jugo, P.J., Candela, P.A. and Piccoli, P.M. (1999) Magmatic sulfides and Au:Cu ratios in porphyry deposits: An experimental study of copper and gold partitioning at 850°C, 100 MPa in a haplogranitic melt-pyrrhotite-intermediate solid solution-gold metal assemblage, at gas saturation. Lithos, 46, 573-589.

Klein C. and Dutrow B. (2008). The 23rd Edition of the Manual of Mineral Science (after James D. Dana). J. Wiley and Sons, Inc., Hoboken.

Kullerud, G., Yund, R.A. and Moh, G.H. (1969) Phase relations in the Cu-Fe-S, Cu-Ni-S and Fe-Ni-S systems. In H.D.B. Wilson, Ed., Magmatic ore deposits: A symposium, p. 323-343. The Economic Geology Publishing Company, Lancaster.

Lynton, S.J., Candela, P.A. and Piccoli, P.M. (1993) An experimental study of the partitioning of copper between pyrrhotite and a high silica rhyolitic melt. Economic Geology, 88, 901-915.

Mallmann, G. and O'Neill, H.S.C. (2007) The effect of oxygen fugacity on the partitioning of Re between crystals and silicate melt during mantle melting. Geochimica et Cosmochimica Acta, 71, 2837-2857.

Mungall, J.E. (2002) Roasting the mantle: Slab melting and the genesis of major Au and Au-rich Cu deposits. Geology, 30, 915-918.

Myers, J. and Eugster, H.P. (1983) The system Fe-Si-O: Oxygen buffer calibrations to 1,500K. Contributions to Mineralogy and Petrology, 82, 75-90.

O'Neill, H.S.C. (1987) Quartz-fayalite-iron and quartz-fayalite-magnetite equilibria and the free-energy of formation of fayalite (Fe_2SiO_4) and magnetite (Fe_3O_4). American Mineralogist, 72, 67-75.

O'Neill, H.S.C. and Pownceby, M.I. (1993) Thermodynamic data from redox reactions at high temperatures. II. The MnO-Mn_3O_4 oxygen buffer, and implications for the thermodynamic properties of MnO and Mn_3O_4. Contributions to Mineralogy and Petrology, 114, 315-320.

Pownceby, M.I. and O'Neill, H.S.C. (1994) Thermodynamic data from redox reactions at high temperatures. IV. Calibration of the Re-ReO_2 oxygen buffer from EMF and NiO + Ni-Pd redox sensor measurements. Contributions to Mineralogy and Petrology, 118, 130-137.

Robie, R.A., Seal, R.R. and Hemingway, B.S. (1994) Heat capacity and entropy of bornite (Cu_5FeS_4) between 6 and 760 K and the thermodynamic properties of phases in the system Cu-Fe-S. Canadian Mineralogist, 32, 945-956.

Sillitoe, R.H. (2010) Porphyry copper systems. Economic Geology, 105, 3-41.

Simon, G., Kesler, S.E., Essene, E.J. and Chryssoulis, S.L. (2000) Gold in porphyry copper deposits: Experimental determination of the distribution of gold in the Cu-Fe-S system at 400 to 700°C. Economic Geology and the Bulletin of the Society of Economic Geologists, 95, 259-270.

Weast, R.C., Ed. (1979) CRC handbook of chemistry and physics, 60^{th} ed. Chemical Rubber Company Press, Cleaveland.

Yund, R.A. and Kullerud, G. (1966). Thermal stability of assemblages in the Cu-Fe-S system. Journal of Petrology, 7, 454-488.

Appendix 1. Detailed textures in centrifuge experiments

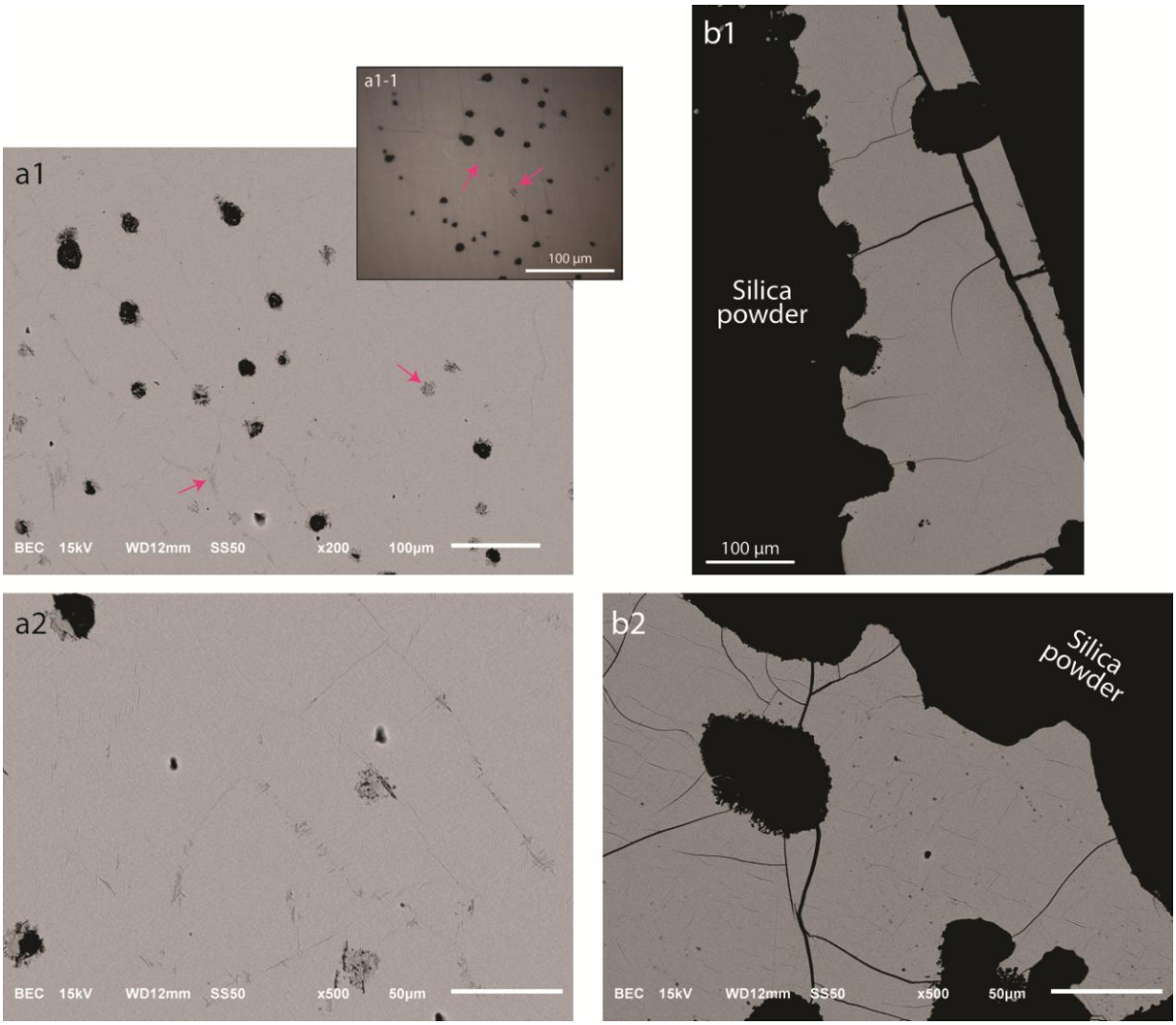

Figure A1. BSE images of (a) Cent1200bn-1 (static run) and (b) Cent1200bn-2 (centrifuged run) showing detailed textures of the run products. (a) Faint dark-coloured lines that mimic grain boundaries are observed. Also found are fine aggregate bodies of similar colour (shown by pink arrows in a1 and a1-1). (b1) The faint lines are less abundant at the top of the sample (right side is shown here) and more abundant at the bottom of the sample (b2).

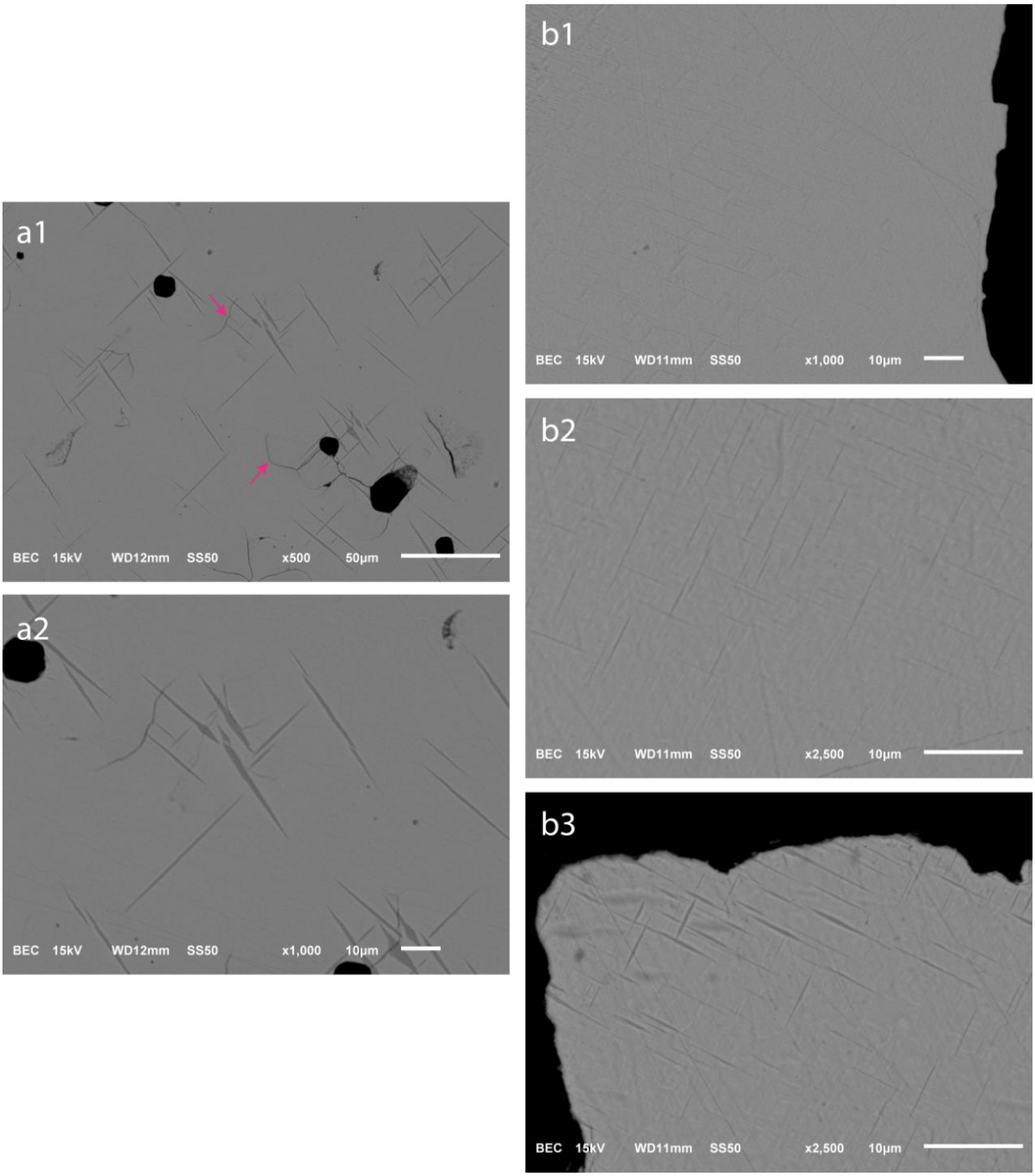

Figure A2. BSE images of (a) Cent1100bn-1a (static run) and (b) Cent1100bn-2 (centrifuged run) showing detailed textures of the run products. In both samples, it is clear that there is a second phase that has been quenched or exsolved from the main phase. a1 and a2 are in the same field of view, while b1, b2 and b3 are from different areas in the sample.

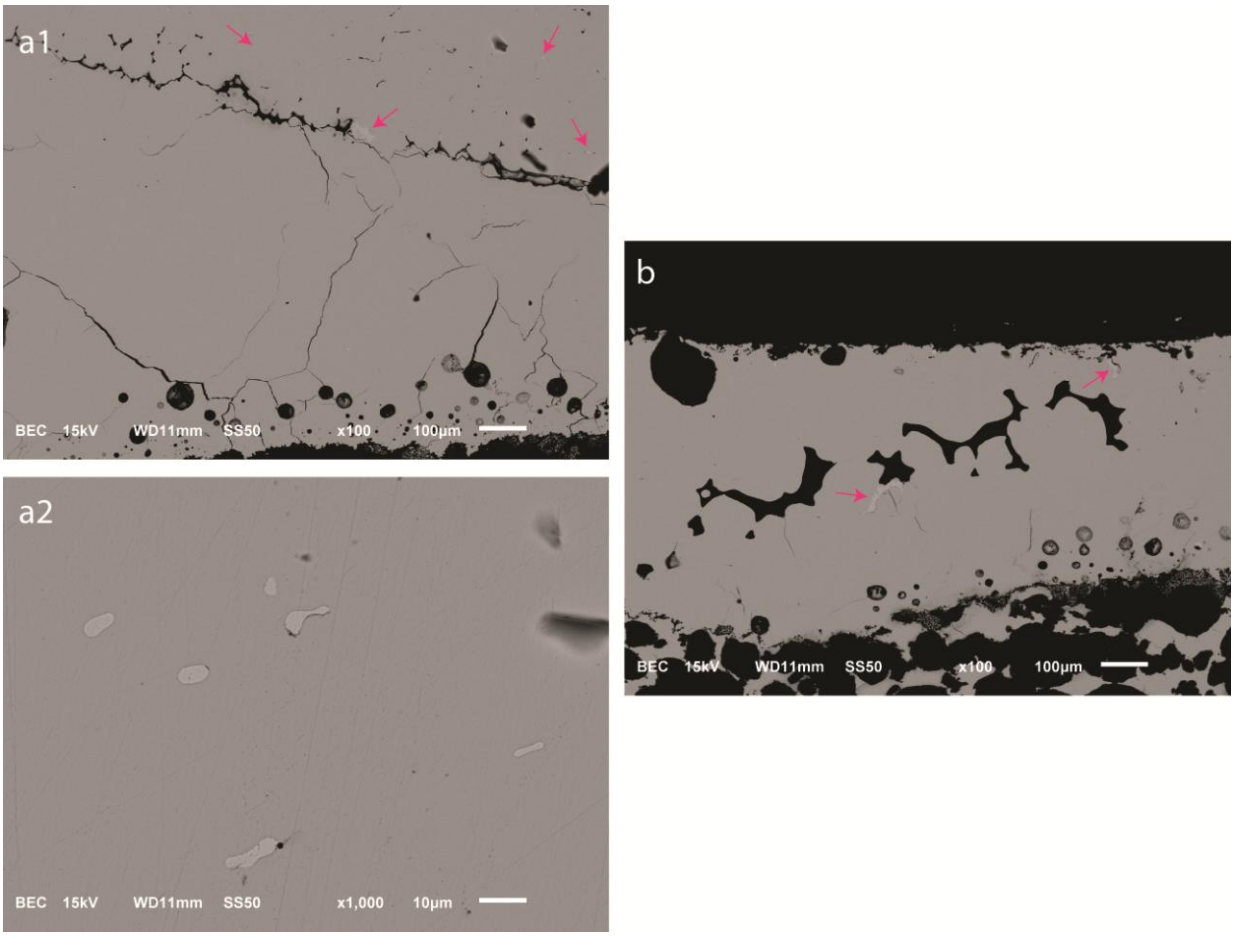

Figure A3. BSE images of (a) Cent1100cc-1 (static run) and (b) Cent1100cc-2 (centrifuge run). (a1) Blebs of Cu metal are mostly found above the crack across the sample (see Figure 35a for entire sample), as shown by the pink arrows. (a2) Cu blebs at a higher magnification. (b) Cu blebs are also found in the centrifuged sample. The synthetic chalcocite may have been prepared too Cu-rich for stoichiometric chalcocite that Cu liquid was exsolved.

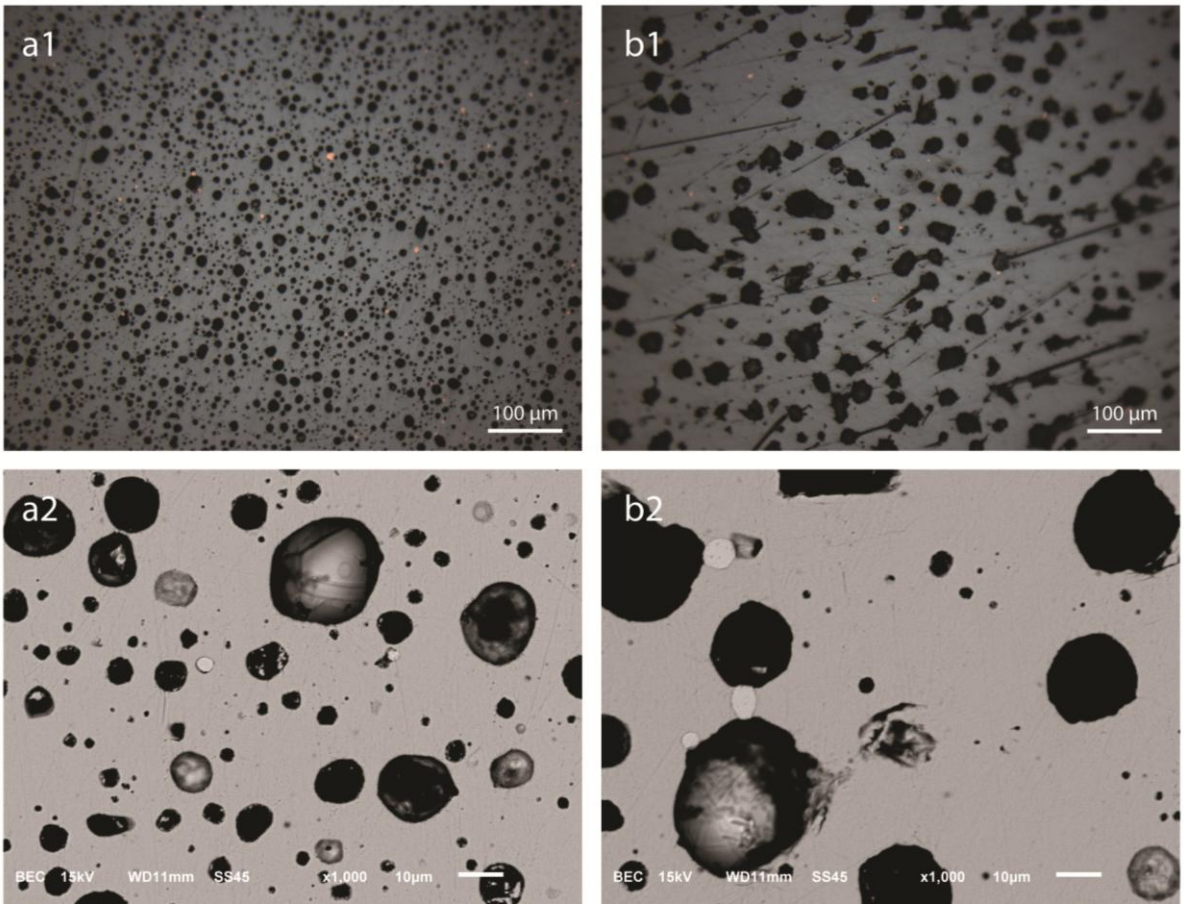

Figure A4. Reflected light photomicrographs (top) and BSE images (bottom) of (a) Cent1050cc-1 (static run) and (b) Cent1050cc-2 (centrifuged run). Blebs of Cu metal are observed throughout the sample (same as those observed in the Cent1100cc experiments in Figure A3). Also noted is the obvious difference in bubble size between the two compositionally identical samples (see Figure 36 as well).

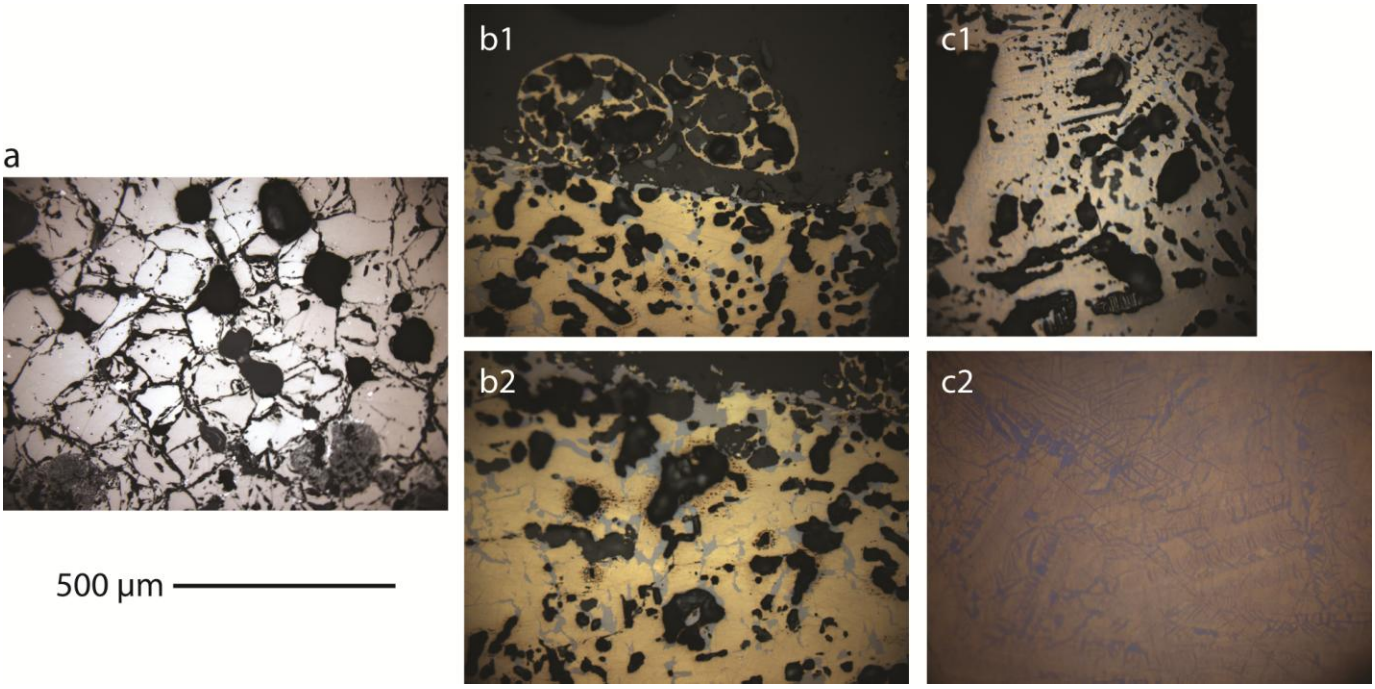

Figure A5. Reflected light photomicrographs of (a) Cent1100-FeS and (b) Cent1100-Mix2, both run in the centrifuge. (c) BN1100-2 (static run) is shown for comparison with Cent1100-Mix2. (a) The existence of a solid phase at run conditions is evidenced by the prominent grain boundaries in the sample. (b) and (c) The same yellow and purple phases are present in the compositionally identical samples. No separation of the quenched purple phase was observed in the centrifuged run in b.

Appendix 2. EDS analyses of buffered metal-free experiments with bornite

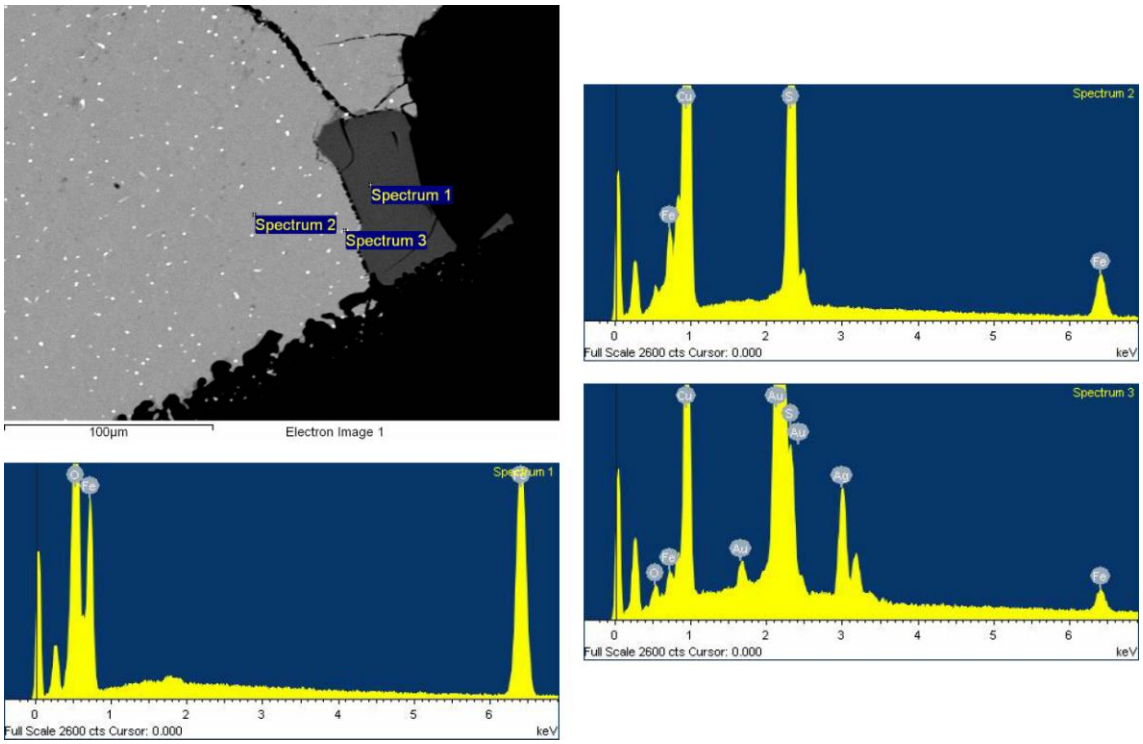

Figure A6. Representative EDS analyses from sample 1200-DopedBN-MMO: magnetite grain (Spectrum 1), bornite melt (Spectrum 2), and the bright metal-bearing phase (Spectrum 3).

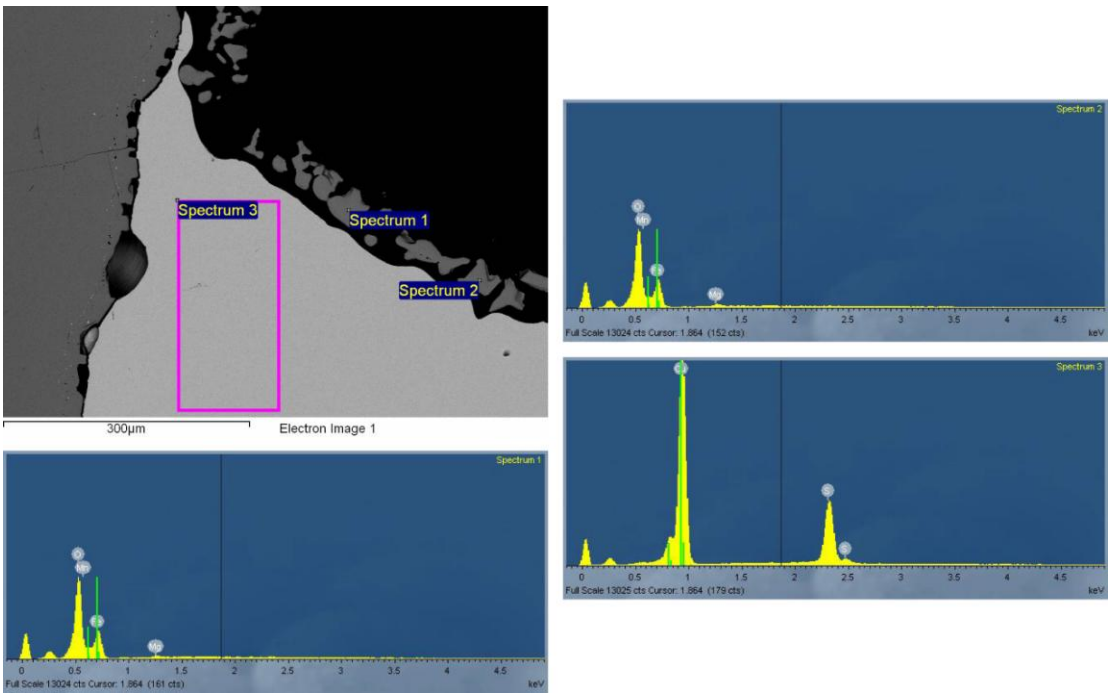

Figure A7. EDS analyses from sample 1100-Bornite-MMO: Mn-O-Fe-Mg blebs (Spectrum 1 and 2), and chalcocite melt (Spectrum 3).

Appendix 3. EDS analyses of buffered Au fusion experiments

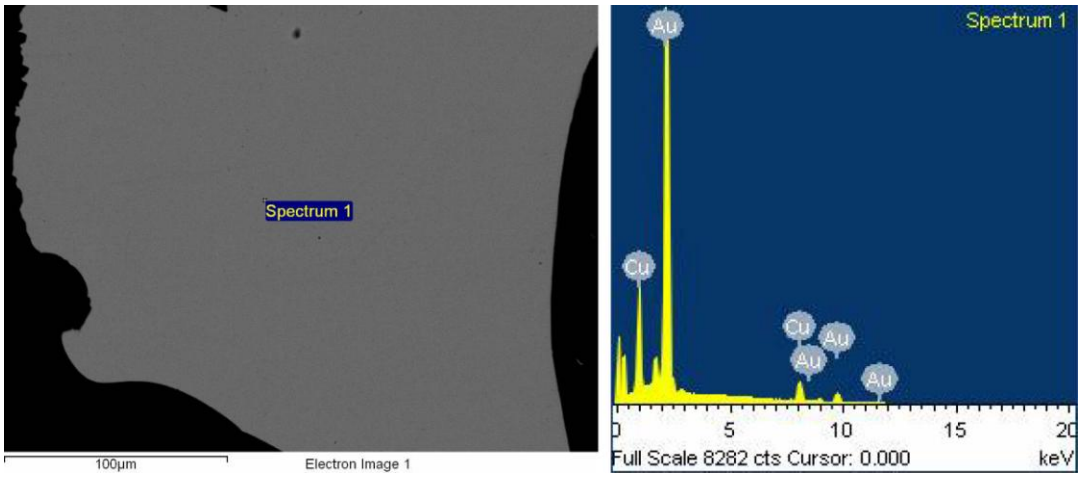

Figure A8. Representative EDS analysis of the Au-Cu alloy in 1050-cc-bn-Au (Figure 45).

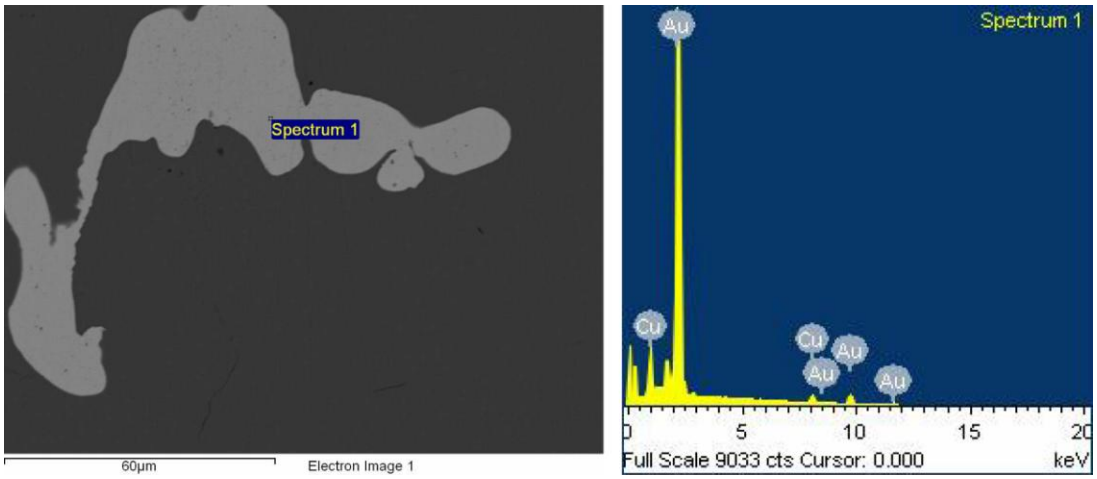

Figure A9. Representative EDS analysis of the Au-Cu alloy in 1050-cc-Au (Figure 46).